UNIVERSITÀ DI PISA

FACOLTÀ DI INGEGNERIA

RELAZIONE PER IL CONSEGUIMENTO DELLA LAUREA SPECIALISTICA IN INGEGNERIA MECCANICA

"Optimization of Helium vessel design for ILC cavities"

RELATORI

Prof. Ing. *Marco Beghini*
Dipartimento di *Ingegneria Meccanica, Nucleare e della Produzione*

Dott. Ing. *Andrea Basti*
INFN Sezione di Pisa

Ing. *Donald V. Mitchell*
Fermi National Accelerator Laboratory

IL CANDIDATO

Enrico Fratangelo

Anno Accademico 2008-2009

Index

Abstract

The ILC (International Linear Collider) is a proposed new major particle accelerator. It consists of two 20 km long linear accelerators colliding electrons and positrons at an energy exceeding 500 GeV. Achieving this collision energy while keeping reasonable accelerator dimensions requires the use of high electric field superconducting cavities as the main acceleration element. These cavities are operated at 1.3 GHz inside an appropriate container (He vessel) at temperatures as low as 1.4 K using superfluid Helium as the refrigerating medium.

The purpose of this thesis, in the context of the ILC R&D activities currently in progress at Fermilab (Fermi National Accelerator Laboratory), is the mechanical study of an ILC superconducting cavity and Helium vessel prototype. The main goals of these studies are the determination of the limiting working conditions of the whole He vessel assembly, the simulation of the manufacturing process of the cavity end-caps and the assessment of the Helium vessel's efficiency. In addition this thesis studies the requirements to certify the compliance with the ASME Code of the whole cavity/vessel assembly.

Several Finite Elements Analyses were performed by the candidate himself in order to perform the studies listed above and described in detail in Chapters 4 through 8. In particular the candidate has developed an improved procedure to obtain more accurate results with lower computational times. These procedures will be accurately described in the following chapters.

After an introduction that briefly describes the Fermilab and in particular the Technical Division (where all the activities concerning with this thesis were developed), the first part of this thesis (Chapters 2 and 3) explains some of the main aspects of modern particle accelerators. Moreover it describes the most important particle accelerators working at the moment and the basic features of the ILC project.

Chapter 4 describes all the activities that were done to certify the compliance of the Helium vessel and the cavity to the ASME code standard. After briefly recalling to the main contents of the the ASME Code (Sections II and VIII - Division II), the procedure used for finding all relevant stresses and comparing the obtained results with the maximum values allowed are explained. This part also includes the buckling verification of the cavity.

In Chapter 5 the manufacturing process of the cavity end-caps, whose function is to link the Helium vessel with the cavity, is studied. The present configuration of the dies is described and the manufacturing process is simulated in order to explain the origin of some defects found on real parts. Finally a new design of the dies is proposed and the resulting deformed piece is compared with the design requirements.

Chapter 6 describes a finite elements analysis to assess the efficiency and the stiffness of the Helium vessel. Furthermore the results of the optimization of the Helium vessel (in order to increase the value of the efficiency) are reported.

The same stiffness analysis is used in Chapter 7 for the Blade-Tuner study. After a description of this tuner and of its function, the preliminary analyses done to confirm the results provided by the vendor are described and then its limiting load conditions are found.

Chapter 8 shows a study of the resistance of all the welds present in between the cavity and the end-cap and between the end-caps and the He vessel for a smaller superconducting cavity operating at 3.9 GHz.

Finally Chapter 9 briefly describes some R&D activities in progress at INFN (Section of Pisa) and Fermilab that could produce significant cost reductions of the Helium vessel design.

All the finite elements analyses contained and described in this thesis made possible the certification of the whole superconducting cavity-Helium vessel assembly at Fermilab. Furthermore they gave several useful indications to the Fermilab staff to improve the performance of the Helium vessel by modifying some design parameters or refining the manufacturing processes.

1. The Fermi National Accelerator Laboratory (Fermilab)

1.1 – Introduction

Fermilab, originally named the National Accelerator Laboratory, was commissioned by the U.S. Atomic Energy Commission, under a bill signed by President Lyndon B. Johnson on November 21, 1967. Founding Director Robert R. Wilson committed the laboratory to firm principles of scientific excellence, esthetic beauty, stewardship of the land, fiscal responsibility and equality of opportunity. Universities Research Association built the laboratory, and has operated the facility under those principles since its founding.

Fig. 1.1 Fermilab Site

On May 11, 1974, the laboratory was renamed in honor of 1938 Nobel Prize winner Enrico Fermi, one of the preeminent physicists of the atomic age. Fermi's widow, Laura Fermi, spoke at the dedication ceremonies.
Two major components of the Standard Model of Fundamental Particles and Forces were discovered at Fermilab: the bottom quark (May-June 1977) and the top quark (February 1995). In July 2000, Fermilab experimenters announced the first direct observation of the tau neutrino, the last fundamental particle to be observed. Filling the final slot in the Standard Model, the tau neutrino set the stage for new discoveries and new physics with the inauguration of Collider Run II of the Tevatron in March 2001.
The Tevatron, four miles in circumference and originally named the Energy Doubler when it began operation in 1983, is the world's highest-energy particle accelerator. Its 1,000 superconducting magnets are cooled by liquid helium to -268 degrees C (-450 degrees F). Its low-temperature

cooling system was the largest ever built when it was placed in operation in 1983. The American Society of Mechanical Engineers has designated the Tevatron cryogenic system an International Historic Mechanical Engineering Landmark.
Fermilab has added the two-mile Main Injector accelerator to increase the number of proton-antiproton collisions in the Tevatron, greatly enhancing the chances for important discoveries in Run II. The two apartment building-sized collider detectors, CDF and DZero, have undergone extensive upgrades during the nearly decade-long preparations for Run II.
Some of the most important Fermilab's departments and experiment sites are listed below:

- Technical Division
- CDF
- D0

These departments are located (as shown in the picture below) near the Tevatron and will be briefly described in the next paragraphs

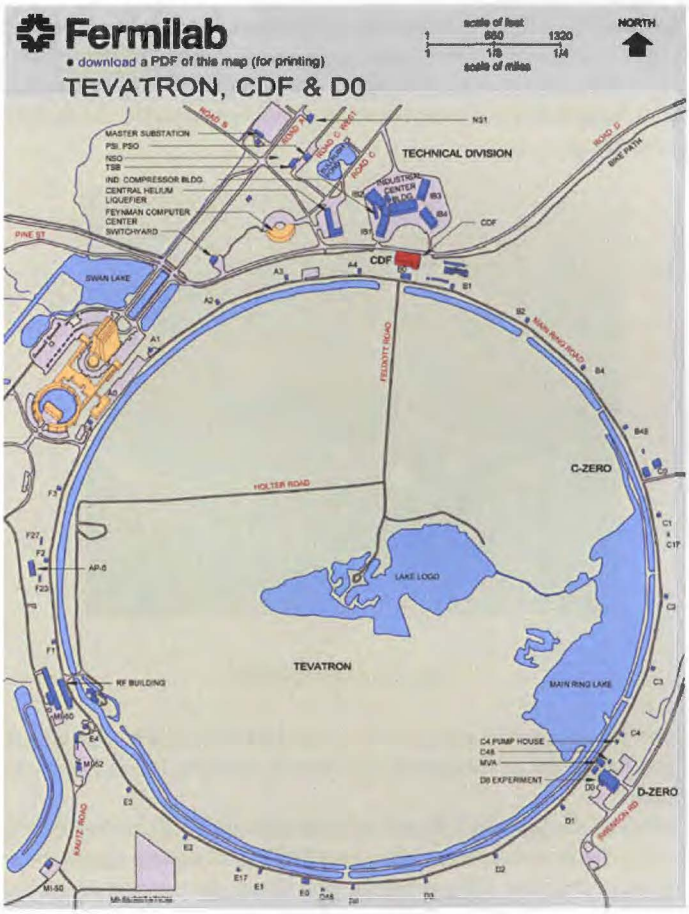

Fig. 1.2 Fermilab map including the Tevatron ring and some important departments (Technical Division, Wilson Hall, CDF and D0)

1.2 – The Technical Division

Fig. 1.3 Technical Division site

The Fermilab's Technical Division is the department concerning with all the engineering and R&D studies on the particle accelerators: these activities are bound not only with the Fermilab experiments but even with the CERN one. In fact Fermilab provided for the construction of the new circular accelerator LHC some of the magnets and totally spent several millions of dollars in order to improve the know-how about the superconducting magnets.
Some of the technical division's most important activities at the moment are listed as follow:

- R&D for the new particle accelerator, ILC: As a part of an international collaboration that consists of about 2000 people from more than 100 universities and laboratories in over two dozen countries, Fermilab has made it their highest priority to make the ILC a reality. Research facilities around the world are collaborating to solve the technical challenges of building such a massive and complex machine. Fermilab scientists are developing designs for klystrons, damping rings, detectors and other specialized ILC components. Fermilab is also heavily involved in the research and development of the cryomodules and superconducting cavities -- the heart of the technology for the ILC. The whole work that has been summarized in this thesis has been developed inside the Technical Division, cooperating with the Fermilab's staff in order to increase the R&D results about the ILC mechanical structure.

Fig. 1.4 Main activities performed in the Technical Division's workshop: the figures shown relates about some assembled cryomodules (on the left) and about a cavity that is being tested (on the right)

- R&D for the superconducting magnets: Fermilab has a strong superconducting (SC) accelerator magnet R&D program, which is natural for a laboratory with the largest SC

accelerator in the world, the Tevatron. The history of SC accelerator magnet development at Fermilab includes 4T NbTi magnets for the Tevatron in the 70's-80's, 7T NbTi dipole models for the SSC in the second part of the 80's, and 9T NbTi High Gradient quadrupoles for the LHC IR's in the second part of the 90's. In 1998 the Technical Division started the High Field Magnet (HFM) program at Fermilab. The program goal was the development of new generation SC accelerator magnets with operation fields above 10 T at 4.5 K and high operation margins for different applications. The possible applications include SC magnets for the Tevatron, particularly to replace some present dipoles and provide space for special devices, to replace existing low-b quadrupoles or to create a new interaction region (IR); SC magnets for a future Very Large Hadron Collider (VLHC); 2nd generation LHC IR dipoles and quadrupoles for luminosity upgrade; SC magnets for beam transfer lines, etc. The magnet requirements for upgrading existing and future machines push accelerator magnet technology to limits exceeding the present level based on the NbTi superconductor. The Fermilab's present SC Magnet R&D program is focused on Nb3Sn accelerator magnets and explores two basic technologies used for brittle superconductors - wind-and-react and react-and-wind. The other superconductors and technologies will be also studied as soon as they become available for application in accelerator magnets.

1.3 – The CDF experiment

Fig. 1.5 CDF detector

The CDF experiment (Collider Detector experiment at Fermilab, shown on figure 1.5) is an international collaboration of about 500 Physicists (from about 30 American universities and National laboratories, etc, plus also from about 30 groups from universities and national laboratories from Italy, Japan, UK, Canada, Germany, Spain, Russia, Finland, France, Taiwan, Korea, Switzerland, etc.). The CDF detector itself weighs 5000 tons and is about 12 meters in all three dimensions. The collision's approximate energy of about 1000 Gev and the goal of this experiment is to measure exceptional events out of the billions of collisions to

- Look for the production of New Physics
- Measure and study the production and decay of heavy particles such as the Top and Bottom Quarks, and the W and Z bosons.
- Measure and study the production of High Energy jets and photons
- Other studies such as diffraction, etc.

1.4 – The D0 experiment

The DØ experiment is located at the second interaction region, where proton and antiproton beams intersect, on the Tevatron synchrotron ring, labelled 'DØ'.

The experiment is a test of the Standard Model of particle physics. It is sensitive in a general way to the effects of high energy collisions and so is meant to be a highly model independent probe of the theory. This is accomplished by constructing and upgrading a large volume elementary particle detector.

The detector is designed to stop as many as possible of the subatomic particles created from energy released by colliding proton/antiproton beams. The intersection region where the matter-antimatter annihilation takes place is close to the geometric center of the detector. The beam collision area is surrounded by tracking chambers in a strong magnetic field parallel to the direction of the beam(s). Outside the tracking chamber are the pre-shower detectors and the calorimeter. The Muon Chambers form the last layer in the detector. The whole detector is encased in concrete blocks which act as radiation shields.

2. THE PARTICLE ACCELERATORS AND THE ILC PROJECT

2.1 – Particle accelerator description

A particle accelerator (or atom smasher) is a device that uses electric fields to propel electrically charged particles to high speeds and to contain them. An ordinary CRT television set is a simple form of accelerator.

Beams of high-energy particles are useful for both fundamental and applied research in the sciences. For the most basic inquiries into the dynamics and structure of matter, space, and time, physicists seek the simplest kinds of interactions at the highest possible energies. These typically entail particle energies of many GeV, and the interactions of the simplest kinds of particles: leptons (e.g. electrons and positrons) and quarks (the elementary particle found in protons and neutrons) for the matter, or photons and gluons (the particles responsible for the binding of protons and neutrons into the atom's core) for the field quanta.

Since isolated quarks are experimentally unavailable because of the impossibility of singularly isolate them apart from the others, the simplest available experiments involve the interactions of, first, leptons with each other, and second, of leptons with nucleons, which are composed of quarks and gluons. Thus elementary particle physicists tend to use machines creating beams of electrons, positrons, protons, and anti-protons, interacting with each other or with the simplest nuclei (eg, hydrogen or deuterium) at the highest possible energies, generally hundreds of GeV or more.

Everyday examples of particle accelerators are cathode ray tubes found in television sets and X-ray generators. These low-energy accelerators generators use a single pair of electrodes with a DC voltage of a few thousand volts between them. In an X-ray generator, the target itself is one of the electrodes. A low-energy particle accelerator called an ion implanter is used in the manufacture of integrated circuits.

The largest and most powerful particle accelerators in the world, like the Large Hadron Collider (LHC) (scheduled to start operation in February 2009) and the Tevatron, are used for experimental particle physics.

Particle accelerators can also produce proton beams, which can produce "proton-heavy" medical or research isotopes as opposed to the "neutron-heavy" ones made in fission reactors. An example of this type of machine is LANSCE at Los Alamos.

There are two basic shapes of accelerators, the linear and the circular one.

In a linear accelerator (linac), particles are accelerated in a straight line with a target of interest at one end. Linacs are very widely used - every cathode ray tube contains one. They are also used to provide an initial low-energy kick to particles before they are injected into circular accelerators. The longest linac in the world is the Stanford Linear Accelerator, SLAC, which is 3 km (2 miles) long.

SLAC is an electron-positron collider. Linear accelerators are also widely used in medicine, for radiotherapy and radio-surgery.

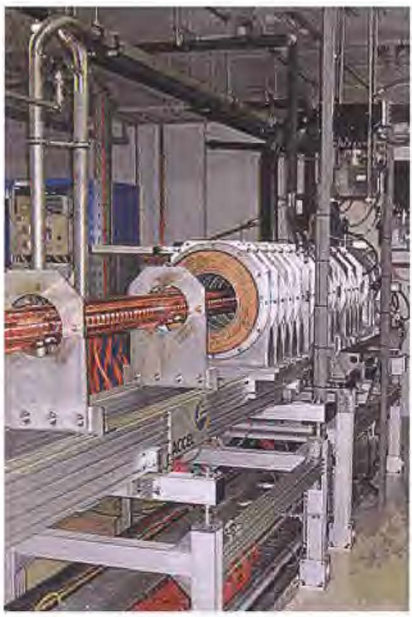

Fig. 2.1 – Linac used for the Australian Synchrotron, used to accelerate the electron beam to energies of 100 MeV

In the circular accelerator, particles move in a circle until they reach sufficient energy. The particle track is typically bent into a circle using electromagnets. The earliest circular accelerators were cyclotrons, invented in 1929 by Ernest O. Lawrence at the University of California, Berkeley. Cyclotrons have a single pair of hollow 'D'-shaped plates to accelerate the particles and a single large dipole magnet to bend their path into a circular orbit. It is a characteristic property of charged particles in a uniform and constant magnetic field B that they orbit with a constant period, at a frequency called the cyclotron frequency, so long as their speed is small compared to the speed of light c. This means that the accelerating D's of a cyclotron can be driven at a constant frequency by a radio frequency (RF) accelerating power source, as the beam spirals outwards continuously. The particles are injected in the centre of the magnet and are extracted at the outer edge at their maximum energy. Cyclotrons reach an energy limit because of relativistic effects whereby the particles effectively become more massive, so that their cyclotron frequency drops out of synch with the accelerating RF. Therefore simple cyclotrons can accelerate protons only to an energy of around 15 million electron volts (15 MeV, corresponding to a speed of roughly 10% of c).

To reach higher energies, with relativistic mass approaching or exceeding the rest mass of the particles (for protons, billions of electron volts GeV), it is necessary to use a synchrotron. This is an accelerator in which the particles are accelerated in a ring of constant radius. An immediate advantage over cyclotrons is that the magnetic field need only be present over the actual region of the particle orbits, which is very much narrower than the diameter of the ring. However, since the particle momentum increases during acceleration, it is necessary to turn up the magnetic field B in proportion to maintain constant curvature of the orbit. In consequence synchrotrons cannot accelerate particles continuously, as cyclotrons can, but must operate cyclically, supplying particles in bunches, which are delivered to a target or an external beam in beam "spills" typically every few seconds.

Fig. 2.2 – Segment of an electron synchrotron at DESY, Germany

Circular geometry has significant advantages at energies up to and including tens of GeV: with a circular design, particles can be effectively accelerated over longer distances. Also, only a fraction of the particles brought onto a collision course actually collide. In a linear accelerator, the remaining particles are lost; in a ring accelerator, they keep circulating and are available for future collisions. The disadvantage of circular accelerators is that particles moving along bent paths will necessarily emit electromagnetic radiation known as synchrotron radiation. Energy loss through synchrotron radiation is inversely proportional to the mass of the particles in question. That is why it makes sense to build a hadron collider such as the LHC for protons or, alternatively, for lead nuclei, as a ring collider, an electron-positron collider of the same size would never be able to achieve the same collision energies, as the synchrotron radiation losses would be too great.
Even if the effective collision energy at the LHC will be higher than the ILC foreseen collision energy (14,000 GeV for the LHC vs. ~500 GeV for the ILC), measurements could be made more accurately at the ILC. Since collision between electrons and positrons are much simpler to analyse than collisions between many quarks, antiquarks and gluons, one of the roles of the ILC would be making precision measurements of the properties of particles discovered at the LHC.

2.2 – Existing particle accelerators

Linear accelerators ("linacs") accelerate elementary particles along a straight path. Circular accelerators, such as the Tevatron, the LEP, and the Large Hadron Collider (LHC), use circular paths.

Some of the most important existing particle accelerators used for the research of the matter will be listed and briefly described below:

- **LHC**: The Large Hadron Collider (LHC) is the world's largest and highest-energy particle accelerator, intended to collide opposing particle beams, protons at an energy of 7 TeV/particle or lead ions at 574 TeV/ion. The Large Hadron Collider was built by the European Organization for Nuclear Research (CERN) with the intention of testing various predictions of high-energy physics, including the existence of the hypothesised Higgs boson and of the large family of new particles predicted by supersymmetry. It lies in a tunnel 27 kilometres in circumference, as much as 175 metres beneath the Franco-Swiss border near Geneva, Switzerland. It is funded by and built in collaboration with over 10,000 scientists and engineers from over 100 countries as well as hundreds of universities and laboratories. The collider tunnel contains two adjacent parallel beam pipes that intersect at four points, each containing a proton beam, which travel in opposite directions around the ring. Some

1,232 dipole magnets keep the beams on their circular path, while an additional 392 quadrupole magnets are used to keep the beams focused, in order to maximize the chances of interaction between the particles in the four intersection points, where the two beams will cross. In total, over 1,600 superconducting magnets are installed, with most weighing over 27 tonnes. Approximately 96 tonnes of liquid helium is needed to keep the magnets at their operating temperature of 1.9 K, making the LHC the largest cryogenic facility in the world at liquid helium temperature.

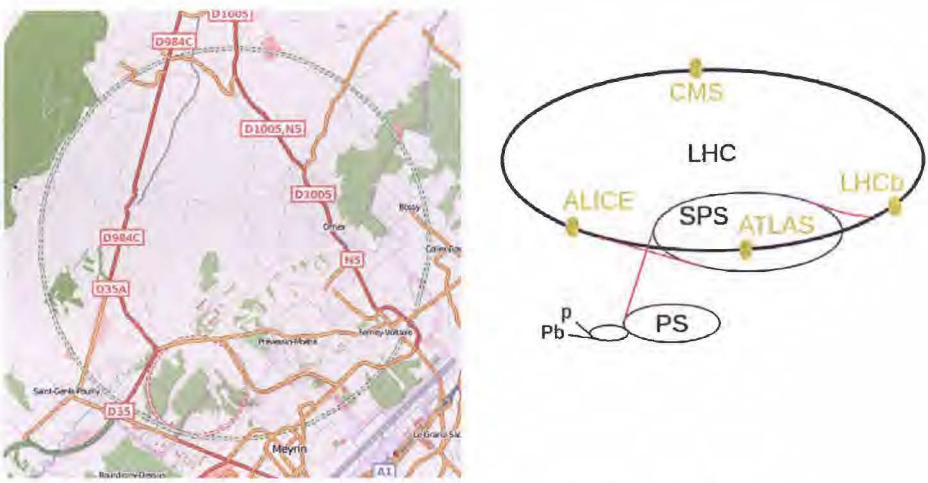

Fig. 2.3 – Map of the Large Hadron Collider at CERN (on the left) and map of the LHC experiments (on the right)

- **Tevatron**: Fermilab was started in 1967. The first large circular accelerator operating on site was the Main Ring with its injection stages consisting of a proton source, a linear accelerator (LINAC) and a Booster ring. The Main Ring, shown at the center of Fig. 1.2, had a circumference of 6.2 Km. The proton beam had a maximum energy of 450 GeV. It was ejected and used against fixed targets. A few years later, the Tevatron, the first accelerator made with superconducting magnets, was built in the same tunnel. The Main Ring served as last injection element to the Tevatron. The proton beam energy doubled to 900 GeV. In 1984, the Antiproton Source became integral part of Fermilab accelerator complex, allowing the Tevatron to operate as a proton-antiproton collider with a center of mass energy of 1800 GeV. More recently, the Main Injector, to replace the Main Ring and increase the intensity of the primary proton beam, and the Antiproton Recycler, to increase the intensity of the antiproton source, were built. Several stages progressively raise the beam energy. The accelerating steps of the proton beam at Fermilab include the Cockcroft-Walton electrostatic accelerator, the LINAC and the Booster and the Main Injector

Fig. 2.4 – Picture from inside the Tevatron Accelerator at Fermilab

For the collider mode of the Tevatron, the Main Injector, beyond being used as injector for the Tevatron itself, also feed an antiproton source. The source comprises an external target where anti-protons are generated, a debuncher ring, where antiproton shots are first collected, debunched and partially cooled, an accumulator ring fed by the debuncher. The Recycler ring is used as an additional anti-proton accumulator to store beams of higher intensity. It is made of permanent magnets, and it is located in the same tunnel as the Main Injector. The Cockcroft-Walton provides the first stage of acceleration. In this device, electrons are added to hydrogen atoms. The resulting negative ions, each consisting of two electrons and one proton, are attracted by a positive voltage and accelerated to energy of 750 KeV. After leaving the Cockcroft-Walton the negative hydrogen ions enter a linear accelerator called the LINAC. The LINAC consists of five tank containing sets of drift tubes. An oscillating electric field is applied to the tubes. The particles travel through the drift tubes in phase with the electric field, shielded by the tubes when the electric field would slow them down, and emerging in the gaps In between the tubes when the field is accelerating. In a recent upgrade the LINAC energy was increased to 400 MeV. After exiting the LINAC, the ions are stripped of their electrons by a carbon foil, resulting in a proton beam that is injected into the Booster synchrotron ring. The Booster accelerates the protons to an energy of 8 GeV, and, via pulsed operation, it organizes the high frequency sequence of LINAC pulsed into a smaller number of bunches for injection into the Main Injector. The Main Injector accelerates alternatively protons and antiprotons, up to 150 GeV for injection in the Tevatron. Alternatively it sends a 120 GeV beam to the antiproton production target. The final stage of acceleration is provided by the Tevatron, a superconducting synchrotron of 2 Km in diameter, with bending dipole magnets reaching a 4.5T magnetic field. In collider mode, protons and antiprotons are injected separately into the Tevatron and circulate in the same beam pipe. The acceleration in the Tevatron is provided by a set of RF

superconducting cavities. The luminosity in the Tevatron collider is proportional to the beam currents, the antiproton current being critical element. Collisions of the beam bunches must occur at the center of the particle detectors surrounding the beam pipe at specific location around the Tevatron ring. The two main detectors operating at Tevatron Collider are CDF (Collider Detector at Fermilab) and D0. These detectors discovered the Top Quark in 1995.

- **X-FEL**: The European x-ray free electron laser (XFEL) is a planned European project in strong connection with the DESY research center in Hamburg. A free electron laser generates high intensity electromagnetic radiation (in this case x-rays) by accelerating electrons to relativistic speeds. The XFEL is constructed such that the electrons produce x-ray light in synchronisation resulting in high-intensity x-ray pulses with the properties of laser light with intensities much brighter than that produced by conventional synchrotron light sources. The XFEL is planned to run 3.4 km underground from the DESY site, in the quarter Bahrenfeld of Hamburg, to the town of Schenefeld where a new XFEL research facility is to be constructed. Electrons will be accelerated to an energy of 10-20 GeV by a 2.1 km long superconducting linear accelerator. The electrons are then introduced into the magnetic fields of undulators where they undergo curved trajectories resulting in the emission of x-ray radiation. X-FEL is very important because it is a linear accelerator, such as the proposed ILC, and uses the same accelerating technologies that are supposed to be introduced for it. So it could be considered a very effective prototype of ILC.

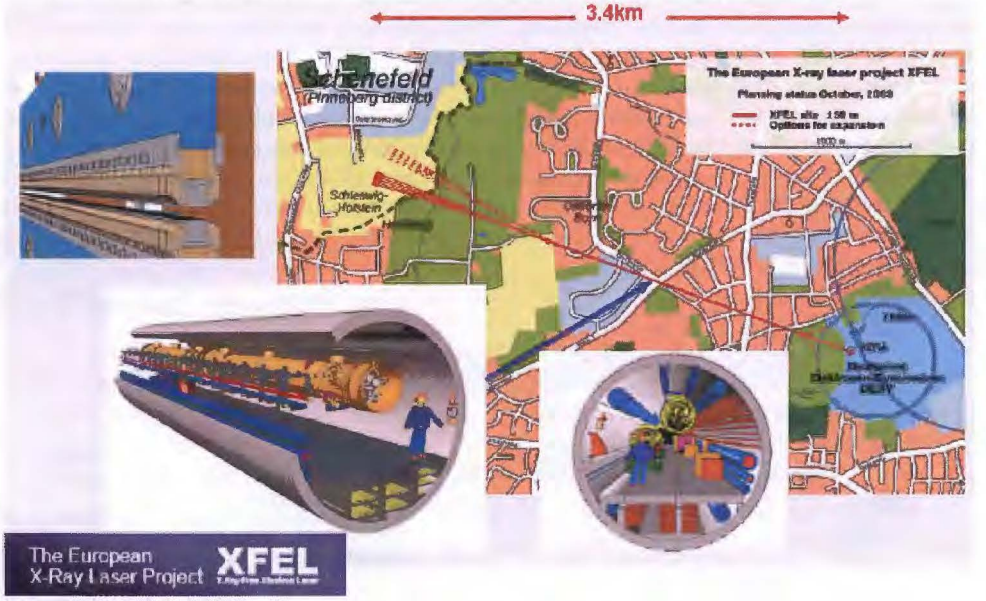

Fig. 2.5 – Map of the XFEL accelerator at DESY, Germany

- **SLAC**: The SLAC National Accelerator Laboratory, originally named Stanford Linear Accelerator Center, is a United States Department of Energy National Laboratory operated by Stanford University under the programmatic direction of the U.S. Department of Energy Office of Science. The SLAC research program centers on experimental and theoretical research in elementary particle physics using electron beams and a broad program of research in atomic and solid-state physics, chemistry, biology, and medicine using synchrotron radiation. The 2.0 mile (3.2 kilometer) long underground accelerator is the longest linear accelerator in the world, and is claimed to be "the world's straightest object". Founded in 1962 as the Stanford Linear Accelerator Center, the facility is located on 426

acres (1.72 square kilometers) of Stanford University-owned land on Sand Hill Road in Menlo Park, California—just west from the University's main campus. The main accelerator, a 2.0 mile-long RF linear accelerator, which can accelerate electrons and positrons up to 50 GeV, has been operational since 1966. It is buried 30 feet (10 meters) below ground and passes underneath Interstate 280.

Fig. 2.6 – Map of the SLAC accelerator at Stanford, USA

2.3 – Linear accelerator's description

A particle accelerator is an electrical device for the acceleration of subatomic particles: two particle beams, made with particles with the same mass but with opposite electrical and magnetic properties (so that there are particles and anti-particles), hurt one against the other and this high energy impact allows the atoms' nuclei to split and some new particles (not easily achievable through different ways) to be formed. This sort of device has many applications: in example it allows the study of the smallest sizes of the matter, or the generation of X-rays in a hospital environment, or even to inject the energized particles into a higher energy particle accelerator at a dedicated experimental particle physics laboratory. The design of a particle accelerator depends on the type of particle that is being accelerated: electron, proton or ion.

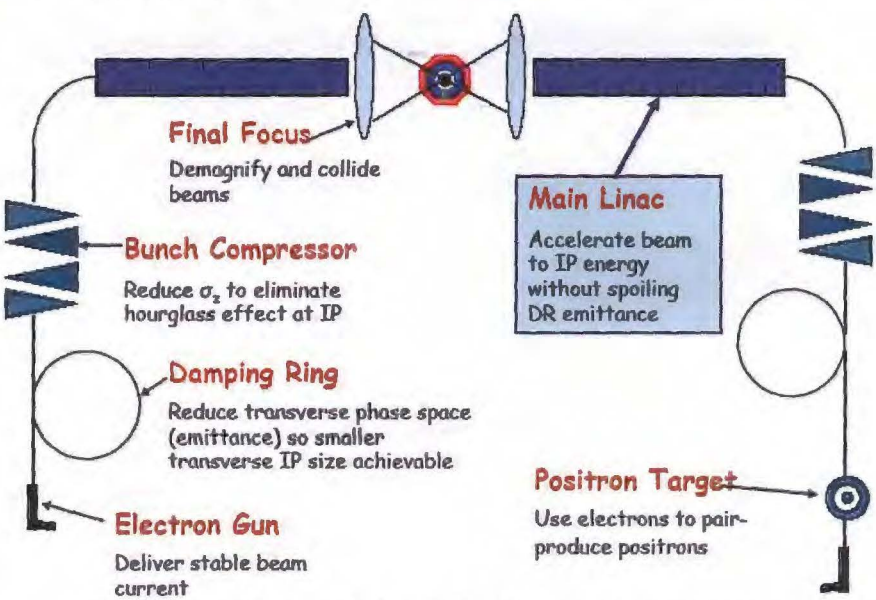

Fig. 2.7 – Conceptual scheme for a linear particle accelerator

A linear particle accelerator consists of the following elements:

- The particle source. The design of the source depends on the particle that is being moved. Electrons are generated by a cold cathode, a hot cathode, a photocathode, or RF ion sources. Protons are generated in an ion source, which can have many different designs. If heavier particles are to be accelerated, (e.g. uranium ions), a specialized ion source is needed.
- A high voltage source for the initial injection of particles.
- A hollow pipe vacuum chamber. The length will vary with the application. If the device is used for the production of X-rays for inspection or therapy the pipe may be only 0.5 to 1.5 meters long. If the device is to be an injector for a synchrotron it may be about ten meters long. If the device is used as the primary accelerator for nuclear particle investigations, it may be several thousand meters long.
- Within the chamber, electrically isolated cylindrical electrodes whose length varies with the distance along the pipe. The length of each electrode is determined by the frequency and power of the driving power source and the nature of the particle to be accelerated, with shorter segments near the source and longer segments near the target. The mass of the particle has a large effect on the length of the cylindrical electrodes; for example an electron is considerably lighter than a proton and so will generally require a much larger section of cylindrical electrodes as it accelerates very quickly - think about a concrete ball and a tennis ball; it is easier to accelerate the tennis ball from rest (this comes about because of the kinetic energy being equal to the energy gained by the electron as it is accelerated through the potential difference, usually in the region of 5KV.)
- One or more sources of radio frequency energy, used to energize the cylindrical electrodes. A very high power accelerator will use one source for each electrode. The sources must operate at precise power, frequency and phase appropriate to the particle type to be accelerated to obtain maximum device power.

2.4 – The ILC project

The International Linear Collider (ILC) is a proposed linear particle accelerator. It is planned to have a collision energy of 500 GeV initially, and, if approved after the project has published its Technical Design Report, planned for 2012, could be completed in the late 2010s.A later upgrade to 1000 GeV is possible. The host country for the accelerator has not yet been chosen.

Three sites satisfy a matrix of criteria agreed upon by the regional CFS groups early in the RDR process. Although the sites have been developed for the baseline 500 GeV center-of-mass machine, it was a requirement that all sites can support the extension to the 1 TeV center-of-mass machine (an estimated additional 20 km of site), and that sufficient local infrastructure (power) is available for this upgrade.

The three sample sites have the following characteristics:

- The Americas sample site lies in Northern Illinois near the existing Fermi National Accelerator Laboratory. The site provides a range of locations to position the ILC in a north-south orientation. The site chosen has approximately one-quarter of the machine on the Fermilab site. The surface is primarily flat, with surface elevations ranging from 200 meters to 275 meters above sea level. The long tunnels are bored in a contiguous dolomite rock strata ('Galena Platteville'), at a typical depth of 30-100 m below the surface.
- The Asian site has been chosen from several possible ILC candidate sites in Japan. The sample site has a uniform terrain located along a mountain range, with a tunnel depth

ranging from 40 m to 600 m. The chosen geology is uniform granite highly suited to modern tunneling methods. One specific difference for the Asian site is the use of long sloping access tunnels instead of vertical shafts, the exception being the experimental hall at the Interaction Region, which is accessed via two 112 m deep vertical shafts. The sloping access tunnels take advantage of the mountainous location of the sample site.

- The European site is located at CERN, Geneva, Switzerland, and runs parallel to the Jura mountain range, close to the CERN site. The majority of the machine is located in the 'Molasse' (a local impermeable sedimentary rock), at a typical depth of 370 m.

A competitive design study known as CLIC is also underway; it seems unlikely that both machines will be built.

The ILC would collide electrons with positrons. It will be between 30 km and 50 km (19-31 mi.) long, more than 10 times as long as the 50 GeV Stanford Linear Accelerator, the longest existing linear particle accelerator. The proposal was previously known by various names in different regions.

2.4.1 – Requirements for the High Gradient condition

The requirements for accelerating the particles with a high electrical field are listed as follow:

- cavity design: the cavity is the electro-magnetic energy container, that supply its energy to the beam who's passing through it. In order to maximize the energy furnished to the beam and limit the energy loss it is important to take in account two parameters: the first one (called the Q parameter) concerns with the ratio between the electro-magnetic energy stored into the device and the power that is dissipated on the cavity's wall, while the second one (called the Rs parameter) concerns with the cavity's surface resistance. The Q parameter depends by the Rs one, so it is the index for the "quality" of the cavity: fixing the Rs parameter, the Q one is higher when the super-conducting regimen is held and when a stationary energy wave is achieved. In the picture below the ratio between the dissipated energy for a super-conducting regimen and a normal-conducting one is shown.
  In order to efficiently accelerate the beam, multi-cell resonators have been introduced, by repeating the resonating structure for several times and merging the resonators through couplings.

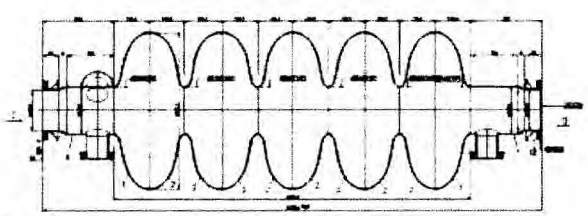

Fig. 2.9 – Sample of a resonating structure. In order to create a multi-cell resonator it is necessary to serially link these single cells

The cavity's profile is designed in order to minimize the power losses with the support of the CAD devices, that can study the full parametric model of the cavity and find the best trade-off solution (a parametrization sample is shown in Fig. 2.10).

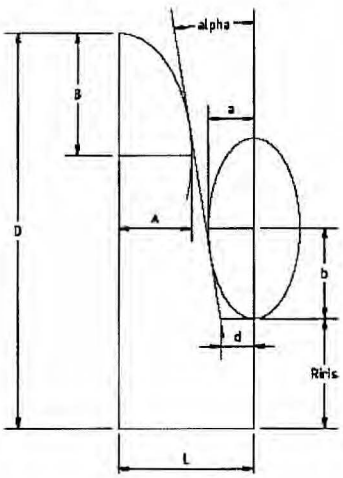

Fig. 2.10 – Parametric model of the cavity's profile

- right choice of the material: the best material usable for the superconducting cavities is the niobium because of its mechanical and magnetic properties and because of its readily availability; in fact the niobium is the elemental superconductor with the highest critical temperature and the highest critical magnetic field (the conditions that make the superconductor work such as a normal conductor), it has a good formability (comparable with the copper). The problem of using the niobium is that it has a good affinity with interstitial impurities such as H, that degrade the efficiency parameters (Rs) of the cavity. The typology of niobium used for the superconducting cavities is the High purity one (called RRR niobium): in order to obtain it multiple electron beam melting steps need to be performed under vacuum condition, so that all the volatile impurities can be eliminated. After the purification process the niobium is cut, forged and rolled (its final form is a sheet) so that it is ready for the Eddy Current Scanner, where the rolling defects and some interstitial defects can be detected. At this point the sheets are ready to be formed with a press up to the required shape: for a multi-cell cavity several pieces are prepared and then welded together as shown in the figure below. The final realization steps are the in-situ baking (where the material is leaded up to a 150°C temperature in order to create a uniform dielectric layer) and the electro-polishing (where a much smoother surface is achieved).

- Cavity mechanical fabrication: in order to achieve the best results, the cavity fabrication is set up in close connection with industrial companies. In fact the operations such as the e-beam welding, the stiffener-ring insertion and the tuning are very important for the cavity's final properties.
- Surface treatments: the most important processes are the electro-polishing and the High pressure water rinsing. In the electro-polishing (described in Fig. 2.11) niobium and aluminum are immersed in an acid solution in order to create a galvanic cell. During this process all the superficial asperities are removed.

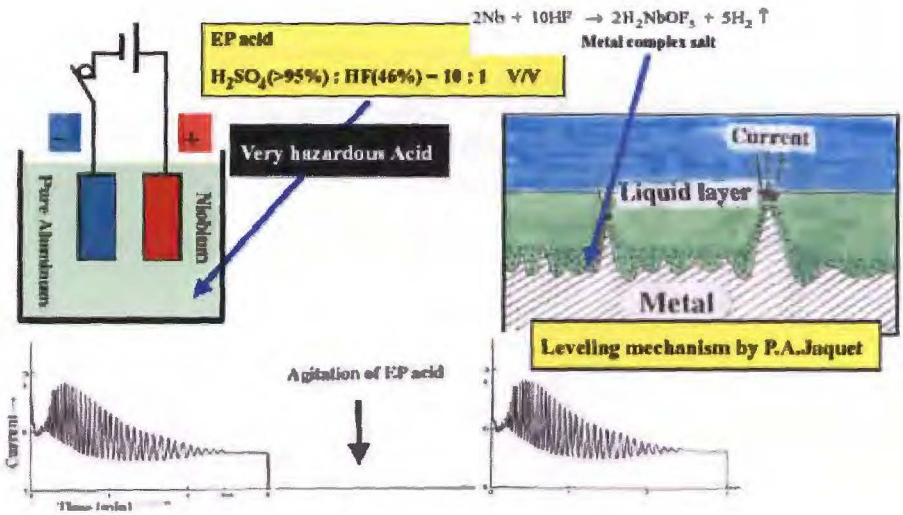

Fig. 2.11 – Scheme of the electro-polishing process

- The high pressure water rinsing is the final superficial treatment for the cavity: the cavity is rinsed by a ultra-pure water pressurized jet. Several sweeps are performed on every cavity.
- Assembly environment: Typically, the cavities of a cavity string are assembled in a class 10 or class 100 clean room on an assembly bench over a period of several days after they have been qualified in the final tests. Every cavity is high pressure rinsed for several hours, dried in a class 10 clean room, auxiliary parts are attached, high pressure rinsed again, dried and mounted onto the assembly bench. The most critical part of the assembly is the interconnection between two cavities, monitored by particle counting.

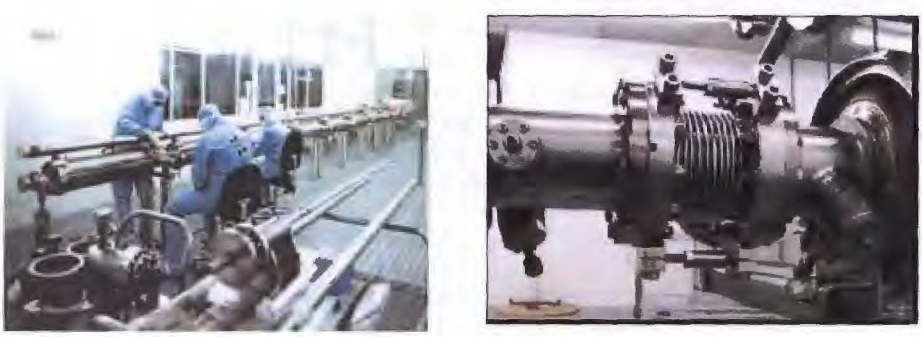

Fig. 2.12 – Technicians during the cavity assembly (on the left) and sample of the interconnection between two cavities

2.4.2 – Realization of the cryogenic conditions

As it was introduced above, in order to minimize the energy dissipated in the cavity a superconducting regimen must be held: this choice leads to the introduction of a coolant at a 2K

temperature and the ideal Carnot cycle efficiency and the cryo losses must be taken in account. Furthermore a whole plant for the distribution and recovery of the coolant must be built around the accelerator.
In order to protect the cryogenic environment for the superconducting cavities and support them the cryomodule (see Fig. 2.13) has been introduced for all the modern particle accelerators.

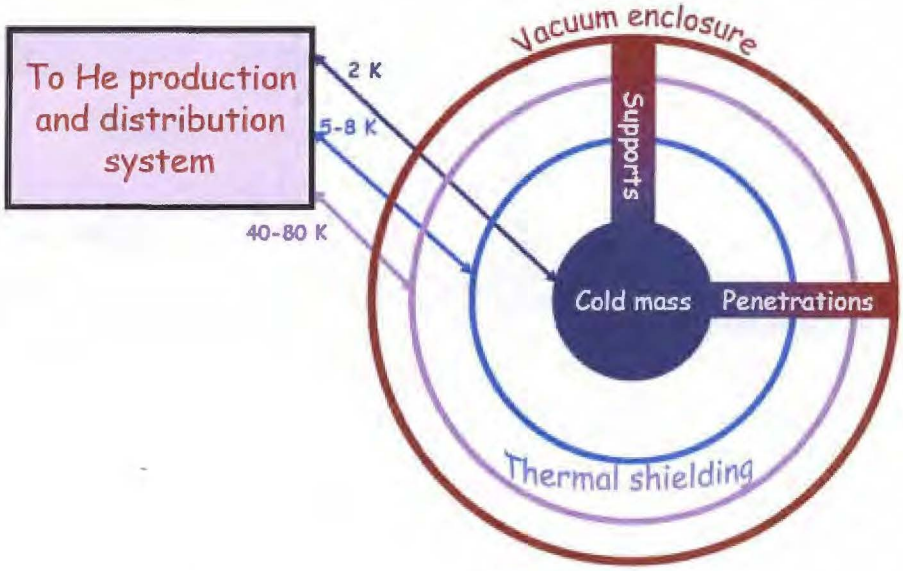

Fig. 2.13 – Conceptual scheme of the protection of the cryogenic environment

Thus the cryomodule provides:

- the cryogenic environment: the cavities and the magnets are immersed in a 2K temperature atmosphere;
- the shield for the sources of "parasitical" heat transfer from the room environment;
- the structural support of the cold mass, in order to provide precise alignment between the cavities

In order to minimize the heat losses and maximize the filling factor (the ratio between the real estate gradient and the cavity performances) long cryomodules, containing many cavities are preferred. For the existing accelerators a cryomodule consists of 8 or 9 cavities.

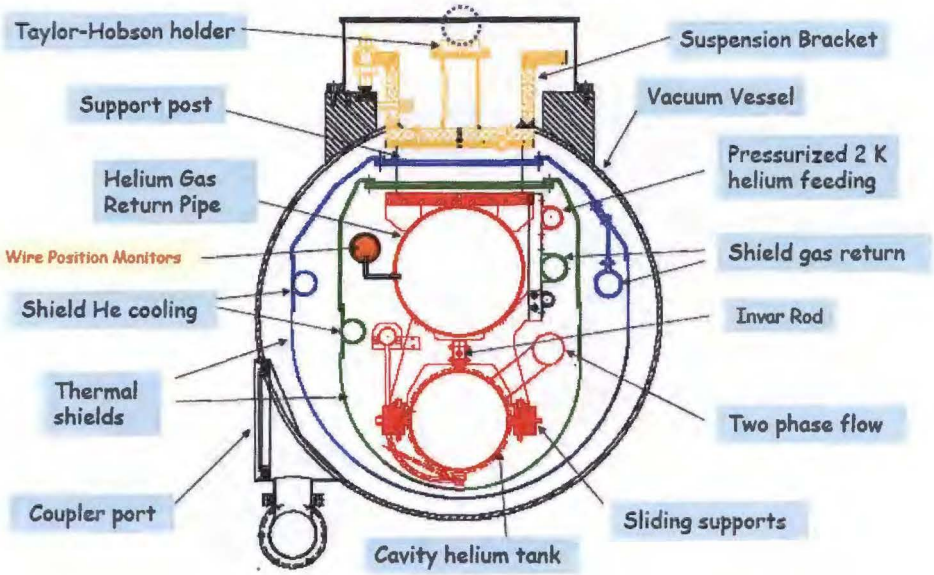

Fig. 2.14 – Cross section of the cryomodule: all the single parts of the cryogenic system are illustrated

The resulting cryomodule design is represented in Fig. 2.14 and 2.15.

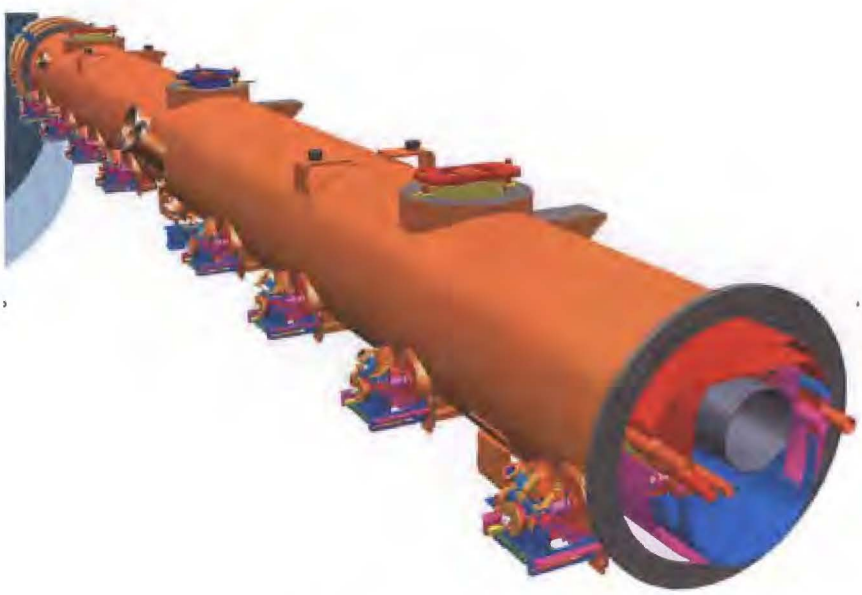

Fig. 2.15 – 3d view of the 1.3 GHz Cryomodule

3. THE ILC PROJECT AT FERMILAB

Fermilab is in the process of building the necessary infrastructure to fabricate, process, treat and test superconducting RF cavities for ILC R&D. Current ILC designs call for superconducting cavities with a gradient of 35 MV/m (megavolts per meter). Fermilab researchers are engaged in determining what combination of the three polishing techniques -- Electropolishing, Buffer Chemical Polishing and Tumbling -- should be used to build cavities with the necessary specifications. Once produced, assembling the cavities, inserting them into a cryomodule and transporting them to the ILC, no matter where it is sited, involves series of challenges that Fermilab researchers and technicians are actively engaged in tackling. A state-of-the-art clean room with a Class 10 area for cavity assembly has recently been built on site. Fermilab technicians have also overseen the transport of a cavity at vacuum from DESY and inserted it into a cryomodule. Fermilab accomplished this milestone without damaging the cavity and also provided the opportunity to test other cryomodule components developed at the lab.

The new facilities build for the support of the ILC R&D consist of a Vertical Test Stand, Horizontal Test Stand, Cryomodule Assembly Facility and ILC Test Area (see Fig. 3.1). The Vertical Test Stand and Horizontal Test Stand will be used to qualify cavities for ILC R&D. Inside the Crymodule Assembly Facility, which actually consists of two separate buildings, scientists will dress qualified cavities and string them together in a clean room environment. These strings of cavities then become fully assembled cryomodules, which will get tested in the ILC Test Area. Fermilab is currently in the process of constructing the ILC Test Area, where scientists will test a series of cryomodules with an electron beam.

Fig. 3.1 – Picture of the whole cryomodule inside the Fermilab's assembly area

In addition, Fermilab plans to develop a facility for chemically processing and treating superconducting cavities. Once the entire infrastructure is complete, Fermilab will have a full-service superconducting RF facility, where scientists from around the world will be able to process, assemble and test cavities and cryomodules from start to finish.

3.1 – The 1.3 GHz Helium vessel

At Fermilab, in order to perform the tests and to certificate the whole assembly, an 8-cavities structure (the 1.3 GHZ cryomodule, represented in Fig. 2.15) has been designed and will be entirely built.

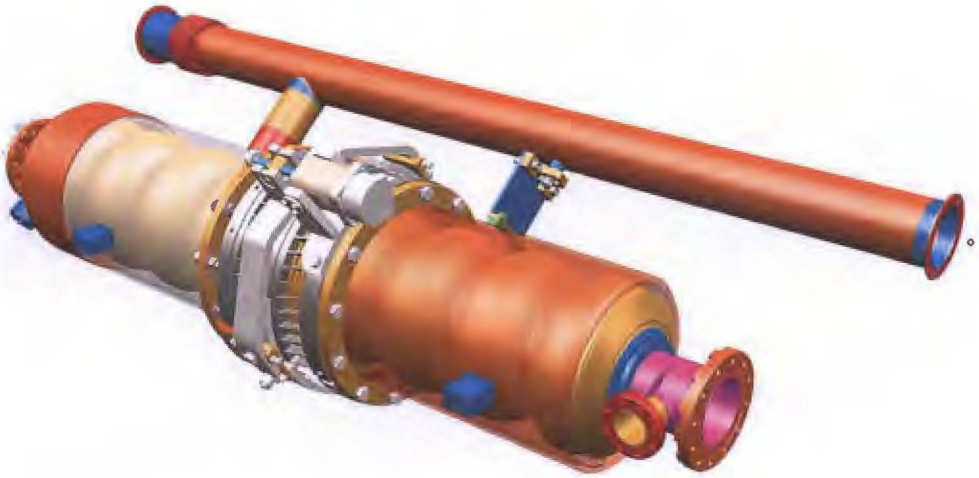

Fig. 3.2 – 3d draft of the 1.3 GHz cavity equipped with the Helium vessel and the first version of the blade-tuner

The superconducting cavity is represented below:

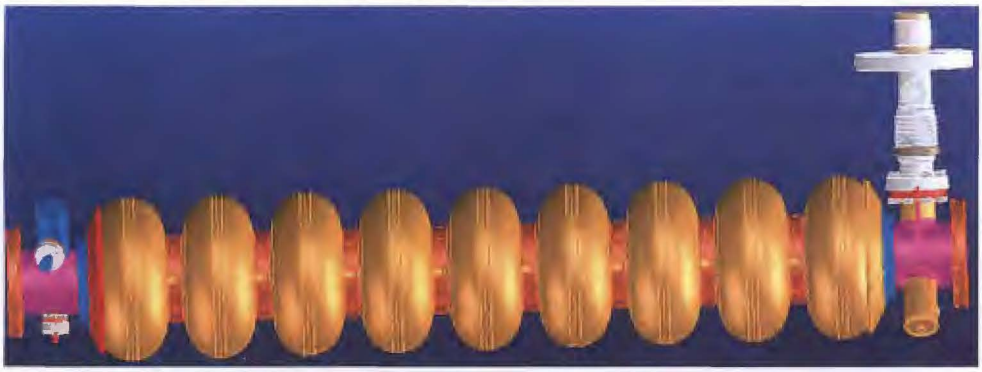

Fig. 3.3 – 3d draft of the 1.3 GHz cavity equipped with the reinforcing rings

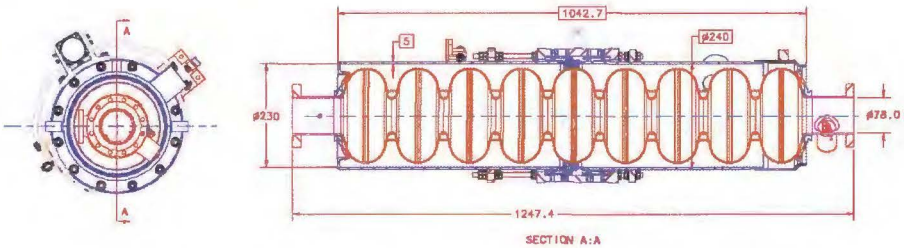

Fig. 3.4 – 2d draft representing the overall dimension of the 1.3GHz Helium vessel

On Fig. 3.5 a 2d axis-symmetric view of the 1.3 GHz He vessel is shown and the main components of this assembly are indicated as follow:

- superconducting cavity (component 1): this component has been described in the previous chapter and it is the core of this assembly;
- Helium vessel (component 2): this component has been introduced in order to keep the temperature as low as the superconducting regimen requires, so it "dresses" the superconducting cavity and a continuous 1.8°K superfluid Helium flow is held between the cavity and the vessel. This liquid flow is kept at a certain pressure that stresses all the weldings and components of the whole structure; the weldings themselves must assure the helium bounding, in order to have no helium leaks.

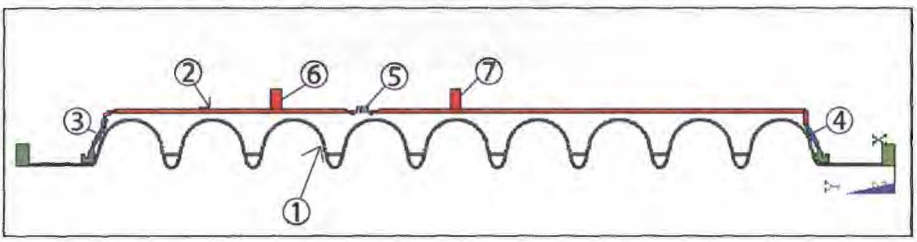

Fig. 3.5 – 2d axis-symmetric draft representing the 1.3GHz Helium vessel

- Tuning system (shown on Fig. 3.6): the introduction of this device is due to the problem of keeping the axial length constant. In fact the cavity, when it is subjected to the operating magnetic field, undergoes the LFD (Lorentz Force Detuning) phenomenon: this effect causes a reduction of the axial length of the cavity and the loss of its initial geometric parameters. In order to compensate the LFD and restore the original resonating structure a tuning system has been introduced: this device acts on the helium vessel's flanges (components 6 and 7 on Fig. 3.5) with a screw-operated engine and relatively moves them. This component will be treated and described on Chapter 7.
- Bellow (component 5, shown also on Fig. 3.6): this component has been introduced between the two flanges and divides the Helium vessel into two parts creating a concentrated compliance, so that it allows to reduce the force due to the stretching and shrinkage of the cavity

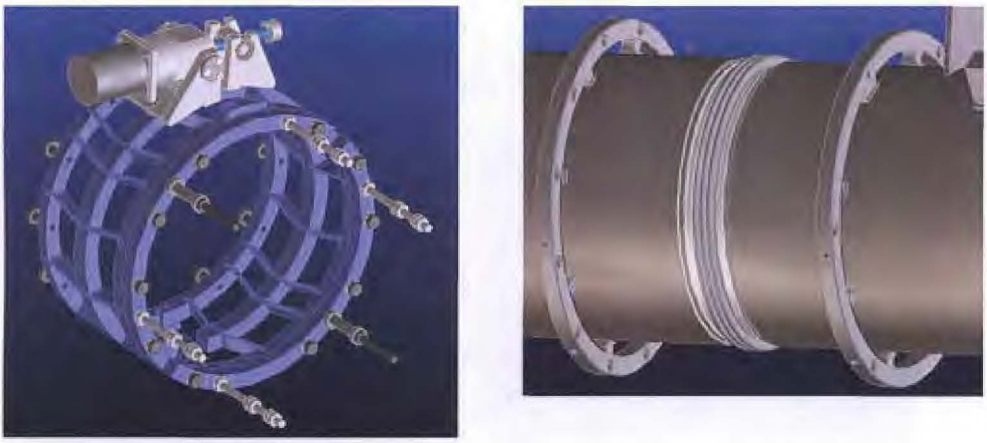

Fig. 3.6 – Drafts of the latest version of the blade-tuner (on the left) and of the flanges where the blade-tuner will be linked to the Helium vessel

- End-caps (components 3 and 4): the choice of the titanium composition for the Helium vessel is due to the bad weldability of the niobium with the other materials. In fact the only possibility of welding the niobium (keeping also an acceptable reliability for the joint's mechanical properties) with the vessel is the introduction of an intermediate alloy (whose composition recalls both the cavity and the vessel material) that can be joined with both the materials: titanium has been chosen because the titanium-niobium alloy is industrially available and owns acceptable mechanical properties. A titanium-niobium end-cap has been finally introduced to separate the cavity from the Helium vessel, so both the titanium/titanium-niobium and niobium/titanium-niobium materials can be performed with an EB welding. Whereas the titanium-titanium weldings are performed with a TIG process. This component will be treated and described on Chapter 5.

The EBM welding process has been studied performing some samples in order to assess the welding parameters and the weld shrinkage; this welding is performed into a vacuum machine to obtain the best results.

In the picture below (see Fig. 3.7) all these welds are illustrated:

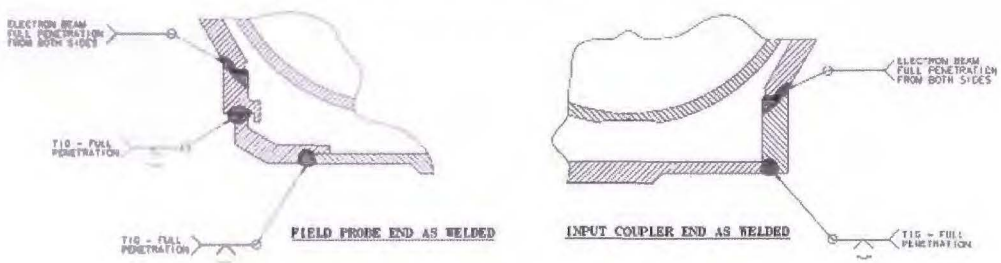

Fig. 3.7 – Schemes of the welds that are supposed to be executed between the titanium/niobium end-cap and the titanium disk and between the titanium disk and the titanium shell for the field probe end and the coupler end of the 1.3GHz Helium vessel

The TIG welding is an important process, because it's necessary to obtain a full penetration joint and avoid oxygen inclusions into the welding. In order to achieve these goals the Glove Box has been introduced (see Fig. 3.8): the welder performs this operation with the 2 joints staying in an oxygen-free atmosphere, that is kept inert by an argon continuous flux.

Fig. 3.8 – Sample of the execution of the TIG welding inside the Glove Box (on the left) and picture of the Glove Box (on the right)

3.2 – FEM analyses performed on the 1.3GHz Helium vessel

The finite element analyses that have been done on the 1.3GHz Helium vessel will be listed and briefly described below, and then will be wholly described in the next chapters.

- Analysis of the resistance of the vessel: the vessel has been loaded with the operating load condition and the resulting stresses have been compared with the allowable stresses given by the ASME code;
- Analysis of the end-cap press-work: the press-work process has been completely studied in order to assess the end-cap's elastic return and rightly design the casts;
- Analysis of the stiffness and efficiency of the vessel: the vessel has been analysed in order to assess his efficiency and an attempt to optimize it has been performed;
- Analysis of the blade-tuner: the blade-tuner has been loaded with the operating loads and his elastic behaviour has been studied, then the tuning limits have been determined.

All these analyses have been performed using the Ansys Classic calculation code except the 3d stress one and the nonlinear buckling one that was performed by using the Ansys Workbench software.

4. ANALYSIS OF THE RESISTANCE OF THE 1.3 GHz HELIUM VESSEL

The analysis of the resistance of the 1.3GHz Helium vessel (He-vessel) consists of the following studies:

- Static analysis of the He-vessel 3d FEA model;
- Static analysis of the He-vessel 2d harmonic FEA model;
- Buckling analysis of the cavity

4.1 – Load conditions

The He-vessel has been analyzed under these load conditions:

- 0.4MPa inner pressure;
- 0.4MPa inner pressure and 0.5mm flange displacement;
- 0.4MPa inner pressure, 0.5mm flange displacement and -269°C cooling

The 1st load case allows to study the behavior of the vessel itself under the working pressure given by the liquid helium pressurized continuous flow: there are no loads coming from the blade-tuner; the 2nd load case introduces the loads coming from the blade-tuner: in order to analyze the most dangerous loading condition bound to the blade-tuner's action and in order to use the most precautionary approach, the flanges has been modeled as two flat disks linking the vessel and the blade-tuner, so the flanges themselves are more rigid than they are in reality, in order to maximize the force that is necessary for moving them. In fact in a more realistic model the blade-tuner's forces should be applied only on 4 holes (where the piezoelectric sensors are), and this configuration implicate a higher vessel's compliance and lower stresses.
The 3rd load case allows to study the vessel under the blade-tuner action when the vessel's inner temperature is about 4°K: even this load case, as the previous one, is applied in both the blade-tuner different kinds of action (extension or shrinkage).
In order to perform a fully comprehensive analysis it is necessary to consider the effects of the hydrostatic pressure and the vessel's proper weight: these loads aren't axisymmetric, so a simple 2d axisymmetric analysis isn't able to represent them.

4.2 – 3d FEA analysis

The 3d FEA model is shown below:

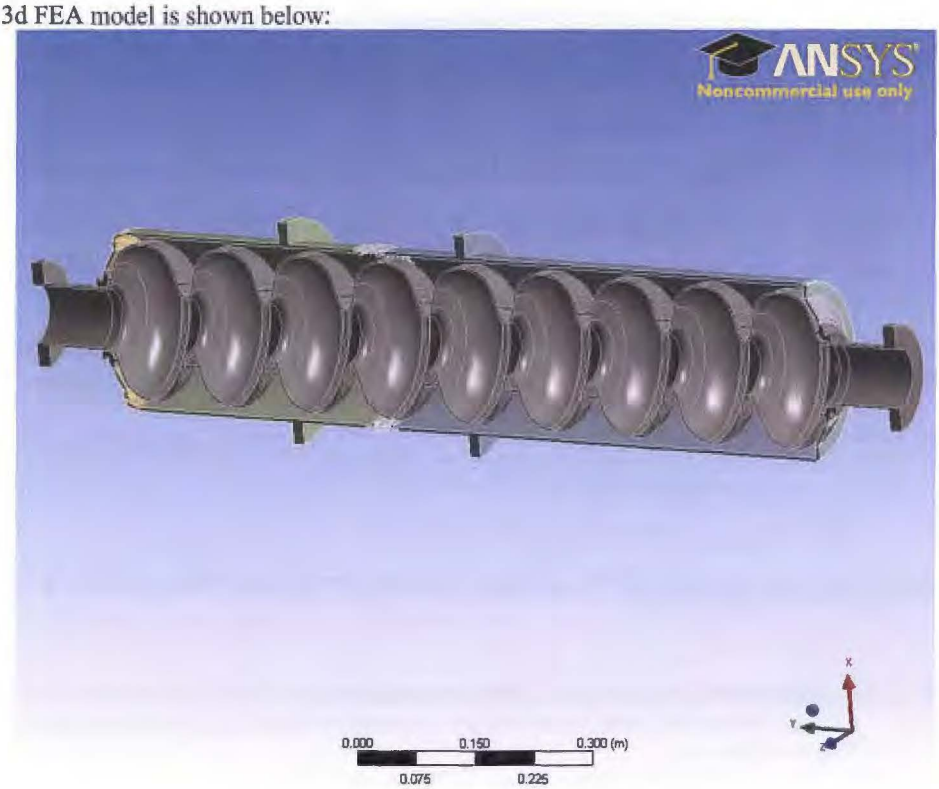

Fig. 4.1 – 3d model used for the finite elements analysis

The advantage of this analysis is that both the vessel's weight and the hydrostatic pressure can be taken in account into the model, in order to obtain more comprehensive results. Besides all these loads have been easily introduced into the model because of its tri-dimensional nature.
As it can be seen in the picture above, in order to reduce the CPU time a symmetrical boundary condition has been introduced: the resulting Finite Element model consist of about 17000 brick elements (the most recurrent kind of element for mechanical 3d analyses) and about 150000 nodes.
The map of the von Mises stresses for the 3rd load condition is shown below: this choice is due to the possibility of comparing the results with the yielding strength of the materials.

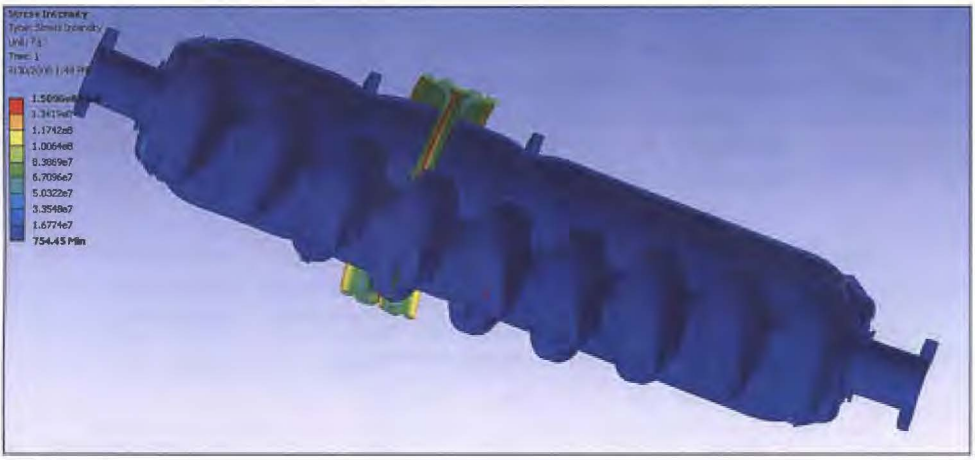

Fig. 4.2 – von Mises stresses in the 3rd load condition

The results for all the load conditions are listed in the tables below:

No	Area	Stress with pressure only (MPa)	Stress with pressure and moving away displacement (MPa)	Stress with pressure and approaching displacement (MPa)	Yelding stresses (MPa)
4	Ti Bellow	147	227	189	233
7	Ti-Nb endcap	29	23	32.2	22
8	Nb cavity	34	62	21.5	76

Table 4.3 – Results in the 1st and 2nd load conditions and comparison with the yielding strengths

No	Area	Stress with pressure, cool down and moving away displacement (MPa)	Stress with pressure, cool down and approaching displacement (MPa)	Yelding stresses (MPa)
4	Ti Bellow	247	247	233
7	Ti-Nb endcap	29	35.9	500
8	Nb cavity	34	85	38

Table 4.4 – Results in the 3rd load conditions and comparison with the yielding strengths

In order to check the results achieved with the 3d model, a 2d simple model loaded with the pressure only has been introduced: this model is the same as the one used for the harmonic analysis

(see the next paragraph 4.3.2 for its description) with the only difference that the analyses are performed in an axis-symmetric regimen.
Comparing the 2d model results with the 3d model one, it has been possible to see that the differences between the two models are very low and only depend by the element size, obviously lower for the 2d model, the effects of the hydrostatic pressure and of the vessel's weight don't have a great influence on the vessel's behavior.

No	Area	Stress with only pressure (MPa) – 2d model	Stress with only pressure (MPa) – 3d model	Stress with pressure and displacement (MPa) – 2d model	Stress with pressure and displacement (MPa) – 3d model
1	Ti-Nb endcap	40	30	32	24
4	Ti Bellow	147	150	227	233
7	Ti-Nb endcap	29	28	23	22
8	Nb cavity	34	38	62	76

Table 4.5 – Comparison between the 3d and 2d analyses for the 1st and 2nd load conditions

4.3 – 2d harmonic FEA model

In order to completely assess the linearized stresses for the He-vessel and to use an adequately small mesh size, it's necessary to use a different approach: the vessel, in fact, can be modeled as an axisymmetric non axisymmetrically loaded body.
Before explaining how the analysis has been performed, it could be very helpful to briefly explain the ASME section VIII code guidelines for the finite element analyses and certification of pressurized vessels, as well as the guidelines about the way to find the materials' allowable stresses starting from the yielding and ultimate strengths.

4.3.1 – ASME Code guidelines

The ASME (American Society of Mechanical Engineers) is a professional body focused on mechanical engineering born in response to numerous steam boiler pressure vessel failures: this society is famous for setting codes and standards for mechanical devices (such as pressurized vessels).
Accordingly to the ASME code, the analysis of the 1.3GHz Helium vessel consists of two steps:

- Determination of the materials' allowable stresses;
- Determination of the linearized stresses along the structure to be analyzed

4.3.1.1 – Determination of the allowable stresses

The procedure to determine the materials' allowable stresses is described in the Tab. 1.100, mandatory apex 1, Section II, Part D of the ASME code. The allowable stresses are determined since the values of the yielding and ultimate strengths. For wrought or cast ferrous and nonferrous materials it is the minimum value between the results of the formulas shown below:

$$S = min[\frac{Su}{3.5}; \frac{2}{3} \cdot Sy]$$

Su is the ultimate strength, while Sy is the yielding strength.
For welded pipes or tubes (ferrous or nonferrous material) the value S must be scaled by a 0.85 factor.

- Titanium grade 2

The mechanical properties are listed below: in the He-vessel the titanium pipe is welded to the titanium-niobium end-caps, so it is necessary to use the scaling factor introduced above.

$$Su = 344\,MPa \rightarrow S = 83\,MPa$$

$$Sy = 275\,MPa \rightarrow S = 156\,MPa$$

The most conservative Allowable Stress S has been selected, and it has been moreover multiplied by a factor 0.8, obtaining the new allowable that will be used during the FE analysis.

$$S = 0.8 \cdot 83 = 66.4\,MPa$$

- High RRR Niobium

Below is a summary of the niobium material data for an 800 C bake of three hours from JLAB-TN-02-01, "High RRR Niobium Material Studies," by Ganapati Myneni and Peter Kneisel, Jefferson Lab. This paper has an extensive tabulation of yield and ultimate strength numbers for niobium of various heat treatments, including several at 800 C.

						ASME Sec VIII, Div 1		Fermilab FESHM
Mat'l	YS	TS	% elong	approx RRR	heat	allowable stress		allowable stress
						Take the smaller of:		ASME x 0.8
						2/3 x YS	TS/ 3.5	
	MPa	MPa				MPa	MPa	Mpa
WCL SNS prototype sample 10	40.7	163	50	400	800 C 3 hr	29	45	23
WCL SNS prototype sample 11	41.3	154	60	400	800 C 3 hr	29	45	23
WC SNS production sample 19	44.8	147	59	400	800 C 3 hr	33	43	27
WC SNS production sample 20	48.9	148	--	400	800 C 3 hr	33	43	27
TD SNS production sample 28	37.9	157	41	300	800 C 3 hr	25.2	49	20
TD SNS production sample 29	37.9	151	40	300	800 C 3 hr	25.2	43	20
3.9 GHz cavity 5	*38 est*	*140 est*	--	300	825 C 2.4 hr	25	40	20

Table 4.6 – Niobium material data given by the vendor

The 800 C bake was of particular concern to JLab due to the evidence of softening of the niobium (yield strength reduction) at that temperature. These data are both the most nearly representative of our material which we have found in the niobium material literature, and also the most conservatively low numbers for any bake-out temperature, including higher temperatures.
The conclusion is to take as the allowable stress: S=22Mpa

- Titanium-Niobium

The alloy's composition is 55% Titanium - 45% Niobium. The mechanical properties of this material were given by the vendor (ATI Wang Chang). The allowable stress is indicated below.

$$Su = 546\,MPa \rightarrow S = 132.6\,MPa$$

$$Sy = 480\,MPa \rightarrow S = 272\,MPa$$

Even in this case the 0.8 scaling factor is applied on the most conservative value of the allowable stress.

$$S = 0.8 \cdot 132.6 = 106\,MPa$$

4.3.1.2 - Determination of the linearized stresses

In order to perform the certification of the He-vessel an elastic analysis is required, so the allowable stresses found in the above chapter must be compared with the stresses acting into the structure.

The ASME stress categories and the symbols used to denote them in the code are given below:

- Primary Stress: can be divided in General Primary Membrane Stress (Pm), Local Primary Membrane Stress (PL) and Primary Bending Stress (Pb)
- Secondary Stress, Q
- Peak Stress, F

and this categorization depends on location, origin and type.
The membrane stress is the component of stress that is uniformly distributed and equal to the average value of stress across the thickness of the section under consideration; the bending stress is the component of stress that varies linearly across the thickness of section under consideration.
A primary stress is a stress produced by mechanical loading only and is so distributed in the structure that no redistribution of load occurs as a result of yielding. It is a normal stress or a shear stress developed by the imposed loading, that is necessary to satisfy the simple laws of equilibrium of external and internal forces and moments. The basic characteristic of this stress is that it is not self-limiting. Primary stresses that considerably exceed the yield strength will result in failure, or at least in gross distortion. A thermal stress is not classified as a primary stress.
Primary stresses are divided into 'general' and 'local' categories.
The Primary Local Membrane Stress arises in cases in which a membrane stress produced by pressure or other mechanical loading and associated with a primary together with a discontinuity effect produces excessive distortion in the transfer of load to other portions of the structure.
Conservatism requires that such a stress be classified as a primary local membrane stress even though it has some characteristics of a secondary stress.
Secondary stresses are stresses developed by constraints due to geometric discontinuities, by the use of materials of different elastic moduli under external loads, or by constraints due to differential thermal expansion. The basic characteristic of secondary stress is that it is self-limiting. Local yielding and minor distortions can satisfy the conditions that cause the stress to occur and failure from one application of the stress is not to be expected.
Peak stress is that increment of stress which is additive to the primary-plus-secondary stresses by reason of local discontinuities or local thermal stress including the effects (if any) of stress concentration.
Accordingly with the ASME code, the intensity stresses (arising from the Tresca equivalent stress) must be analyzed and compared with the allowable: this choice allows to be more conservative in the assessment of the stresses.
The linearization must be performed along the thickness in the mid-section of every component and in all the connection zones of the structure. A typical rate of the linearized stresses is shown in the picture below.

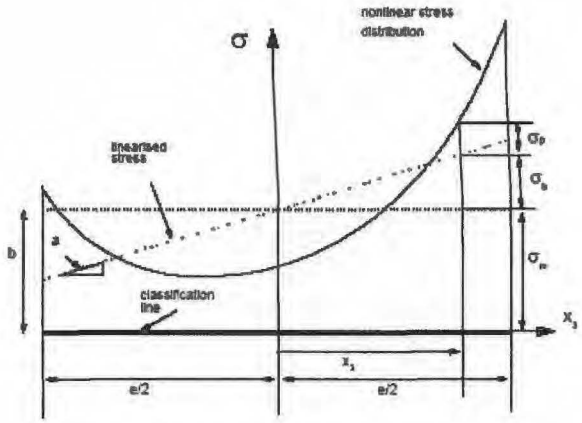

Fig. 4.3 – Typical rate of the linearized stresses along a section

When all the membrane, bending and peak stresses have been determined, they must be compared with the material's allowable. The acceptance criteria are shown below.

$$Pm \leq S$$

$$Pm + Pb \leq 1.5 \cdot S$$

$$Pm + Pb + Q \leq 3 \cdot S$$

Where Q represents the stresses due to the temperature variation.

4.3.2 – Model description

Since the harmonic elements are bi-dimensional, the mesh used all along the vessel is much finer than the 3d model: in fact it has been possible to fill every area with at least 3 elements along all the components' thicknesses. In the picture below the finite element model and the resulting mesh are displayed.

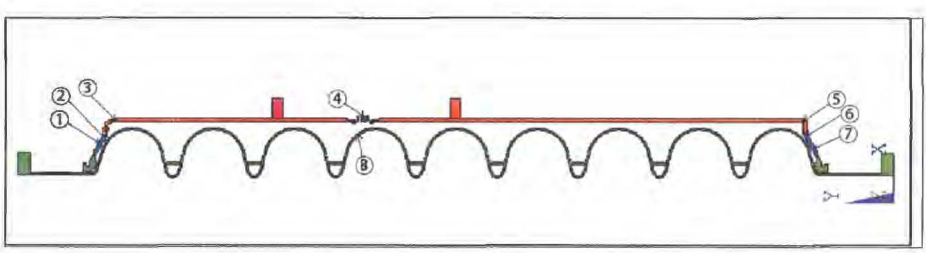

Fig. 4.4 – 2d FEA model used for the harmonic analysis

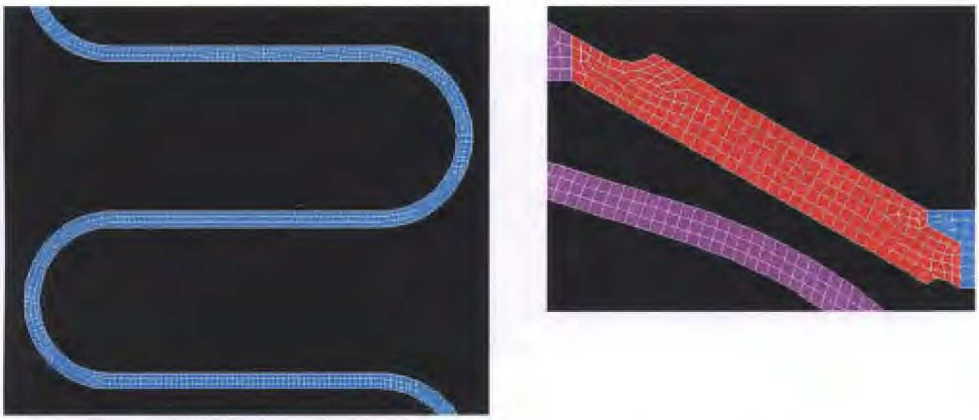

Fig. 4.5 – mesh introduced for the harmonic model: the bellow (on the left) and the end-cap (on the right) are shown

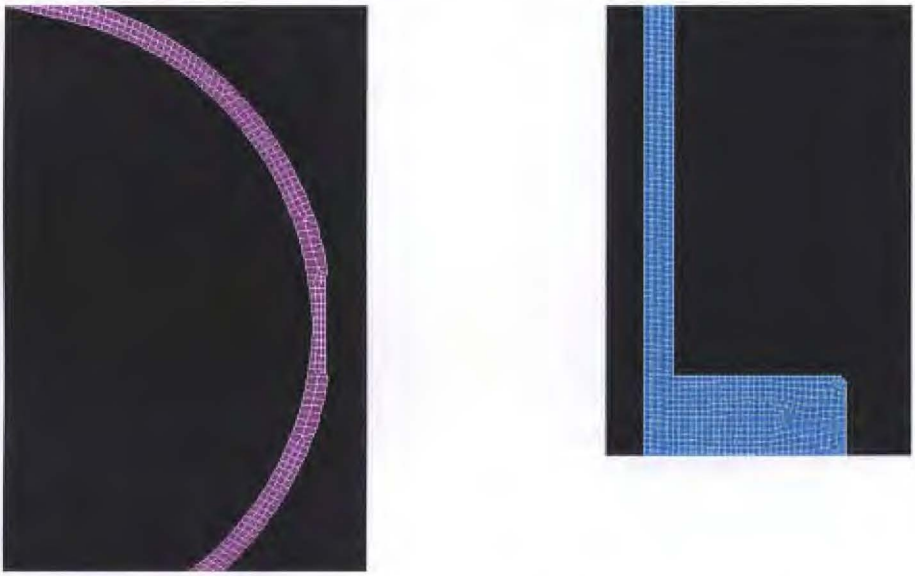

Fig. 4.6 – mesh introduced for the harmonic model: the cavity (on the left) and the vessel with the flange (on the right) are shown

In order to study the behavior of the vessel when it bears the non-axisymmetric loads the harmonic properties of the plane-83 element were used: these kind of element allows the introduction of intermediate nodes that provide a more accurate result.
The own weight has been introduced into the model as a gravity acceleration with a sinusoidal rate along the vessel's circumference on its x and z (radial and circumferential) coordinates: this simple procedure is more clearly explained by the picture shown below.

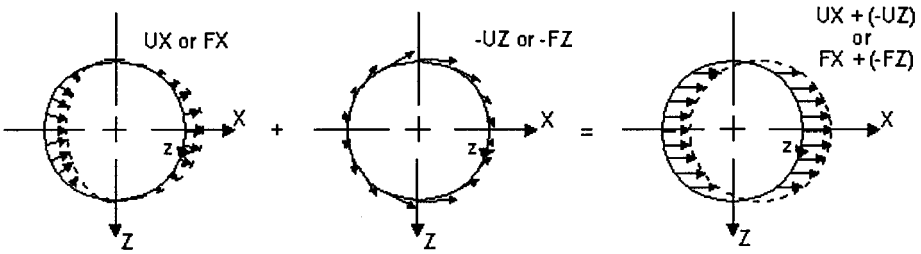

Fig. 4.7 – Procedure used for treating the weight the addition of two axis-symmetric functions

An analysis of the 2d harmonic model of the vessel loaded with the own weight only has been performed and the results were compared with the 3d model. The comparison is shown below.

Material	Comparison item	2d harmonic	3d	Ratio
Titanium	Maximum Von Mises stress (MPa)	1,56	1,73	0,9
	Maximum x component of displacement (μm)	3,24	3,25	1
	Maximum y component of displacement (μm)	1,29	1,32	0,97
Titanium-Niobium	Maximum Von Mises stress (MPa)	1,38	1,68	0,82
	Maximum x component of displacement (μm)	3,83	3,84	1
	Maximum y component of displacement (μm)	2,76	2,83	0,98
Niobium	Maximum Von Mises stress (MPa)	5,48	7,76	0,71
	Maximum x component of displacement (μm)	93,3	94,3	0,99
	Maximum y component of displacement (μm)	26,9	27,2	0,99

Table 4.7 – Comparison between harmonic model and 3d one loaded with the own weight only

The maximum difference between the displacements in the 2 models is about the 3.5%, while for the equivalent stresses it is higher (about the 35%) due to the different mesh sizes for the elements: in fact this important parameter influences the stresses results much more than the displacements results because the stress values show a convergent rate when the element size is being reduced, while the displacements don't show this behavior.
Besides it wasn't possible for the 3d model to control the elements distribution on the meshed areas, so even using the same element size the results are different.

The hydrostatic pressure has been introduced into the model as the addition of a constant pressure and a pressure with a sinusoidal rate along the vessel's circumference on its x and z (radial and circumferential) coordinates: this simple procedure is more clearly explained by the picture shown below.

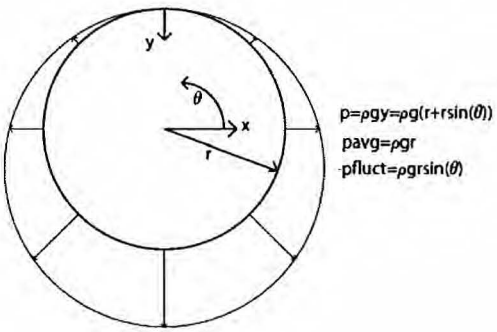

Fig. 4.8 – Procedure used for treating the hydrostatic pressure as the addition of two axis-symmetric functions

The hydrostatic pressure has this rate along the y axis:

$$p = \rho \cdot g \cdot h$$

In order to fit this formula to the harmonic model of the vessel it's useful to convert it into cylindric coordinates.

$$p(\theta) = \rho \cdot g \cdot r \cdot (1 + \sin(\theta))$$

As introduced above, the pressure presents two components: the first is constant along the circumference angle, while the second has got a sinusoidal rate. These loads were both included into the model in order to perform an analysis, compare the results with the 3d model loaded with the hydrostatic pressure only and obtain a data sheet that is very similar to the one made above. The results are shown below.

Material	Comparison item	2d harmonic	3d	Ratio
Titanium	Maximum Von Mises stress (MPa)	0,3	0,29	1,05
	Maximum x component of displacement (μm)	0,110	0,1	1,100
	Maximum y component of displacement (μm)	0,23	0,21	1,13
Titanium-Niobium	Maximum Von Mises stress (MPa)	0,25	0,3	0,85
	Maximum x component of displacement (μm)	0,11	11,1	0,01
	Maximum y component of displacement (μm)	0,49	0,54	0,91
Niobium	Maximum Von Mises stress (MPa)	1,45	1,58	0,92
	Maximum x component of displacement (μm)	1,5	1,64	0,91
	Maximum y component of displacement (μm)	4,4	4,81	0,91

Table 4.8 – Comparison between harmonic model and 3d one loaded with the hydrostatic pressure only

The maximum difference between the displacements in the 2 models and the displacements in the 3d model is about the 10%, while for the equivalent stresses it is not much higher (about the 16%). The flanges displacements, together with the inner pressure and the thermal load have been applied as axi-symmetric loads and the results should be very close with the 3d model's: thus in order to compare the differences between the 2d harmonic and 3d results with a reference value it's a good idea to determine the maximum differences found in a "sample problem" (the only pressure case itself). The results are shown below

Material	Comparison item	2d harmonic	3d	Ratio
Titanium	Maximum Von Mises stress (MPa)	118,6	126,2	0,94
	Maximum x component of displacement (μm)	62,3	62,8	0,99
	Maximum y component of displacement (μm)	56,8	59,5	0,95
Titanium-Niobium	Maximum Von Mises stress (MPa)	23,1	29	0,8
	Maximum x component of displacement (μm)	6,84	7,13	0,96
	Maximum y component of displacement (μm)	43,4	44,3	0,98
Niobium	Maximum Von Mises stress (MPa)	28,1	25,5	1,1
	Maximum x component of displacement (μm)	5,91	5,89	1
	Maximum y component of displacement (μm)	36,1	39,8	0,91

Table 4.9 – Comparison between harmonic model and 3d one loaded with the oinner pressure only

Once the comparison with the "sample problem" has been done it's clear that the differences between 2d harmonic and 3d model in the 2 tests are the same as in the sample test. Now the model is ready to describe the behavior of the vessel under the 3 load cases.

4.3.3 – Loads and constraints

Since the finite element solver is able to perform the analysis on a certain harmonic mode only, 2 load steps have to be introduce: in the first one all the 0-harmonic loads (such as the inner pressure, the constant component of the hydrostatic pressure, the thermal load and the flange's displacement) have been defined, while in the second one all the 1-harmonic loads (such as the fluctuating component of the hydrostatic pressure and the own weight) have been defined.
In the following images the way the loads were applied on the vessel is fully explained for each load step.

- First load case

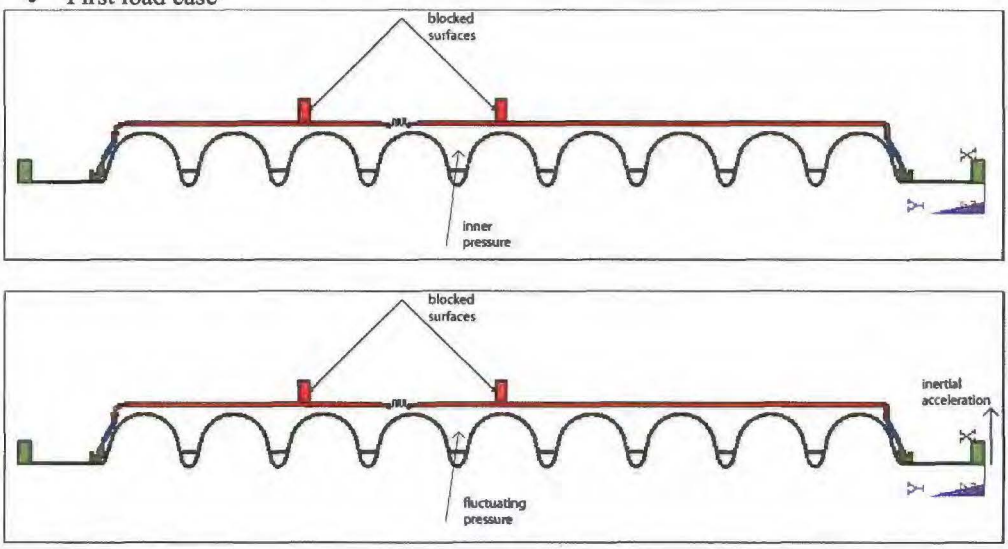

Fig. 4.9 – Loads configuration for the 1st load condition: the axis-symmetric (upper image) and the harmonic (lower image) loads are shown. These loads are finally added in order to determine the cumulative solution

- second load case

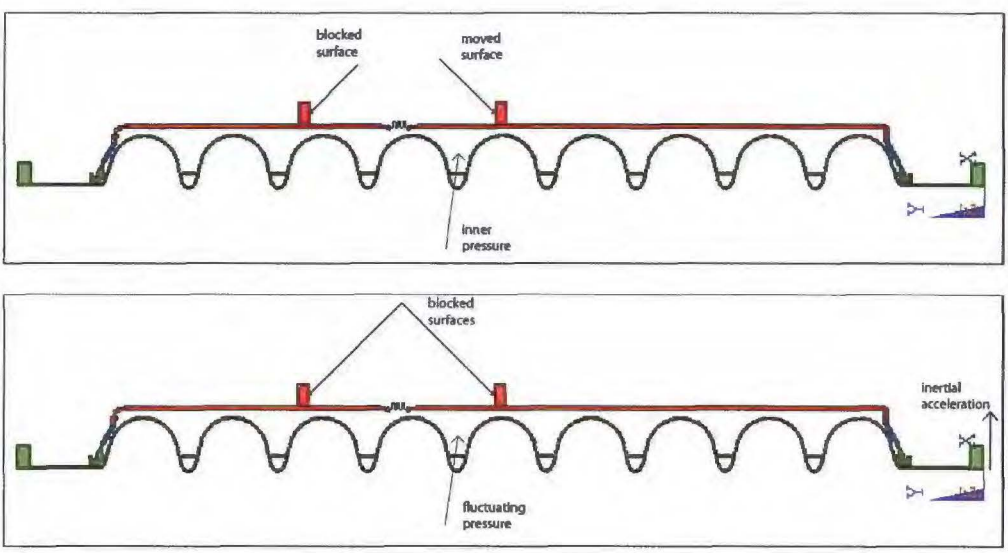

Fig. 4.10 – Loads configuration for the 2nd load condition: the axis-symmetric (upper image) and the harmonic (lower image) loads are shown. These loads are finally added in order to determine the cumulative solution

- third load case

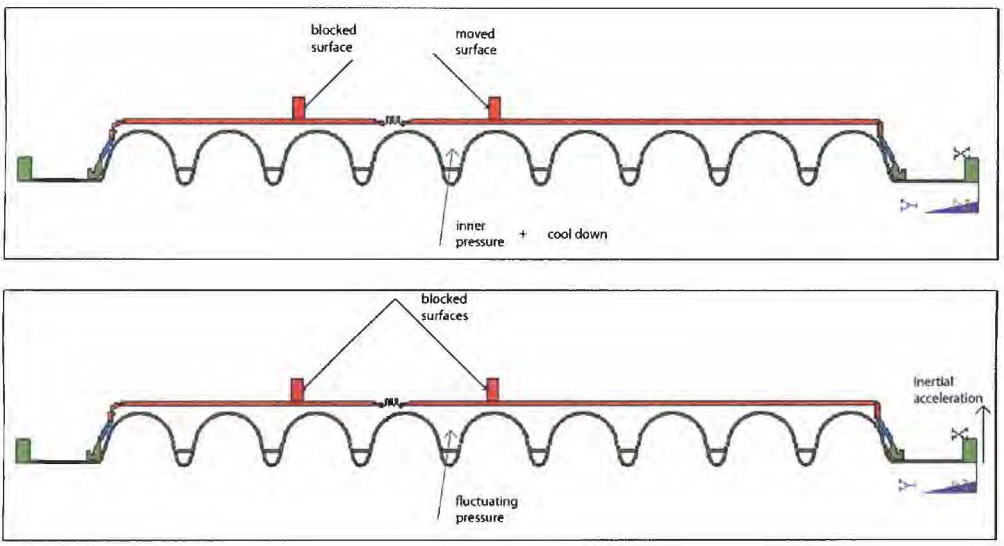

Fig. 4.11 – Loads configuration for the 3rdload condition: the axis-symmetric (upper image) and the harmonic (lower image) loads are shown. These loads are finally added in order to determine the cumulative solution

4.3.4 – Results list

In agreement with the ASME Code, Part VIII, Division 2, Annex 5.A, the Intensity Stress has been linearized along proper Stress Classification Lines (SCLs). Two sets of SCLs for each component of the assembly have been used.
A first set (a,c,d,e,f,k,l,m,n,p,q,r,s) crossing the contact edge between two adjacent components. Usually the highest stress in a component is located in the contact region with the adjacent component due to the local structural discontinuities.
A second set of SCLs (b,g,h,i,j,o) crossing each component in a mid-section.

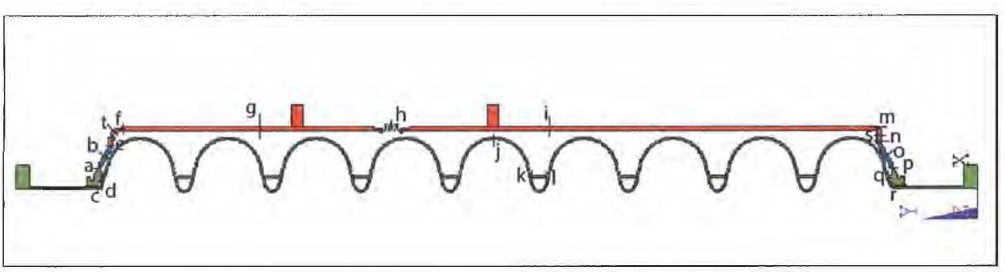

Fig. 4.12 – Stress classification lines for the 2d harmonic model

The linearized stresses will be divided into two categories (membrane and membrane+bending stresses) and listed below.

- First load case, membrane linearized stresses

SCL	Component and evaluation region	Material	Stress value	Allowable stress
a	Cavity: cavity/Ti-niobium joint, weld area	High RRR Niobium	4,83	22
b	Ti-Nb joint: mid section	Titanium 55% Niobium 45%	5,26	106
c	Cavity: cavity/niobium joint, weld area	High RRR Niobium	3,95	22
d	Cavity: cavity/niobium joint, weld area	High RRR Niobium	10,08	22
e	Ti-Nb joint: Ti-Nb/titanium ring, weld area	Titanium 55% Niobium 45%	16,33	66,4
f	Titanium shell: Ti shell/Ti ring joint, weld area	Titanium Grade 2	5,31	66,4
g	Titanium shell: mid section	Titanium Grade 2	5,8	66,4
h	Bellow: central convolution	Titanium Grade 2	40,7	66,4
i	Titanium shell: mid section	Titanium Grade 2	9,41	66,4
j	Cavity: iris, mid section	High RRR Niobium	7,56	22
k	Cavity: cavity/reinforcing ring joint, weld zone	High RRR Niobium	8,32	22
l	Cavity: cavity/reinforcing ring joint, weld zone	High RRR Niobium	9,17	22
m	Titanium shell: Ti shell/Ti ring joint, weld area	Titanium Grade 2	33,6	66,4
n	Ti-Nb joint: Ti-Nb/titanium ring, weld area	Titanium 55% Niobium 45%	15,42	106
o	Ti-Nb joint: mid section	Titanium 55% Niobium 45%	5,81	106
p	Cavity: cavity/Ti-niobium joint, weld area	High RRR Niobium	5,1	22
q	Cavity: cavity/niobium joint, weld area	High RRR Niobium	10,38	22
r	Cavity: cavity/niobium joint, weld area	High RRR Niobium	4,34	22
s	Titanium ring, mid section	Titanium grade 2	5,64	66,4
t	Titanium ring, mid section	Titanium grade 2	4,65	66,4

Table 4.10 – Membrane linearized stresses for the 1st load condition and comparison with the allowable stresses

- First load case, membrane+bending linearized stresses

SCL	Component and evaluation region	Material	Stress value	Allowable stress
a	Cavity: cavity/Ti-niobium joint, weld area	High RRR Niobium	16,92	33
b	Ti-Nb joint: mid section	Titanium 55% Niobium 45%	17,01	159
c	Cavity: cavity/niobium joint, weld area	High RRR Niobium	7,13	33
d	Cavity: cavity/niobium joint, weld area	High RRR Niobium	19,86	33
e	Ti-Nb joint: Ti-Nb/titanium ring, weld area	Titanium 55% Niobium 45%	27,6	99,6
f	Titanium shell: Ti shell/Ti ring joint, weld area	Titanium Grade 2	6,79	99,6
g	Titanium shell: mid section	Titanium Grade 2	6,3	99,6
h	Bellow: central convolution	Titanium Grade 2	128,2	99,6
i	Titanium shell: mid section	Titanium Grade 2	9,81	99,6
j	Cavity: iris, mid section	High RRR Niobium	10,5	33
k	Cavity: cavity/reinforcing ring joint, weld zone	High RRR Niobium	21,2	33
l	Cavity: cavity/reinforcing ring joint, weld zone	High RRR Niobium	19,84	33
m	Titanium shell: Ti shell/Ti ring joint, weld area	Titanium Grade 2	54,6	99,6
n	Ti-Nb joint: Ti-Nb/titanium ring, weld area	Titanium 55% Niobium 45%	27,2	159
o	Ti-Nb joint: mid section	Titanium 55% Niobium 45%	18,12	159
p	Cavity: cavity/Ti-niobium joint, weld area	High RRR Niobium	19,43	33
q	Cavity: cavity/niobium joint, weld area	High RRR Niobium	18,82	33
r	Cavity: cavity/niobium joint, weld area	High RRR Niobium	8,2	33
s	Titanium ring, mid section	Titanium grade 2	15,63	99,6
t	Titanium ring, mid section	Titanium grade 2	12,14	99,6

Table 4.11 – Membrane+bending linearized stresses for the 1st load condition and comparison with the allowable stresses

- Second load case, membrane linearized stresses with approaching flanges:

SCL	Component and evaluation region	Material	Stress value	Allowable stress
a	Cavity: cavity/Ti-niobium joint, weld area	High RRR Niobium	7,07	22
b	Ti-Nb joint: mid section	Titanium 55% Niobium 45%	5,16	106
c	Cavity: cavity/niobium joint, weld area	High RRR Niobium	5,14	22
d	Cavity: cavity/niobium joint, weld area	High RRR Niobium	7,95	22
e	Ti-Nb joint: Ti-Nb/titanium ring, weld area	Titanium 55% Niobium 45%	20,6	66,4
f	Titanium shell: Ti shell/Ti ring joint, weld area	Titanium Grade 2	8,4	66,4
g	Titanium shell: mid section	Titanium Grade 2	7,8	66,4
h	Bellow: central convolution	Titanium Grade 2	46,6	66,4
i	Titanium shell: mid section	Titanium Grade 2	9,41	66,4
j	Cavity: iris, mid section	High RRR Niobium	10,15	22
k	Cavity: cavity/reinforcing ring joint, weld zone	High RRR Niobium	11,04	22
l	Cavity: cavity/reinforcing ring joint, weld zone	High RRR Niobium	10,86	22
m	Titanium shell: Ti shell/Ti ring joint, weld area	Titanium Grade 2	29	66,4
n	Ti-Nb joint: Ti-Nb/titanium ring, weld area	Titanium 55% Niobium 45%	18,78	106
o	Ti-Nb joint: mid section	Titanium 55% Niobium 45%	5,63	106
p	Cavity: cavity/Ti-niobium joint, weld area	High RRR Niobium	7,34	22
q	Cavity: cavity/niobium joint, weld area	High RRR Niobium	6,74	22
r	Cavity: cavity/niobium joint, weld area	High RRR Niobium	5,7	22
s	Titanium ring, mid section	Titanium grade 2	6,21	66,4
t	Titanium ring, mid section	Titanium grade 2	9,05	66,4

Table 4.12 – Membrane linearized stresses for the 2nd load condition and comparison with the allowable stresses

- Second load case, membrane + bending linearized stresses with approaching flanges

SCL	Component and evaluation region	Material	Stress value	Allowable stress
a	Cavity: cavity/Ti-niobium joint, weld area	High RRR Niobium	20,6	33
b	Ti-Nb joint: mid section	Titanium 55% Niobium 45%	20,2	159
c	Cavity: cavity/niobium joint, weld area	High RRR Niobium	10,6	33
d	Cavity: cavity/niobium joint, weld area	High RRR Niobium	17,25	33
e	Ti-Nb joint: Ti-Nb/titanium ring, weld area	Titanium 55% Niobium 45%	34,44	99,6
f	Titanium shell: Ti shell/Ti ring joint, weld area	Titanium Grade 2	10,12	99,6
g	Titanium shell: mid section	Titanium Grade 2	8,57	99,6
h	Bellow: central convolution	Titanium Grade 2	76,4	99,6
i	Titanium shell: mid section	Titanium Grade 2	9,81	99,6
j	Cavity: iris, mid section	High RRR Niobium	11,14	33
k	Cavity: cavity/reinforcing ring joint, weld zone	High RRR Niobium	11,78	33
l	Cavity: cavity/reinforcing ring joint, weld zone	High RRR Niobium	11,24	33
m	Titanium shell: Ti shell/Ti ring joint, weld area	Titanium Grade 2	64,5	99,6
n	Ti-Nb joint: Ti-Nb/titanium ring, weld area	Titanium 55% Niobium 45%	32,9	159
o	Ti-Nb joint: mid section	Titanium 55% Niobium 45%	20,5	159
p	Cavity: cavity/Ti-niobium joint, weld area	High RRR Niobium	23,1	33
q	Cavity: cavity/niobium joint, weld area	High RRR Niobium	15,47	33
r	Cavity: cavity/niobium joint, weld area	High RRR Niobium	11,32	33
s	Titanium ring, mid section	Titanium grade 2	17,95	99,6
t	Titanium ring, mid section	Titanium grade 2	20	99,6

Table 4.13 – Membrane+bending linearized stresses for the 2nd load condition in the approaching flanges configuration and comparison with the allowable stresses

- Second load case, membrane linearized stresses with moving away flanges:

SCL	Component and evaluation region	Material	Stress value	Allowable stress
a	Cavity: cavity/Ti-niobium joint, weld area	High RRR Niobium	3,84	22
b	Ti-Nb joint: mid section	Titanium 55% Niobium 45%	5,39	106
c	Cavity: cavity/niobium joint, weld area	High RRR Niobium	3,43	22
d	Cavity: cavity/niobium joint, weld area	High RRR Niobium	12,7	22
e	Ti-Nb joint: Ti-Nb/titanium ring, weld area	Titanium 55% Niobium 45%	12,07	66,4
f	Titanium shell: Ti shell/Ti ring joint, weld area	Titanium Grade 2	3,57	66,4
g	Titanium shell: mid section	Titanium Grade 2	7,77	66,4
h	Bellow: central convolution	Titanium Grade 2	34,9	66,4
i	Titanium shell: mid section	Titanium Grade 2	9,41	66,4
j	Cavity: iris, mid section	High RRR Niobium	6,22	22
k	Cavity: cavity/reinforcing ring joint, weld zone	High RRR Niobium	11,86	22
l	Cavity: cavity/reinforcing ring joint, weld zone	High RRR Niobium	13,58	22
m	Titanium shell: Ti shell/Ti ring joint, weld area	Titanium Grade 2	19,5	66,4
n	Ti-Nb joint: Ti-Nb/titanium ring, weld area	Titanium 55% Niobium 45%	12,06	106
o	Ti-Nb joint: mid section	Titanium 55% Niobium 45%	6,09	106
p	Cavity: cavity/Ti-niobium joint, weld area	High RRR Niobium	3,67	22
q	Cavity: cavity/niobium joint, weld area	High RRR Niobium	12,74	22
r	Cavity: cavity/niobium joint, weld area	High RRR Niobium	3,85	22
s	Titanium ring, mid section	Titanium grade 2	3,81	66,4
t	Titanium ring, mid section	Titanium grade 2	2,53	66,4

Table 4.14 – Membrane linearized stresses for the 2nd load condition in the moving away flanges configuration and comparison with the allowable stresses

- Second load case, membrane + bending linearized stresses with moving away flanges

SCL	Component and evaluation region	Material	Stress value	Allowable stress
a	Cavity: cavity/Ti-niobium joint, weld area	High RRR Niobium	13,27	33
b	Ti-Nb joint: mid section	Titanium 55% Niobium 45%	13,51	159
c	Cavity: cavity/niobium joint, weld area	High RRR Niobium	5,53	33
d	Cavity: cavity/niobium joint, weld area	High RRR Niobium	30,4	33
e	Ti-Nb joint: Ti-Nb/titanium ring, weld area	Titanium 55% Niobium 45%	20,7	99,6
f	Titanium shell: Ti shell/Ti ring joint, weld area	Titanium Grade 2	5,57	99,6
g	Titanium shell: mid section	Titanium Grade 2	8,6	99,6
h	Bellow: central convolution	Titanium Grade 2	202	99,6
i	Titanium shell: mid section	Titanium Grade 2	9,81	99,6
j	Cavity: iris, mid section	High RRR Niobium	10,64	33
k	Cavity: cavity/reinforcing ring joint, weld zone	High RRR Niobium	30,9	33
l	Cavity: cavity/reinforcing ring joint, weld zone	High RRR Niobium	30,2	33
m	Titanium shell: Ti shell/Ti ring joint, weld area	Titanium Grade 2	43,8	99,6
n	Ti-Nb joint: Ti-Nb/titanium ring, weld area	Titanium 55% Niobium 45%	21,5	159
o	Ti-Nb joint: mid section	Titanium 55% Niobium 45%	15,52	159
p	Cavity: cavity/Ti-niobium joint, weld area	High RRR Niobium	15,81	33
q	Cavity: cavity/niobium joint, weld area	High RRR Niobium	29	33
r	Cavity: cavity/niobium joint, weld area	High RRR Niobium	5,13	33
s	Titanium ring, mid section	Titanium grade 2	10,28	99,6
t	Titanium ring, mid section	Titanium grade 2	12,24	99,6

Table 4.15 – Membrane+bending linearized stresses for the 2nd load condition in the approaching flanges configuration and comparison with the allowable stresses

- Third load case, membrane linearized stresses with approaching flanges:

SCL	Component and evaluation region	Material	Stress value	Allowable stress
a	Cavity: cavity/Ti-niobium joint, weld area	High RRR Niobium	12,07	22
b	Ti-Nb joint: mid section	Titanium 55% Niobium 45%	21,7	106
c	Cavity: cavity/niobium joint, weld area	High RRR Niobium	4,32	22
d	Cavity: cavity/niobium joint, weld area	High RRR Niobium	9,61	22
e	Ti-Nb joint: Ti-Nb/titanium ring, weld area	Titanium 55% Niobium 45%	6,11	66,4
f	Titanium shell: Ti shell/Ti ring joint, weld area	Titanium Grade 2	8,32	66,4
g	Titanium shell: mid section	Titanium Grade 2	8,24	66,4
h	Bellow: central convolution	Titanium Grade 2	42,3	66,4
i	Titanium shell: mid section	Titanium Grade 2	9,41	66,4
j	Cavity: iris, mid section	High RRR Niobium	7,62	22
k	Cavity: cavity/reinforcing ring joint, weld zone	High RRR Niobium	10,11	22
l	Cavity: cavity/reinforcing ring joint, weld zone	High RRR Niobium	10,03	22
m	Titanium shell: Ti shell/Ti ring joint, weld area	Titanium Grade 2	34,5	66,4
n	Ti-Nb joint: Ti-Nb/titanium ring, weld area	Titanium 55% Niobium 45%	11,4	106
o	Ti-Nb joint: mid section	Titanium 55% Niobium 45%	21,1	106
p	Cavity: cavity/Ti-niobium joint, weld area	High RRR Niobium	11,77	22
q	Cavity: cavity/niobium joint, weld area	High RRR Niobium	12,01	22
r	Cavity: cavity/niobium joint, weld area	High RRR Niobium	4,92	22
s	Titanium ring, mid section	Titanium grade 2	15,87	66,4
t	Titanium ring, mid section	Titanium grade 2	13,48	66,4

Table 4.16 – Membrane linearized stresses for the 3rd load condition in the approaching flanges configuration and comparison with the allowable stresses

- Third load case, membrane + bending linearized stresses with approaching flanges

SCL	Component and evaluation region	Material	Stress value	Allowable stress
a	Cavity: cavity/Ti-niobium joint, weld area	High RRR Niobium	30,13	66
b	Ti-Nb joint: mid section	Titanium 55% Niobium 45%	21,8	318
c	Cavity: cavity/niobium joint, weld area	High RRR Niobium	7,63	66
d	Cavity: cavity/niobium joint, weld area	High RRR Niobium	12,75	66
e	Ti-Nb joint: Ti-Nb/titanium ring, weld area	Titanium 55% Niobium 45%	22,3	200
f	Titanium shell: Ti shell/Ti ring joint, weld area	Titanium Grade 2	9,58	200
g	Titanium shell: mid section	Titanium Grade 2	8,53	200
h	Bellow: central convolution	Titanium Grade 2	109,3	200
i	Titanium shell: mid section	Titanium Grade 2	9,81	200
j	Cavity: iris, mid section	High RRR Niobium	10,65	66
k	Cavity: cavity/reinforcing ring joint, weld zone	High RRR Niobium	11,73	66
l	Cavity: cavity/reinforcing ring joint, weld zone	High RRR Niobium	12,1	66
m	Titanium shell: Ti shell/Ti ring joint, weld area	Titanium Grade 2	59	200
n	Ti-Nb joint: Ti-Nb/titanium ring, weld area	Titanium 55% Niobium 45%	30,7	318
o	Ti-Nb joint: mid section	Titanium 55% Niobium 45%	21,7	318
p	Cavity: cavity/Ti-niobium joint, weld area	High RRR Niobium	30,7	66
q	Cavity: cavity/niobium joint, weld area	High RRR Niobium	13,47	66
r	Cavity: cavity/niobium joint, weld area	High RRR Niobium	8,34	66
s	Titanium ring, mid section	Titanium grade 2	25,5	200
t	Titanium ring, mid section	Titanium grade 2	21,6	200

Table 4.17 – Membrane+bending linearized stresses for the 3rd load condition in the approaching flanges configuration and comparison with the allowable stresses

- Third load case, membrane linearized stresses with moving away flanges:

SCL	Component and evaluation region	Material	Stress value	Allowable stress
a	Cavity: cavity/Ti-niobium joint, weld area	High RRR Niobium	15,41	22
b	Ti-Nb joint: mid section	Titanium 55% Niobium 45%	22,1	106
c	Cavity: cavity/niobium joint, weld area	High RRR Niobium	2,27	22
d	Cavity: cavity/niobium joint, weld area	High RRR Niobium	10,59	22
e	Ti-Nb joint: Ti-Nb/titanium ring, weld area	Titanium 55% Niobium 45%	19,19	66,4
f	Titanium shell: Ti shell/Ti ring joint, weld area	Titanium Grade 2	3,6	66,4
g	Titanium shell: mid section	Titanium Grade 2	8,41	66,4
h	Bellow: central convolution	Titanium Grade 2	31,6	66,4
i	Titanium shell: mid section	Titanium Grade 2	9,41	66,4
j	Cavity: iris, mid section	High RRR Niobium	5,47	22
k	Cavity: cavity/reinforcing ring joint, weld zone	High RRR Niobium	15,16	22
l	Cavity: cavity/reinforcing ring joint, weld zone	High RRR Niobium	14,62	22
m	Titanium shell: Ti shell/Ti ring joint, weld area	Titanium Grade 2	14,61	66,4
n	Ti-Nb joint: Ti-Nb/titanium ring, weld area	Titanium 55% Niobium 45%	7,93	106
o	Ti-Nb joint: mid section	Titanium 55% Niobium 45%	21,5	106
p	Cavity: cavity/Ti-niobium joint, weld area	High RRR Niobium	14,84	22
q	Cavity: cavity/niobium joint, weld area	High RRR Niobium	11,7	22
r	Cavity: cavity/niobium joint, weld area	High RRR Niobium	2,55	22
s	Titanium ring, mid section	Titanium grade 2	10,56	66,4
t	Titanium ring, mid section	Titanium grade 2	6,52	66,4

Table 4.18 – Membrane linearized stresses for the 3rd load condition in the moving away flanges configuration and comparison with the allowable stresses

- Third load case, membrane + bending linearized stresses with moving away flanges

SCL	Component and evaluation region	Material	Stress value	Allowable stress
a	Cavity: cavity/Ti-niobium joint, weld area	High RRR Niobium	31,7	66
b	Ti-Nb joint: mid section	Titanium 55% Niobium 45%	23,5	318
c	Cavity: cavity/niobium joint, weld area	High RRR Niobium	3,52	66
d	Cavity: cavity/niobium joint, weld area	High RRR Niobium	28,1	66
e	Ti-Nb joint: Ti-Nb/titanium ring, weld area	Titanium 55% Niobium 45%	24,2	200
f	Titanium shell: Ti shell/Ti ring joint, weld area	Titanium Grade 2	5,37	200
g	Titanium shell: mid section	Titanium Grade 2	8,74	200
h	Bellow: central convolution	Titanium Grade 2	258	200
i	Titanium shell: mid section	Titanium Grade 2	9,81	200
j	Cavity: iris, mid section	High RRR Niobium	10,63	66
k	Cavity: cavity/reinforcing ring joint, weld zone	High RRR Niobium	37,6	66
l	Cavity: cavity/reinforcing ring joint, weld zone	High RRR Niobium	38,2	66
m	Titanium shell: Ti shell/Ti ring joint, weld area	Titanium Grade 2	26,7	200
n	Ti-Nb joint: Ti-Nb/titanium ring, weld area	Titanium 55% Niobium 45%	24,7	318
o	Ti-Nb joint: mid section	Titanium 55% Niobium 45%	23	318
p	Cavity: cavity/Ti-niobium joint, weld area	High RRR Niobium	31,5	66
q	Cavity: cavity/niobium joint, weld area	High RRR Niobium	26,3	66
r	Cavity: cavity/niobium joint, weld area	High RRR Niobium	2,99	66
s	Titanium ring, mid section	Titanium grade 2	15,03	200
t	Titanium ring, mid section	Titanium grade 2	10,17	200

Table 4.19 – Membrane+bending linearized stresses for the 3rd load condition in the moving away flanges configuration and comparison with the allowable stresses

As it can be easily seen, the linearized stresses are lower than the material's allowable stresses only inside the bellow elements: in order to verify them the introduction of the ASME Div. I procedure is very useful and more realistic than the Div. II. Since the bellow is a very simple component that can be analyzed with analytical formula, the way the stresses for the bellow elements have been evaluated is using the Ameriflex, Inc., (the bellows vendor) design calculations summary, an electronic sheet dated 4/10/2008 based on these analytical formula This electronic sheet is inserted below.

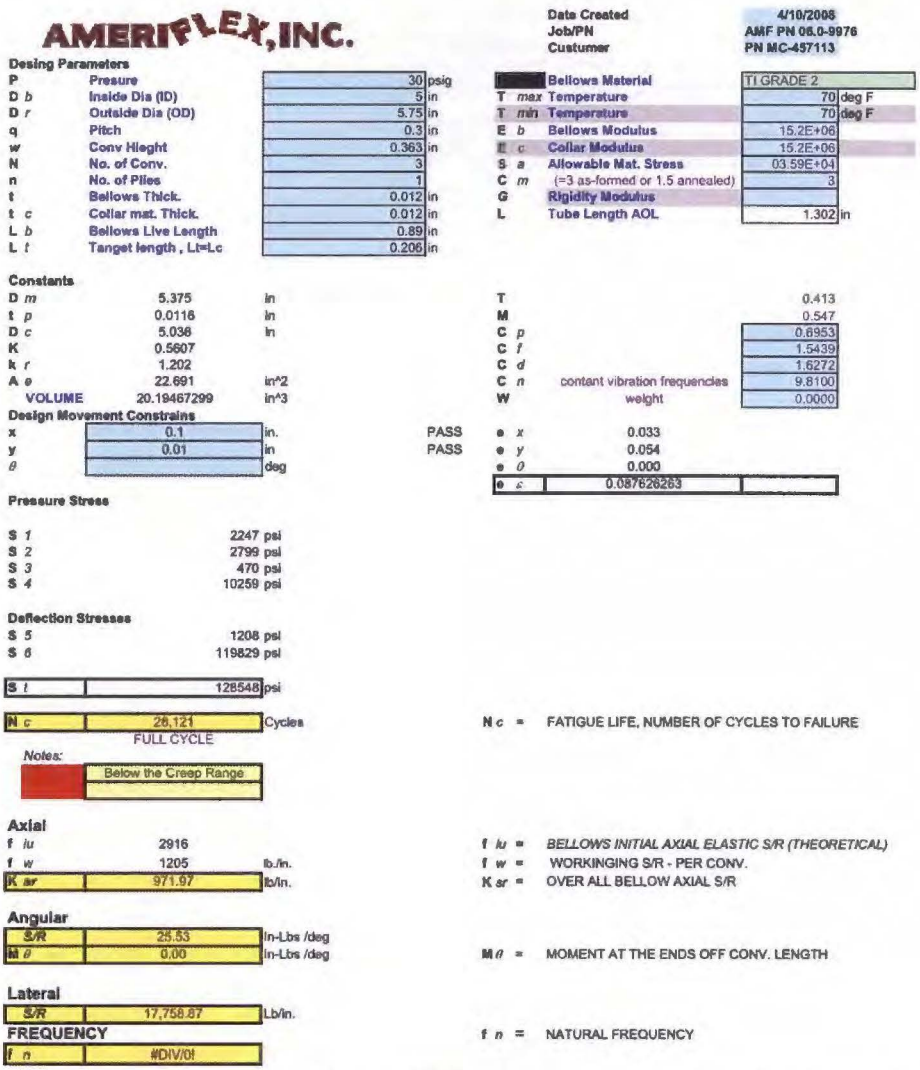

AMERIFLEX, INC.

Date Created 4/10/2008
Job/PN AMF PN 06.0-9976
Custumer PN MC-457113

Desing Parameters

P	Presure	30	psig		Bellows Material	TI GRADE 2	
D b	Inside Dia (ID)	5	in	T max	Temperature	70	deg F
D r	Outside Dia (OD)	5.75	in	T min	Temperature	70	deg F
q	Pitch	0.3	in	E b	Bellows Modulus	15.2E+06	
w	Conv Hieght	0.363	in	E c	Collar Modulus	15.2E+06	
N	No. of Conv.	3		S a	Allowable Mat. Stress	03.59E+04	
n	No. of Plies	1		C m	(=3 as-formed or 1.5 annealed)	3	
t	Bellows Thick.	0.012	in	G	Rigidity Modulus		
t c	Collar mat. Thick.	0.012	in	L	Tube Length AOL	1.302	in
L b	Bellows Live Length	0.89	in				
L t	Tanget length , Lt=Lc	0.206	in				

Constants

D m	5.375	in	T			0.413
t p	0.0116	in	M			0.547
D c	5.036	in	C p			0.8953
K	0.5607		C f			1.5439
k r	1.202		C d			1.6272
A e	22.691	in^2	C n	contant vibration frequencies		9.8100
VOLUME	20.19467299	in^3	W	weight		0.0000

Design Movement Constrains

x	0.1	in.	PASS	e x	0.033
y	0.01	in	PASS	e y	0.054
θ		deg		e θ	0.000
				e ε	0.087626263

Pressure Stress

S 1	2247 psi
S 2	2799 psi
S 3	470 psi
S 4	10259 psi

Deflection Stresses

S 5	1208 psi
S 6	119829 psi

S t	128548	psi
N c	26,121 FULL CYCLE	Cycles

N c = FATIGUE LIFE, NUMBER OF CYCLES TO FAILURE

Notes:

Below the Creep Range

Axial

f iu	2916		f iu = BELLOWS INITIAL AXIAL ELASTIC S/R (THEORETICAL)
f w	1205	lb./in.	f w = WORKINGING S/R - PER CONV.
K ar	971.97	lb/in.	K ar = OVER ALL BELLOW AXIAL S/R

Angular

S/R	25.53	In-Lbs /deg
M θ	0.00	In-Lbs /deg

M θ = MOMENT AT THE ENDS OFF CONV. LENGTH

Lateral

S/R	17,758.87	Lb/in.

FREQUENCY

f n	#DIV/0!

f n = NATURAL FREQUENCY

Fig. 4.13 – Bellow stress analysis performed accordingly with the ASME Sec. VIII Div I

The advantage of using the Div. I instead of the Div. II of the Section VIII of the ASME Code is that the allowable stresses of the materials are higher because all the resulting stresses are determined by analytical formula, so they can be calculated with a higher accuracy.
The resulting stresses using this electronic sheet for the bellow are summarized in the table below.

Type of stress	Stress (MPa)	Allowable (MPa)
Circumferential membrane in bellows tangent	33.6	144
Circumferential membrane for end convolution	59.5	144
Circumferential membrane for intermediate convolution	47.3	144
Meridional membrane + bending in bellows	125	432

Table 4.20 – Results for the bellow analysis accordingly with the Div. I and comparison with the allowable stresses

4.4 – Buckling analysis of the cavity

Accordingly with the ASME Div. II Sec. VIII code the cavity has to be analyzed in order to find its buckling behavior and its critical pressure. This analysis needs to be performed in a nonlinear regimen so the material's and problem's nonlinear effects are included and allows to give more conservative results.
The cavity has been separately studied from the rest of the structure and blocked in the surfaces where it's linked with the niobium collars.

Fig. 4.14 – 3d FEA model of the cavity used for the nonlinear buckling analysis

Accordingly with the ASME code a bilinear kinematic hardening model, with a yielding point which has the same value than the material's allowable stress and with a plastic modulus which is 10 times lower than the Young modulus was used: this choice is due to conservative concerns, because the stress-strain curve resulting from linearized experimental data always is higher than the ASME resulting one, as it is shown on Fig. 4.15.

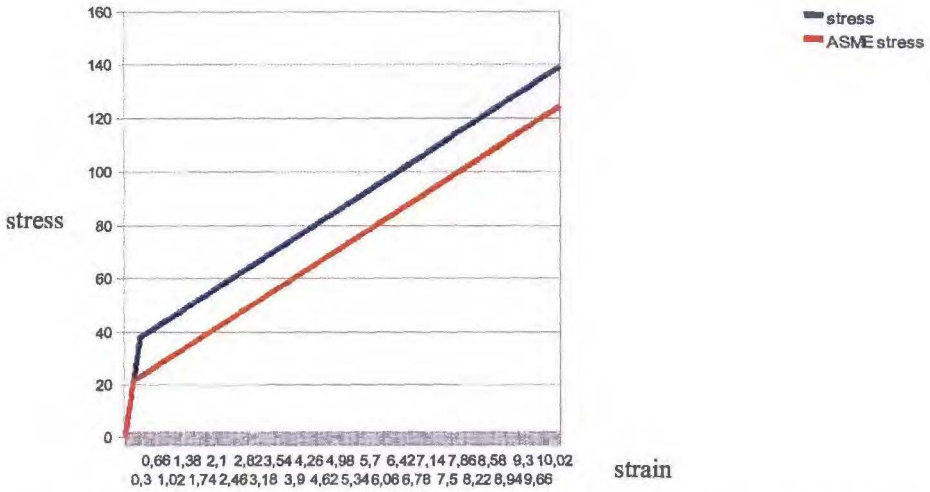

Fig. 4.15 – Comparison between the approximated stress rate (blue line) and rate given by ASME (red line)

During the simulation the cavity has been loaded with a pressure whose value vary from 1bar up to the plastic collapse pressure of the cavity, where the computer stops the iterations because a converged solution can't exist anymore. In order to evaluate the plastic behavior of the cavity when it bears the external pressure a multi-step static analysis has been performed, where in every load step the external pressure is 0.5 bar higher than the value in the previous load step: so in every load step the static analysis is performed and the cavity's new configuration is kept into the calculator's memory and used for the next load step.

In the picture below the deformation – pressure curve is displayed.

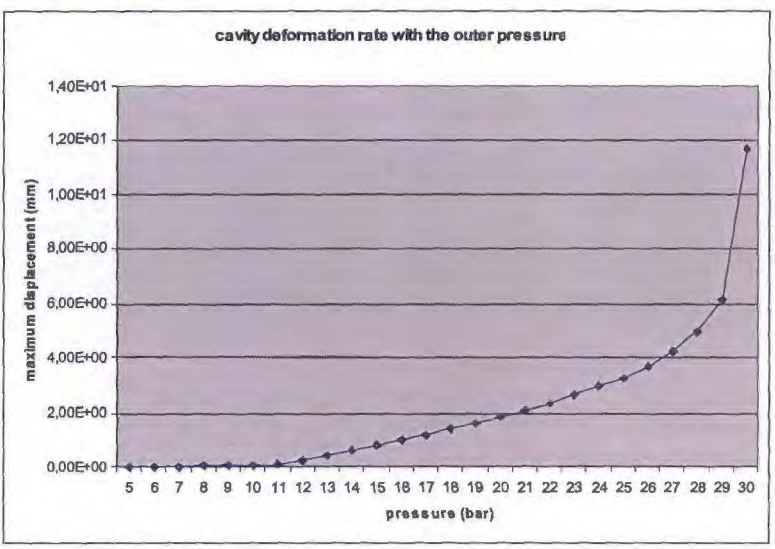

Fig. 4.16 – Curve of the results of the buckling analysis: on the x axis the value of the load is indicated, while on the y axis the calculated displacement is given

Two considerations need to be done about the curve shown above: the first change in the curve's slope is due to the niobium's yielding. In this first point (whose pressure value is about 10bar, higher that the operative value of the pressure) the material's behavior is nomore linear but the cavity itself can bear a higher pressure because it is mostly still in elastic conditions.

The second change in the curve's slope is due to the collapse effect (which appears at 30bar, more than 7 times higher than the operative load): this is the ultimate load condition for the cavity.

In the picture below the deformed shape of the collapsed cavity is shown.

Fig. 4.17 – Deformed shape of the buckled cavity

The picture shows that the collapse effects are local in the cavity and the zone where the collapse appears, very close to the reinforcing rings, shows their utility.

4.5 – Conclusion

This chapter has shown that it is possible to certify the 1.3 GHz Helium vessel accordingly with the ASME Code: this is an important final step of the whole design process and it allows to let the manufacturing of all the He vessel/cavity assembly's components start.

Moreover, as shown on the paragraphs above, the procedure used to study the whole assembly allows to reduce the computational times but it also provides to introduce a very fine mesh and second-order elements. The consequence of this choice is that the results are very accurate.

5. STUDY OF THE 1.3 GHZ CAVITY'S END-CAP MANUFACTURING

5.1 – Introduction and description of the manufacturing procedure

The advantage of using the titanium-niobium end-cap consists in the fact that it can be welded with either the titanium or the niobium in order to create a reliable joint with an EBM operation.
The manufacturing process of it consists of these steps:

- Plastic moulding: before being plastically deformed the end-cap is a flat hollow disk, ready to be inserted into the moulding machine. After this operation a conical part is created under the action of the aluminium dies: it's very important to control the axis-symmetry of this operation, in order not to obtain a final end-cap with slop angles that vary along the circumference. At the end of this operation strict tolerances need to be respected, so the spring-back phenomenon has to be wholly studied during the design of the dies in order to obtain the correct final slop angle.
- Mechanical machining: the end-cap's ends are machined in order to prepare them to be welded with the titanium ring and the niobium collar. Besides the plastic-moulded cone's external surfaces are finished off, so that the final quality of the end-cap is maximized and the thickness and the slop angle tolerances are respected
- Annealing process: a thermal process is performed on the end-cap before it is ready to be assembled with the cavity and the Helium vessel.

During the tests for the realization of the end-cap several problems arose: the first one concerns with the nominal value of the slope angle, while the second concerns with the slope angle variation. When the process was performed for the first time the slope angle was several degrees higher than than the nominal value (so the cone was flatter than what it should be): in order to fix this problem the dies were re-designed with the support of a finite element analysis, that is a very useful device able to simulate the whole phenomenon and the spring-back effect.
The second problem can be fixed by improving the accuracy in the relative position between the two dies, or by performing a two-step deformation process, where between the two phases of the process the conical end-cap is rotated around his axis by 90° so that the slope errors are reduced.
In this chapter the whole finite element analysis of the moulding process is described.
Before starting to describe the finite element model the end-cap's final draft together with the drafts of the dies are shown in the next pages.

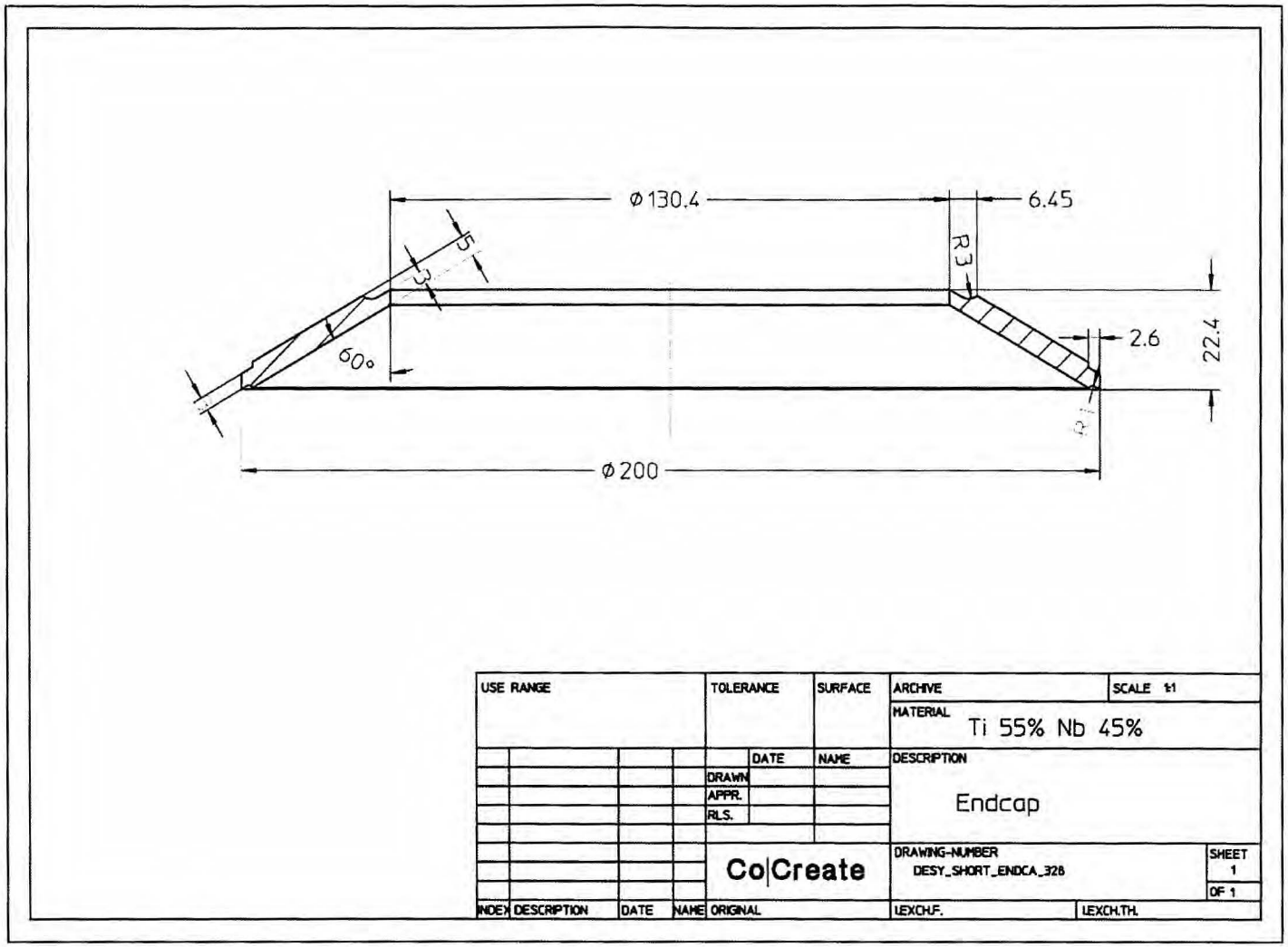

Fig. 5.1 – 2d draft of the final shape of the titanium-niubium end-cap

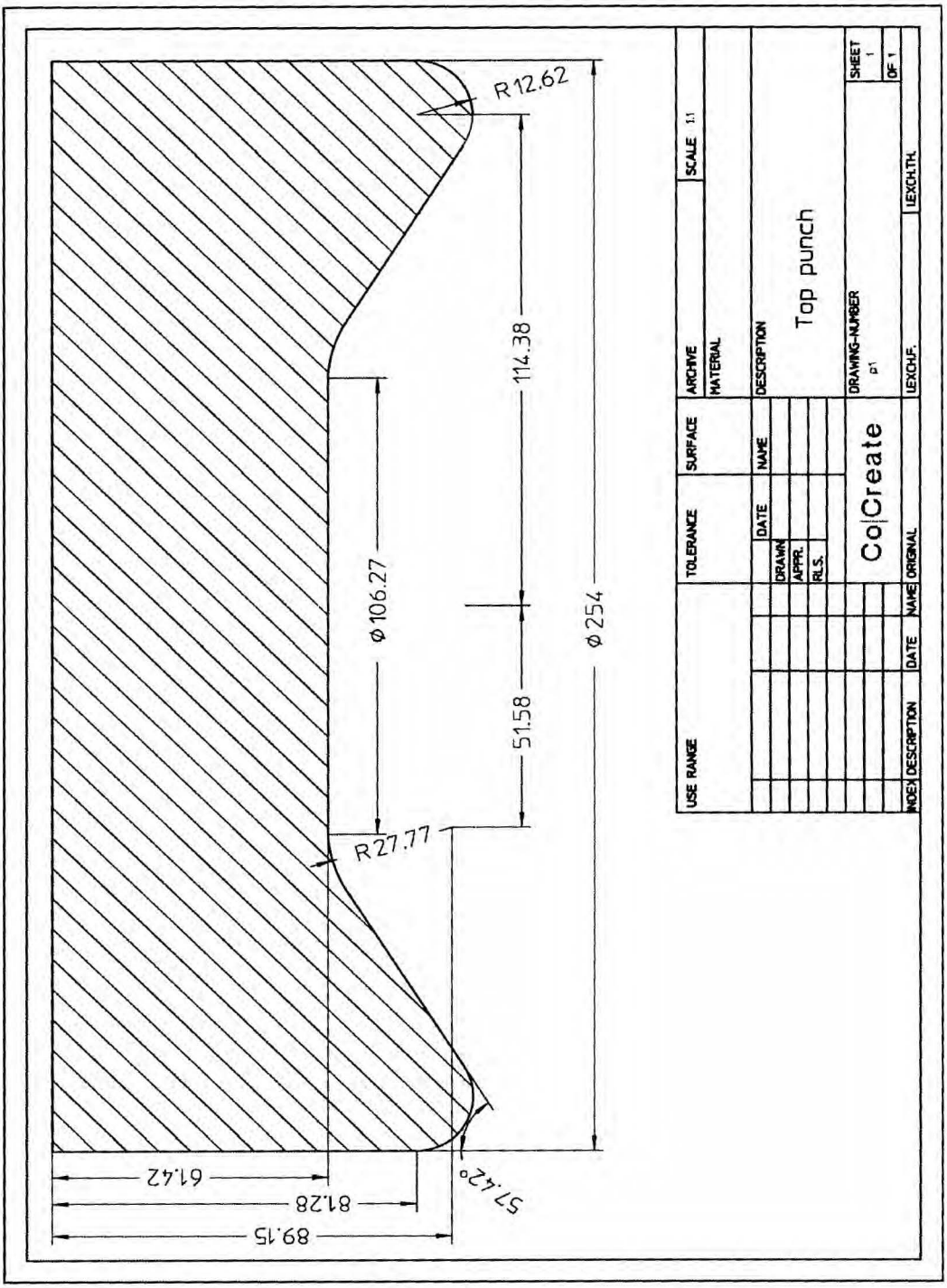

Fig. 5.2 – 2d draft of the final shape of the aluminum upper die

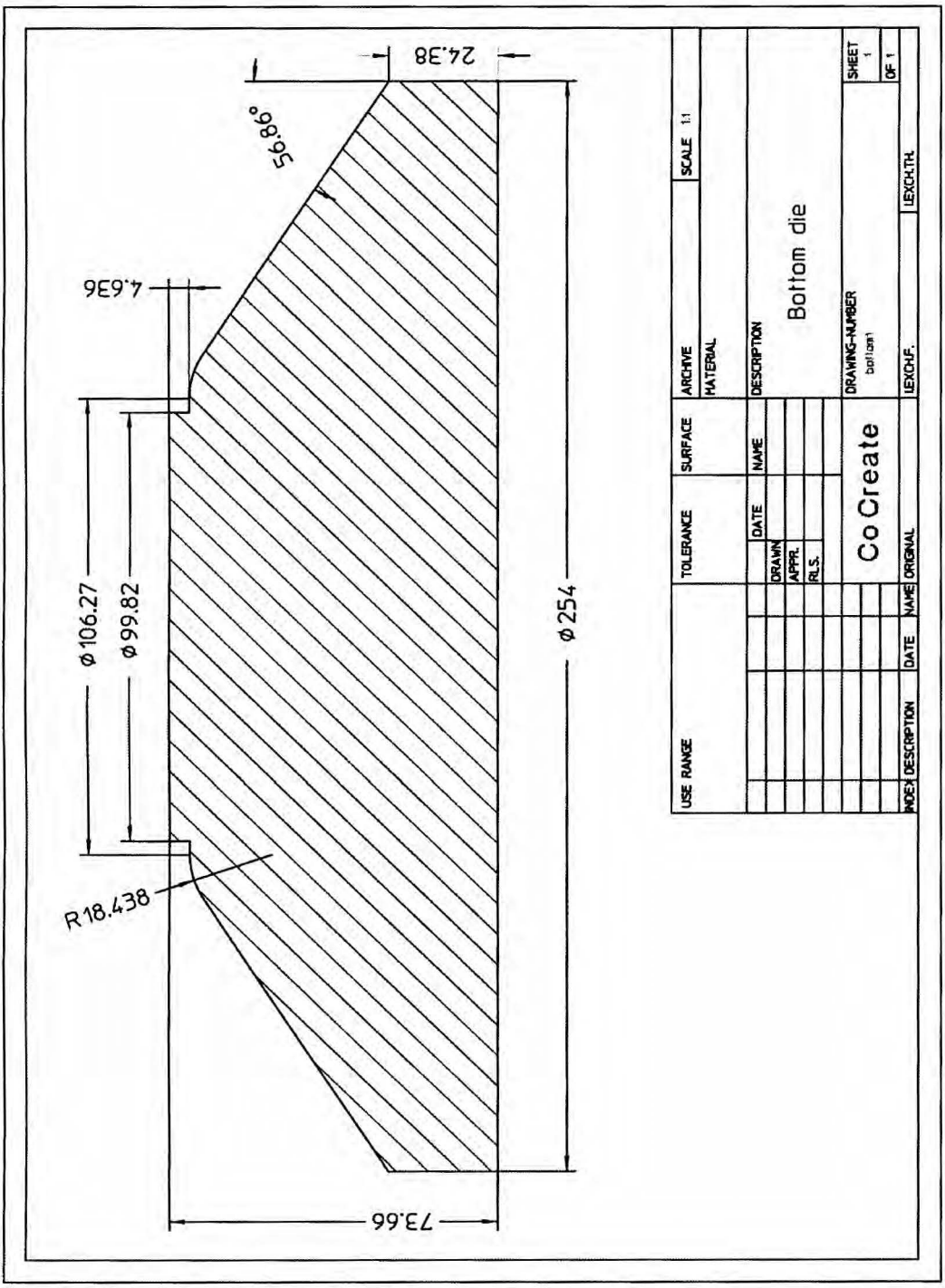

Fig. 5.3 – 2d draft of the final shape of the aluminum lower die

5.2 – FEA Model description

In order to study in a proficient and simple way the whole plastic deformation process a 2-d axis-symmetric model has been introduced: obviously some non-axis-symmetric effects such as the incorrect relative position between the two dies are not considered into the model. Besides the use of a 2-d analysis allows to use quadratic elements, who give more accurate results. The 2d model used for the analysis is shown in the picture below.

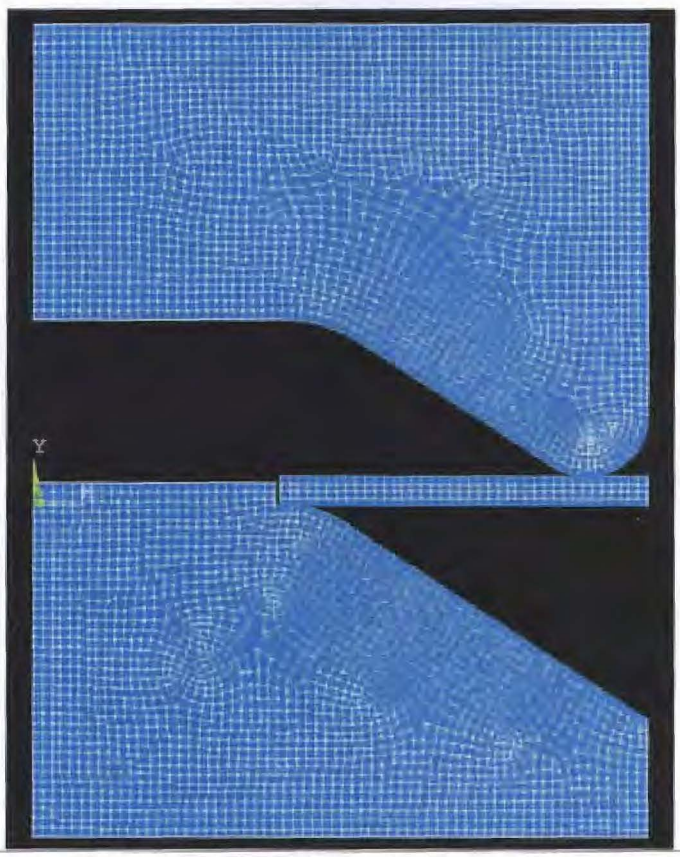

Fig. 5.4 – FEA model used for the analysis of the manufacturing process

It's very important, in order to obtain realistic results by performing the analysis, to represent the titanium-niobium's stress-strain curve with a simple but realistic curve: because of this goal a bilinear plastic behavior who answers to a kinematic hardening criterion has been used for the end-cap's material.
The comparison between the real stress-strain curve (furnished by the vendor) and the simplified curve is shown in the picture below.

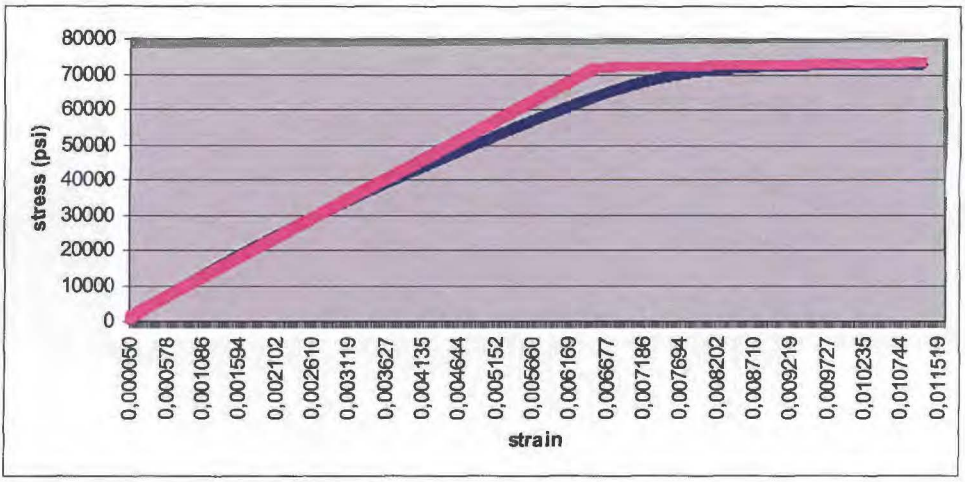

Fig. 5.5 – Comparison between the titanium-niobium's real stress-strain curve (blue line) and the approximated one (pink line)

The material data are listed below:

$E = 1100000\text{psi} = 7.70\text{GPa}$

$\sigma_{ys} = 71710\text{psi} = 502\text{MPa}$

$E_p = E/10 = 770\text{MPa}$

$\nu = 0.33$

In order to correctly represent the plastic process it is important to take care about:

- the contact between the dies and the disk;
- the friction between all the parts in contact;

The first phenomenon has been considered by introducing the contact elements: all the surfaces that are supposed to be in contact are filled with node-to-surface contact and target elements, so that a unilateral contact type is set. In the initial condition there is an initial contact between two nodes only on both the upper and the lower contact pair, as it is shown in the figure below.

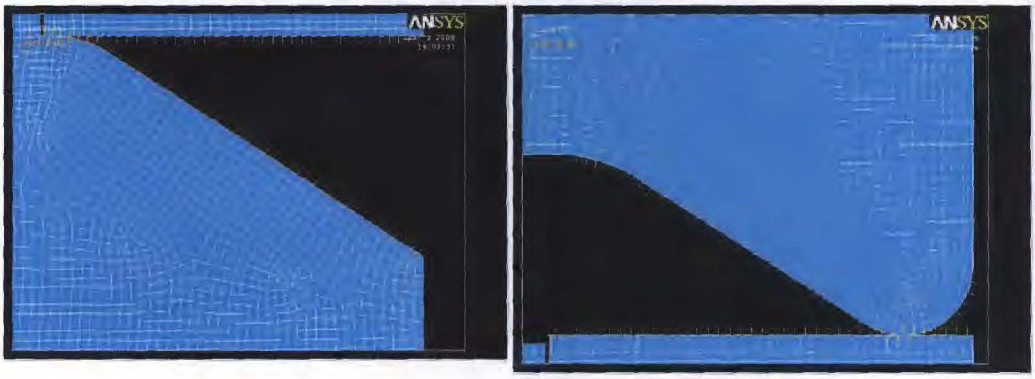

Fig. 5.6 – Contact zone representation

The flat disk is inserted into the bottom die's central hole and during the deformation process it's free to radially deform itself, so that it can move along the bottom die's inclined surface. Because of this fact it is important to represent the friction between the flat disk and the surfaces in contact: accordingly to the Roymech's library a 1.0 friction coefficient has been taken for the titanium-niobium/aluminium contact pairs.
The analysis has been performed under a multi-step regimen: in the first step the upper die vertically moves up to the final position; in the second load step the upper die moves back up to the starting position and a very low pressure is applied on the disk: the pressure has been introduced on the disk's upper surface in order to avoid calculus problems for the computer due to the unconstrained disk and not to give further plastic deformations to the disk; in the third and final load step the low pressure is removed.

5.3 – Results

In the pictures below the Von Mises stress map is shown for the middle part of the first step, for the end of the first load step and for the end of the whole deformation process.

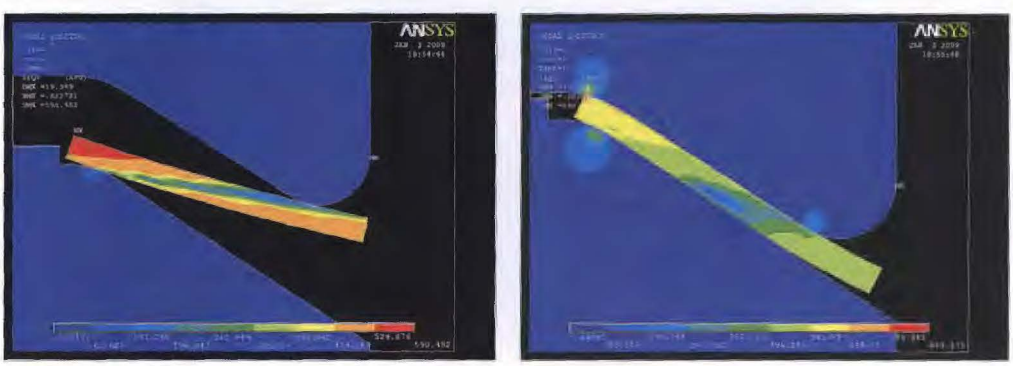

Fig. 5.7 – Von Mises stress maps in the condition of 16mm (on the left) and 32mm (the final value, on the right) upper die's vertical displacement

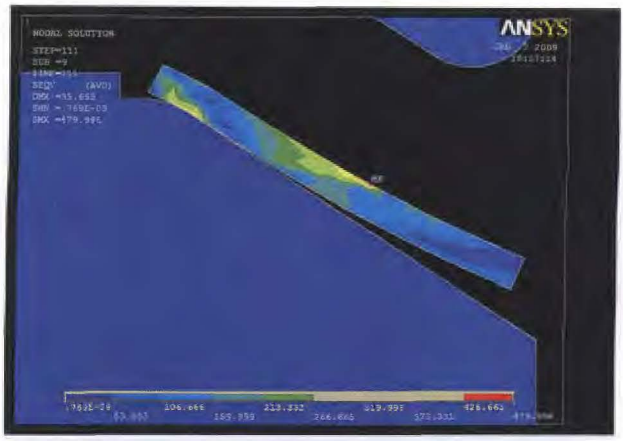

Fig. 5.8 – Von Mises stress map and deformed shape of the end-cap after the end of the deformation process (the elastic spring-back is shown)

As it can be seen on the last picture shown above, the elastic spring-back shows that the titanium-niobium end-cap's final shape is no conical, so that the slope angle gets lower the higher is the radius coordinate. This effect is shown on a sample performed on the Fermilab's Technical Division. In the graph below the FEA model's slope angle rate is shown as function of the radial coordinate.

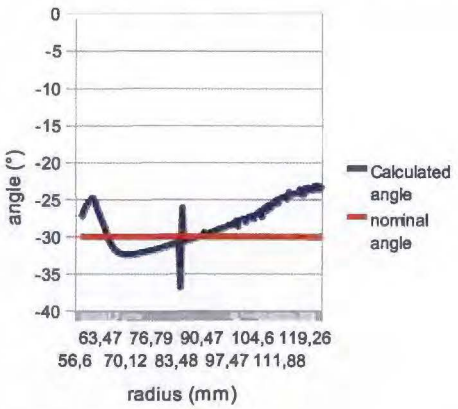

Fig. 5.9 – FEA model's slope angle rate represented as a function of the radial coordinate of the end-cap

The slope angle rate curve clearly shows that the end-cap's final shape is not conical: in order to avoid this problem a new design of the dies is required. In fact the dies mustn't have flat inclined surfaces but they must have a parabolic rate, so that the elastic spring-back effect will create a cone. Moreover in order to compare the finite elements analysis results with the empiric results the thickness rate has been studied: experiments showed that the thickness gets lower the higher is the radius coordinate. This thickness rate is shown in the picture 5.10.

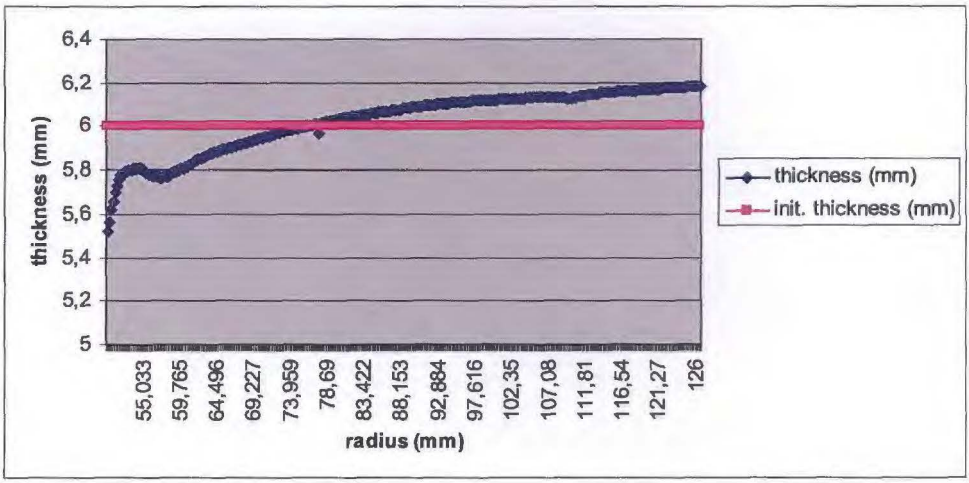

Fig. 5.10 – FEA model's thickness represented as a function of the radial coordinate of the end-cap

The plot above shows that the empiric results are conform with the simulation results.

5.4 – Improvement of the final shape of the end-cap

In order to eliminate the defect in the final shape of the end-cap, a proposal for a new lower die profile has been presented with a parabolic profile (shown on Fig. 5.11): two different curves (one with the y=x^-1.7 profile and the other with the y=x^1.5 one) were merged with the goal of creating this new lower die's profile.

Fig. 5.11 – FEA model for the improvement of the end-cap's final shape

The end-cap's profile obtained after introducing the new lower die is very similar to the nominal one (shown on Fig. 5.1) because the slope angle rate has very low variations along the radius

coordinate (see Fig. 5.12 and 5.13).

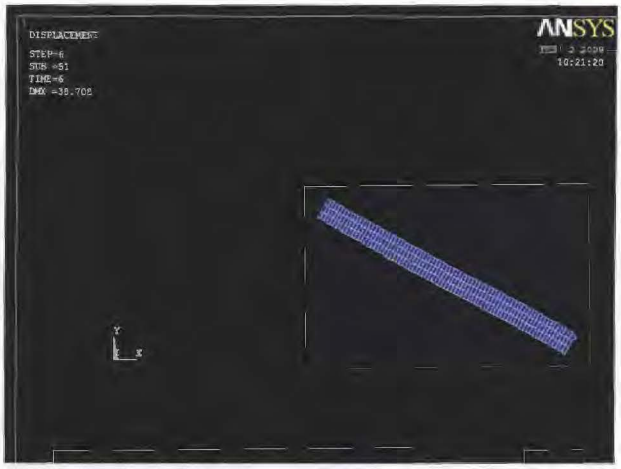

Fig. 5.12 – Deformed shape of the end-cap manufactured with the improved bottom die

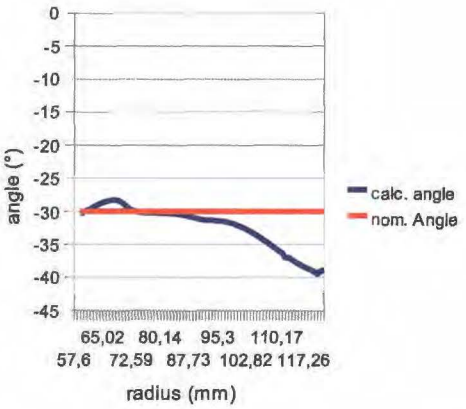

Fig. 5.13 – FEA model's slope angle rate for the end-cap manufactured with the improved lower die represented as a function of the radial coordinate of the end-cap

The slope angle of the deformed end-cap is about 30° for a huge radial zone from 63mm up to 105mm, while the end-cap's inner and outer radii are equal to the nominal values, 65mm and 100mm.

5.5 – Conclusions

The purpose of this chapter was the study the manufacturing process of the end-cap and the

investigation about the defects that were found on some experimental evidences: after the simulation of the whole process, the origin of these defects was found.
Moreover a new configuration of the lower die was proposed: it implicates a more complex shape of the die (in fact it's necessary to perform a Numeric Control Tool Operation in order to manufacture such a profile) but it allows a better conformity of the geometric parameters of the deformed piece to the nominal one.

6. ANALYSIS AND OPTIMIZATION OF THE 1.3 GHZ HE VESSEL'S EFFICIENCY

The analysis for the assessment of the efficiency of the 1.3GHz Helium vessel (He vessel) is very important in order to determine the displacement that must be given to the vessel's flanges by the blade-tuner's action when the cavity must be stretched by a certain amount. Moreover with this analysis it is possible to detect where the source for the loss of efficiency is located, so that a remedy for increasing this parameter can be found.
Another analysis that will be shown in this chapter is the analysis for the assessment of the vessel's stiffness, so that it is possible to determine the force that the blade-tuner bust act on the flanges in order to stretch the cavity by a certain amount. This analysis is very useful in order to study the blade-tuner's resistance , because it allows to study the blade-tuner by itself and to represent the whole vessel as a spring applied on the flanges' holes where the vessels is linked with the blade-tuner
Before describing the analyses introduced above, it is useful to clearly define the vessel's efficiency parameter (η): this is the ratio between the cavity ends' relative axial displacement and the flanges' relative axial displacement given by the blade-tuner.

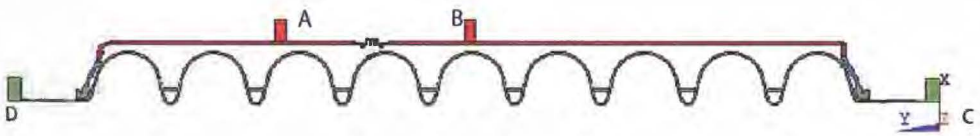

Fig. 6.1 – 2d draft of the FEA model used for the efficiency analysis

$$\eta = \frac{u_y(D) - u_y(C)}{u_y(A) - u_y(B)}$$

Another efficiency parameter that won't be considered in this chapter is the flanges' efficiency, defined as the ratio between the extension of the bellow and and the relative axial displacement of the flanges.

6.1 – 2d FEA model efficiency analysis

In order to obtain an approximated assessment of the He vessel's efficiency a 2d FEM analysis has been performed: the same model introduced for the resistance analysis (see paragraph 4.3) has been used and the only difference with it is that the elements are no-more harmonic, but simple axis-symmetric. The vessel has been blocked on the flange indicated with the letter B in the Fig. 6.1, while the flange indicated with A has been moved away from the other one with a 1mm displacement.
The relative displacement between the niobium cavity's ends due to this load condition has been taken in account in order to determine the vessel's efficiency. The results are shown in the Fig. 6.2.

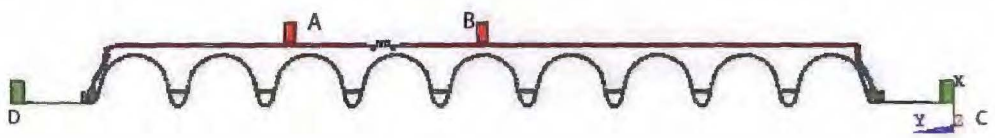

A: Locked surface by the flanges holes
B: Shifted suface by the piezo holes
C,D:Cavity ends

2d analysis: $\delta b=0.5$
$\delta c=0.483$
$\delta d=0.0168$

$\eta=93.3\%$

Fig. 6.2 – Results of the 2d FEA analysis for the assessment of the efficiency

The difference between this model and the real one lies on the blade-tuner flanges' representation and on the way the displacement is applied. In this 2d axis-symmetric model they are represented as two flat disks with a constant thickness either along the circumferential and radial coordinates and this condition is far from the reality, because, as it will be seen below, the flanges present some features that do make it not axis-symmetric and more compliant than it is in this 2d FEM analysis. However, with this analysis it is possible to investigate on the vessel's components considered by their own in order to look at which components is responsible for this loss of efficiency.
The weakest component of the whole Helium vessel assembly is the titanium-niobium end-caps because in these structures the axial movement is transferred from the blade-tuner flanges to the cavity through its bending, taking in account also the low Young modulus (2 times lower than the titanium's and niobium's) of its material.
The following analyses have been performed in order to understand the nature of this phenomenon:

- analysis of the vessel without the cavity's reinforcing rings: these vessel's components have been introduced in order to increase the cavity's resistance to the operating pressure and the buckling resistance, but even increase the cavity's stiffness so that the vessel's efficiency is reduced

	Cavity with rings	Cavity without rings
Value of efficiency (η)	0,93	0,98

- analysis of the efficiency rate as a function of the end-cap's value of the Young's Modulus. In the picture 6.3 this rate is shown (on the x axis the Young Modulus is divided by the

titanium-niobium's value)

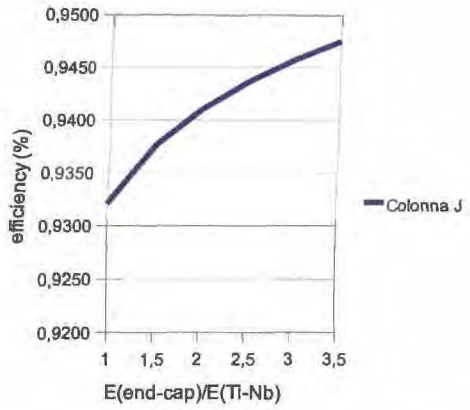

Fig. 6.3 – Efficiency rate for the He vessel as a function of the end-cap's Young modulus

Another useful study of the vessel is the analysis of the limit of its linear behavior: in fact the bellow has a linear behavior until a certain amount of the flanges' axial displacement, and this value must be higher than the nominal one. In order to achieve this result a multi-step analysis with the large displacement nonlinearity solving option turned on has been performed: in every load step a 1mm displacement has been added on the flange indicated as B on the figure 6.3.
The efficiency rate as function of the master displacement of the flanges is shown in the picture 6.4: this value doesn't substantially change even when the flanges' displacement is higher than 20mm (40 times higher than the operative conditions).

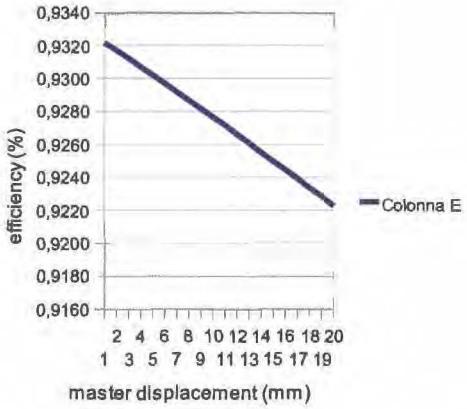

Fig. 6.4 – Efficiency rate of the He vessel as a function of the flanges' relative displacement

6.2 – 3d FEA model efficiency analysis

The 3d model analysis allows to take in account the fact that the flanges are not axis-symmetric components and that the displacement is not uniformly applied on the flange but only on some points. The vessel's configuration for the efficiency analysis is shown below.

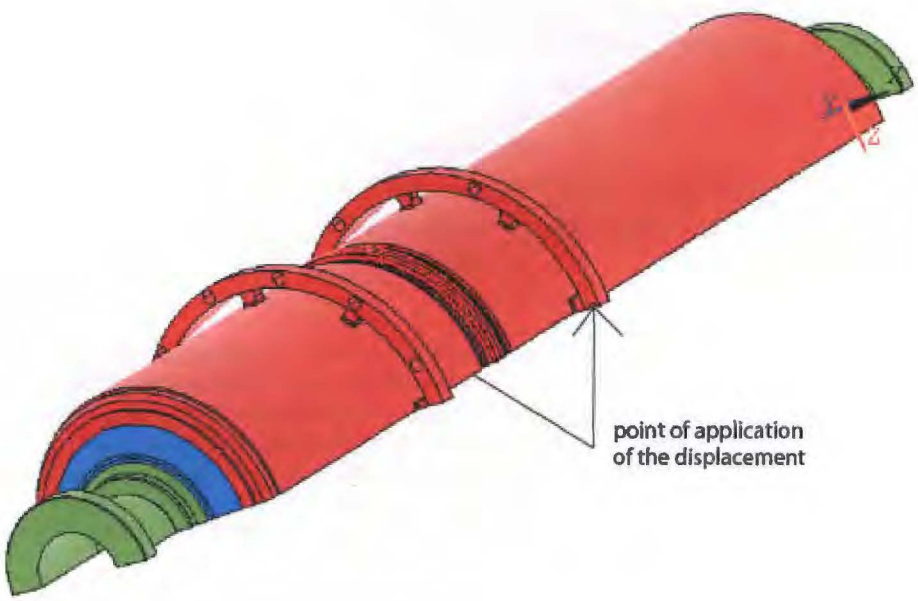

Fig. 6.5 – 3d FEA model used for the efficiency 3d analysis

A 1 mm displacement has been applied on the holes represented in the figure above (one of these is covered by the figure), which are the points linked with the blade-tuner's piezos. The other flange has been blocked by its holes and a symmetry boundary condition has been introduced to minimize the computational times.

The results are listed below.

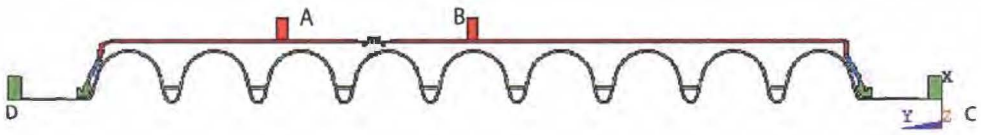

A: Locked surface by the flanges holes
B: Shifted suface by the piezo holes
C,D:Cavity ends

3d analysis:	δb=0.5 δc=0.441 δd=0.0261	η=83%	2d analysis:	δb=0.5 δc=0.483 δd=0.0168	η=93.3%

Lost efficiency=89%

Fig. 6.6 – Results if the 3d efficiency analysis

The loss of efficiency of this model compared to the 2d one is due to two phenomenon:

- the master displacements are not axis-symmetric but they are applied in 2 points, so the flanges can circumferentially bend;
- the flanges are linked to the vessel in a few points instead of an axisymmetric way, so flanges can more easily bend

In order to regain some efficiency increasing the number of connections with the vessel or thickening the flanges would be the best remedies. In order to evaluate the benefits that occur by these two remedies two parametric analysis has been performed.
In the first analysis a model with the thickened flanges has been studied.

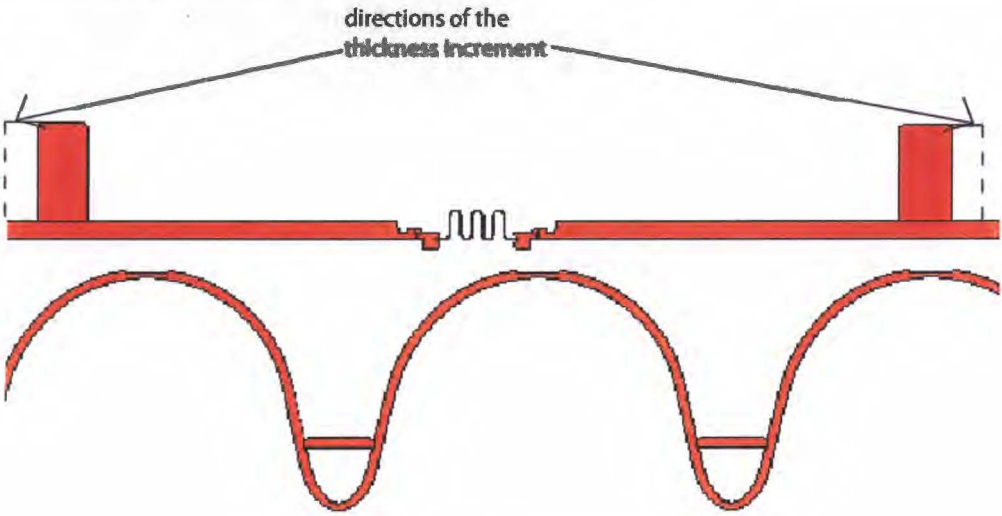

Fig. 6.7 – Description of the first optimization attempt

A 3 steps flanges thickening has been performed: in the first step a 15mm thickness (the original value) has been used, while in the steps 2 and 3 a 18 and 24 thickness has been used. The results are shown below in figure 6.8.

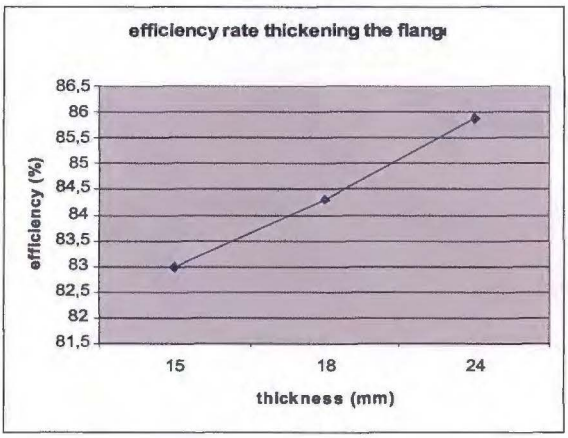

Fig. 6.8 – Results of the first optimization attempt

In the second analysis a model with the widened flanges has been studied.

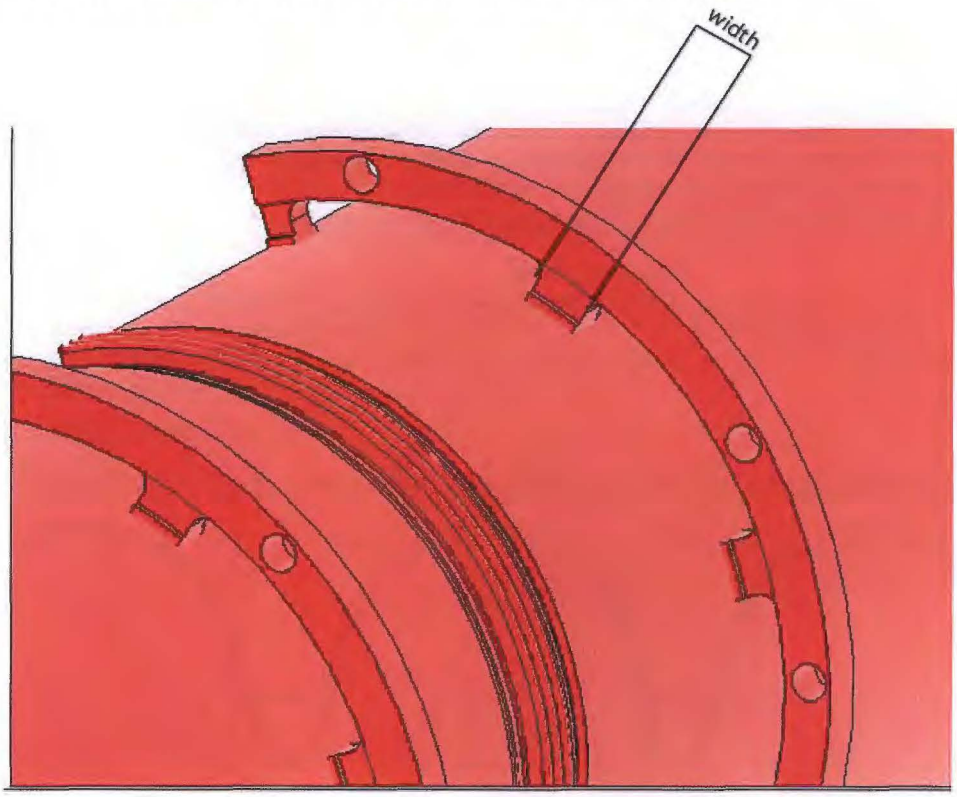

Fig. 6.9 – Second optimization attempt

A 3 steps flanges' linking widening has been performed: since there isn't a uniform linking's wideness all the values have been increased by the 0% in the first step (to obtain the original model), and by the 20% and 44% in the second and third steps. The results are shown below.

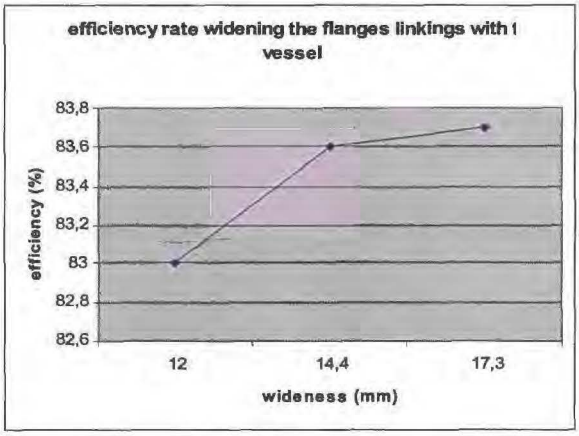

Fig. 6.10 – Results of the second optimization attempt

The result of the optimization operation (figures above) is that thickening the flanges gives better results than widening the linking between flanges and vessel.

Finally the 3d model has been used to assess the vessel's stiffness in the points where it is linked to the blade-tuner, which is the value of the reaction force that the vessel develops when a flange is displaced by 1m. In order to obtain all the values of the stiffness it's necessary to study one model for every hole linked with the blade-tuner. This value is very useful to study the blade-tuner like described in the chapter 7.

Moreover in order to obtain the correct value of the stiffness it is necessary to assess the stiffness shifting a flange's hole by the nominal value of the displacement blocking the other flange, so that the stress stiffening effects, are not considered; this effect, as it can be seen on Fig. 6.4, strongly influences the vessel only for displacements larger than 10 mm.

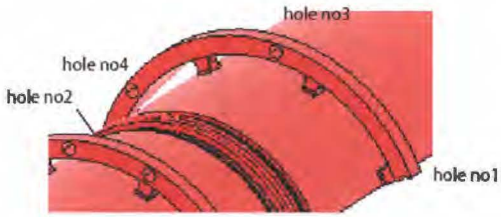

No of hole	Value of the vessel's reaction force (N)	Value of the stiffness (N/mm)
1, 2	976	3900
3,4	750	3000

Fig. 6.11 – Assessment of the vessel's stiffness calculated in the points were the blade-tuner is linked

6.3 – Conclusions

The Chapter 6 showed all the analyses performed to assess the efficiency of the Helium vessel. They are very important because they allow to assess the stretching of the cavity as a function of the relative displacement of the flanges. This aspect is fundamental for the design of the tuning system (that will be better described in the next chapter) because it allow to assess the effective flange's displacement that the tuning system must ensure in order to correctly compensate the LFD. Moreover later on this chapter the efficiency was studied as a function of the most important geometric and physical properties of the He vessel, so that an optimization of this parameter was been possible.
The Fermilab, after the results described on this chapter were issued, took them into account by considering a thickening of the flanges in order to increase the vessel's efficiency.

7. STUDY OF THE BLADE-TUNER

7.1 – Introduction and description of the blade-tuner

The blade-tuner has been introduced in order to compensate the effect of the Lorentz's axial force. The way this component works is explained below.
Under the normal load condition the huge electric field inside the cavity (in the order of 35MV/m) causes the shrinkage of the cavity and of the whole He vessel connected to it; this shortening is perceived by the sensitive elements who link the He vessel's flanges with the central part of the blade-tuner.
On a first approach this tuner has been designed to be coaxial with the cavity and, by means of elongation of the helium vessel, to deform the cavity geometry and consequently change its own resonance frequency. The tuner assembly is mainly composed of two parts, the movement leverage and the bending rings. The complete assembly of the tuner as mounted over the He vessel is shown in the figure 7.1.

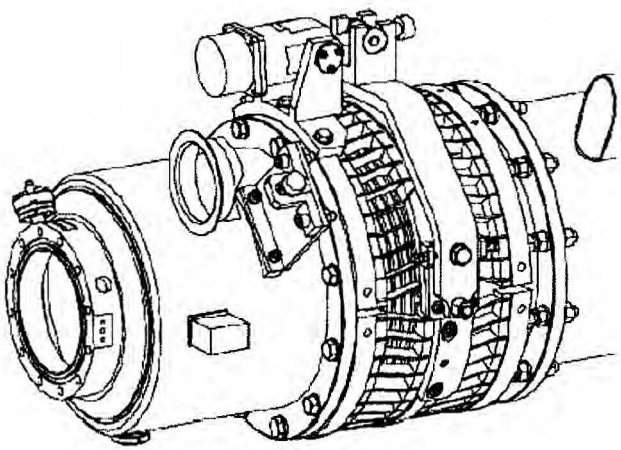

Fig. 7.1 – 3d draft of the blade-tuner mounted on the He vessel

The leverage system provides the amplification of the torque of the stepper motor, dramatically reducing the total movement and increasing the tuning sensitivity. The stepping motor, is rigidly connected to the He vessel and produces a rotation of the big arm in the center of the tuner. The

movement of the big arm induces the rotation of the bending system that changes the cavity length. The bending system consists of three different rings: the two external rings, which are rigidly connected to the helium tank, and the one at the center, symmetrically divided in two halves. The rings are connected by thin titanium plates, or blades, that can change the cavity length (compression and tension) as a result of an azimuthal rotation in opposite directions of the two halves of the center ring, through the bending of the blades. The big central arm is connected to the bending system to produce the rotation and the axial movement, which provides the cavity tuning. The prototype model (named as original Blade Tuner or SuTu tuner, from the former SUperstructures TUner), successfully tested at DESY in 2002, both in CHECHIA and in the superstructures test module inserted in the TTF string, actually represents the reference design for the entire Blade Tuner activity at Fermilab, being the basis of the next models up to the present light and cheap device. One of the realized tuner prototypes, #IV or SuTu_IV, is shown in the figure 7.2.

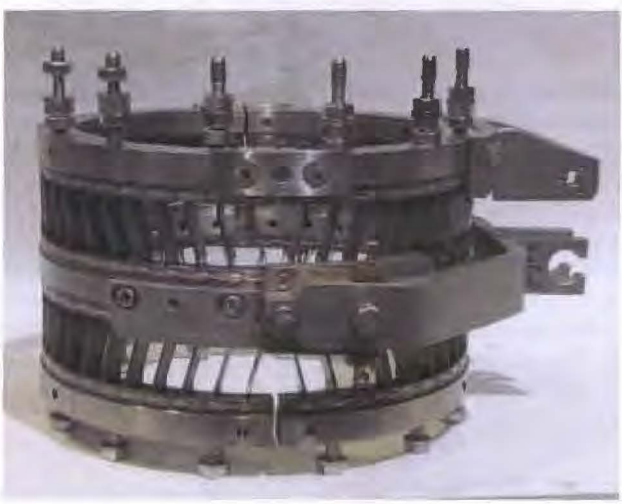

Fig. 7.2 – Blade-tuner prototype realized by INFN-LASA

The stepping motor provides only the slow tuning capability of the tuner, but a fast part is needed to fulfill the cavity design requirements.
Piezo-ceramics actuators (piezo) are used to provide fast tuning capability to the blade tuner. The piezoelectric options for LFD (Lorentz Force Detuning) compensation needs have been now widely validated thanks to several successful tests performed. To be efficient and flexible, the integration of these active elements must follow some guidelines, such as

- Commercial but affordable piezo elements as the first choice for actuators.
- Flexible actuator accommodation, in order to preserve the possibility to install piezo of different sizes or even completely different solutions (e.g. magnetostrictive etc.).
- Ensure slow tuner efficiency even against an eventual complete failure of fast actuators.
- Keep the overall design as simple as possible to reduce the number of additional elements compared to the existing Blade Tuner and lower costs.
- Provide a high axial stiffness for the final assembly in order to lower the sensitivity to Lorentz force detuning and easing fast actuators requirements.

The detailed results obtained by several FEM analyses of the Blade Tuner and its components performed have been used for the integration of these fast tuning elements. Piezoelectric actuators, that represent the reference choice, are subject to several requirements limiting the possible design configurations. First of all, the piezoelectric actuators cannot be subject to tension forces, and

bending and shear actions need to be carefully avoided. Moreover, in order to maximize their lifetime, a correct pre-load range needs to be guaranteed under all operating condition. In addition to that, the characteristic behavior of piezo operation at cryogenic temperatures, in terms of stroke and pre-load effects, has undergone a systematic investigation. Finally the piezoelectric elements have been integrated by inserting two elements between one of the end rings and the corresponding flange on the He vessel, as shown in the figures 7.3, where the He vessel and the cavity are not shown for simplicity. The different tuner parts in these pictures are color-coded by material type: blue denotes Ti, gray stainless steel, yellow CuBe and red brass. The piezo elements are the dark gray rectangular bars acting on the left Ti ring.

Fig. 7.3 – 3d view of the blade-tuner showing the linkings with the He vessel (on the left) and the detail of a piezo-sensor (on the right)

The main purpose of this design choice has been to allow the cavity itself, through its axial stiffness, to generate the mechanical pre-load needed by the piezo actuators. A cavity pre-tuning procedure has been developed in order to guarantee the correct range of pre-load values on the piezoelectric elements along the entire slow tuning range. This procedure allows also avoiding the "neutral" point of the leverage system and requires that the tuner operation always acts stretching the cavity, thus compressing the piezoelectric elements. The position of the piezo actuators has been carefully chosen in order to avoid possible stresses due to the deflection and vibration of the helium vessel. These active elements are kept in position by means of supports as shown in the figure 7.3: they can accommodate elements of length up to 72 mm and a spherical head can be used in order to minimize shear and bending forces. In addition to the piezos, four threaded bars have been introduced on the upper and lower side of the assembly. These bars, parallel to the piezo elements accomplish two different tasks. first of all they are needed during transportation, handling and assembly phases to avoid plastic deformations of the bellow. In this case they are tightly bolted at both ends to provide stiffness to the system. Furthermore, in operating conditions, the inner bolts are loosened by a calibrated distance (less than one mm) and the bars act as safety devices in case of piezo mechanical failure or overpressure conditions inside the He vessel. With respect to the original system used for the TTF superstructures prototype tested at DESY, the leverage system has been rotated to one side, in order to avoid the mechanical interferences with the Invar rod providing the cavity longitudinal alignment in the Cryomodule Type 3 design. The overall final assembly is shown in the figure 7.4.

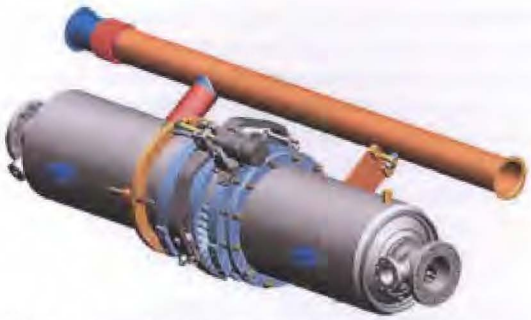

Fig. 7.4 – 3d view showing the whole He vessel-blade-tuner assembly

The solution described above, although it ensures high tuning sensitivity and a perfect symmetrical behavior, is cumbersome and expensive. In particular the friction between rotating and translating parts makes them a weak point that has to be solved in a radically way in order to reduce non-linearity. Therefore a simplified driving system has been realized, reducing drastically the number and complexity of parts. Finally, the revised design solution, with the chosen configuration of the new Blade Tuner rings and blades is presented in the figure 7.5.

Fig. 7.5 – 3d view of the new solution for the blade-tuner design (on the left) and description of the blades' configuration (on the right)

The simplified driving system is also visible, mainly composed by the motor with its harmonic drive and a CuBe screw. The axial movement of the nut is directly transferred in the rotational one by the central rings. Although this arrangement simply push away the two central rings at one side, therefore losing the complete symmetry, finite element computations and experimental test proved the effectiveness of the solution. The experimental test was performed at LASA laboratory by using a simplified mechanism in substitution of the motor. The displacements recorded at the free rings showed a correct axial movement with negligible rotational or translation effects. This result has also been confirmed by FEM computations performed on the new tuner geometry.

One of the most important problems of this new configuration concerns its overall dimension and his compatibility with the constraints due to the ILC cryo-module: the encumbering verify is shown in Fig. 7.6.

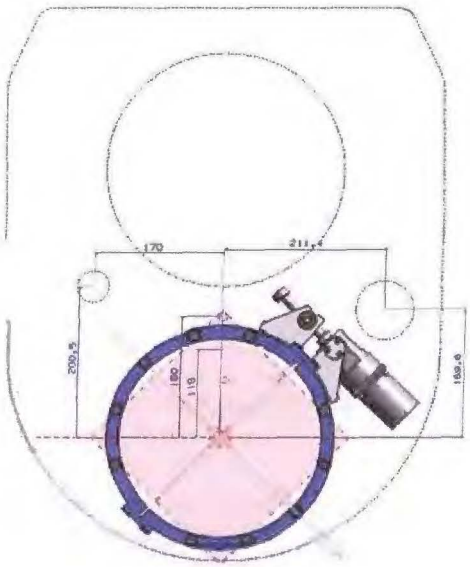

Fig. 7.6 – Encumbering verify for the blade-tuner mounted into the cryomodule

The use of a coaxial tuner opens different possibilities to optimize the geometry of the helium tank and of the cavity end group. In particular the revised tuner design presented is lighter and more compact than the previous one. Positive consequences are a lower impact on the deflection of the cavity and a larger free space for the positioning of the cryomodule elements such as the invar rod. All this has been obtained maintaining the compatibility with the older design, so that this new version can be installed in the already built He vessel only by means of simple adapters. A comparison of the old and new tuner design is shown in Fig. 7.7.

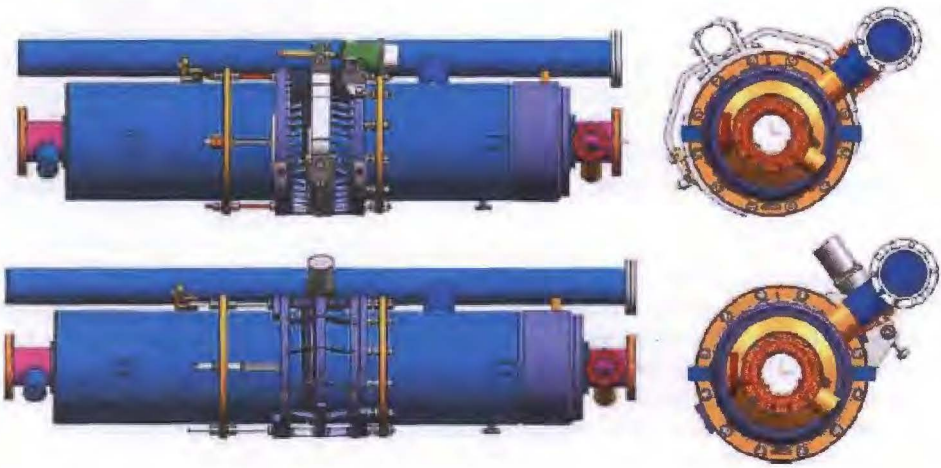

Fig. 7.7 – Comparison between the newer and the older design of the blade-tuner, as mounted on the He vessel

It is clear that the space in the upper part of the helium tank is almost all free, giving an easy access to the positioning of the invar rod.
The materials used for the blade-tuner's components are listed below:

Part	Material	E_T (MPa)	ν	f_y (MPa)[2]	ε_t	f_t (MPa)	ρ (kg/m³)
Blades	Ti Gr5	105000	0.37	830	10%	900	4500
Rings	Ti Gr2	105000	0.37	275	10%	900	4500
Motor supports	Al 6082T6	70000	0.32				2700
Bolts	A4	191000	0.29				

Fig. 7.8 – Physical and mechanical properties of the materials used for the blade-tuner manufacturing

7.2 – Description of the FEA model

The blade-tuner analysis was performed in order to assess the maximum tuning range and to compare it with the values supplied by the INFN-LASA. Another comparison with the INFN-LASA results has been done analyzing the blade-tuner's pre-load and a particular load condition.

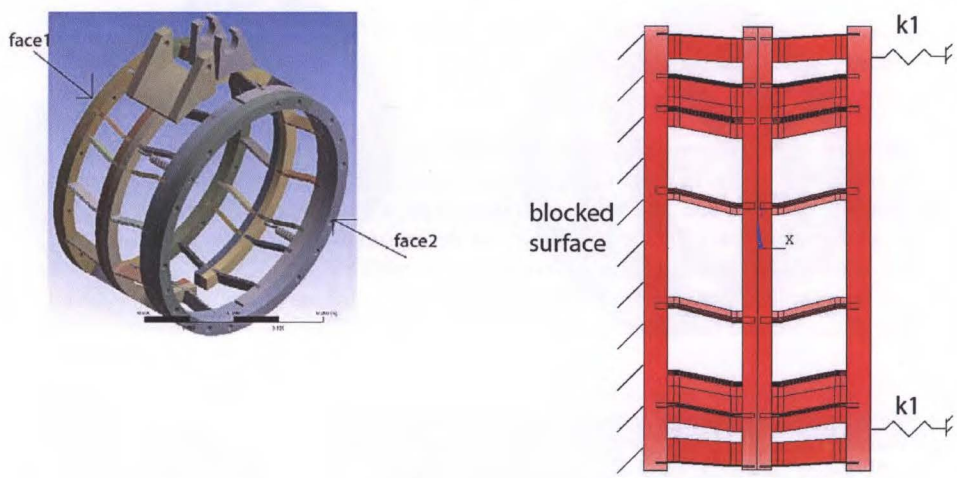

Fig. 7.9 – 3d FEA model used for the blade-tuner analyses and conceptual scheme of the constraints and of the springs used for describing the presence of the HE vessel

The blade-tuner has been blocked with his face1 and presents two springs (with stiffness equivalent to the vessel's one) on his face 2. The stiffness of these springs is the vessel's stiffness in the holes 1 and 2 calculated by a previous analysis (described in chapter 6.2). The safety bars' presence has been introduced into the model as a constraint that avoid the displacements along the y (vertical) and z (parallel to the screw) directions.
The engine action is represented by a remote displacement condition that allow the two engine connections to rotate around the x axis (parallel with the bearings axis) and avoid any other rotation, so that the constraints configuration is very similar with the real one.
In order to compare the simulation results with the INFN-LASA data and assess the limit operative conditions of the blade-tuner, these independent analyses were performed:

- preload analysis: in this condition a 1.1kN force acts on the springs and compress them while the engine connections in the central ring of the blade-tuner are blocked;
- analysis of the stresses when the external flange displacement is 0.497mm: in this load case the safety bars are axially linked with the vessel's flange in the holes 3 and 4, so another two springs have been introduced into the model;
- analysis of the stresses when the engine connections are progressively moved away: the aim of this analysis is to assess the limit condition and the limit of the linear behavior of the blade-tuner. In fact during the normal working of the blade-tuner the blades change their configuration passing from an inclined one to the one where they are parallel with the vessel's axis (stress stiffening effect).

7.3 - Results

- preload analysis:

	value found in the simplified model	value supplied by the INFN
Displacement of the piezo nearest to the engine (mm)	0.20	0.203
Displacement of the other piezo (mm)	0.166	0.16
Blades stress (MPa)	74.7	100

Fig. 7.10 – Comparison between the INFN-LASA results and the 3d FEA model results in the preload condition

The values of the displacement results achieved with the model explained above are very close to the value furnished by the INFN-LASA, while the stresses differences are higher because with this model there was a problem concerning with the element size: in fact this simulation requires very high computational times because there is no symmetry boundary condition to introduce, so the mesh used for the INFN-LASA simulation is probably more coarse then the one used for this FEA analysis.

- analysis of the stresses when the external flange displacement is 0.497mm:

	value found in the simplified model	value supplied by the INFN
Stress on the blades (MPa)	610	552

Fig. 7.10 – Comparison between the INFN-LASA results and the 3d FEA model results in the condition wherein a 0.497mm axial displacement is applied on the external flange of the blade-tuner

- analysis of the stresses when the engine connections are progressively moved away and approached

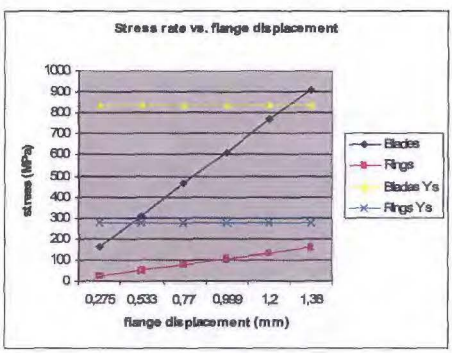

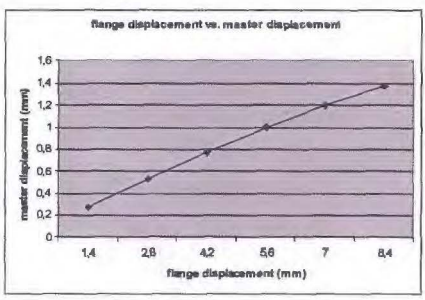

Fig. 7.11 – Stresses rate as a function of the external flange's displacement (on the left) and flange's displacement rate as a function of the engine flange displacement in the moving away condition

The analysis showed that the blade-tuner loses his linear properties after a 1.2mm flanges' relative displacement.

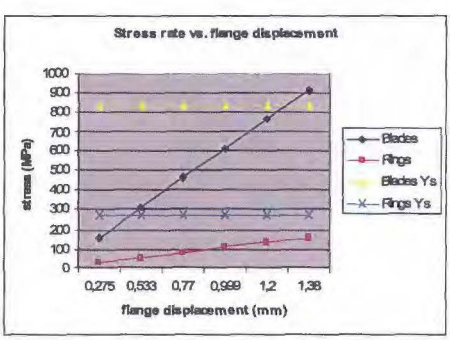

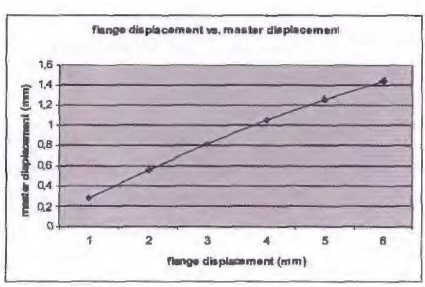

Fig. 7.12 – Stresses rate as a function of the external flange's displacement (on the left) and flange's displacement rate as a function of the engine flange displacement in the approaching condition

The data supplied by the INFN-LASA shows that the maximum blade-tuner's stroke is about 1.8mm for each the approaching and moving away cases, while in this analysis the value is about 1.35mm.

7.4 - Conclusions

The FE analyses shown on this chapter were very important for Fermilab because they allowed to assess the strength of a component that wasn't produced by its own. Moreover the results shown above are confirm the supplier's one.

8. WORK ON THE 3.9 GHz HELIUM VESSEL

In parallel with working on the 1.3 GHz Helium vessel design, the Fermilab was charged by the DESY laboratory in Hamburg with co-operating with it in the design and test of a different "dressed" cavity (called 3.9 GHz). The cavities was performance tested in the Horizontal Test Stand (HTS) at the Meson Test Area at FNAL before being installed in a cryostat with three other 3.9 GHz dressed cavities.

8.1 - Introduction

This paragraph reports the studies on the He vessel for the 3.9 GHz dressed cavity. The purpose of these FE analyses is to find the requirements of the FESHM 5031 (the technical specification), that are summarized below.
Fermilab had to manufacture the 3.9 GHz Cryostat in the framework of a collaboration contract with DESY, and it had to be installed in the FLASH-linac located there. The 3.9 GHz FLASH cryostat supplied by Fermilab had to be consistent with the European legal regulations; DESY was be the importer into the European Union and had to certificate them.
As part of the cryogenic installations of the FLASH-linac (former TTF2-linac) the 3.9 GHz cryostat would have been treated according to the TTF2 risk analysis (Gefahrenanalyse nach Anhang I der Druckgeräterichtlinie (DGRL), May 8, 2003). With reference to this analysis, the cryogenic equipment of the 3.9 GHz cryostat would have been assessed to fall below module I of this DGRL; as a consequence the cryogenic installations require no authorized third party inspections.
According to this technical specification, the 3.9 GHz cryostat would have been treated in line with the standard 1.3 GHz cryomodules: the niobium material of the cavities cannot be certified for the use at low temperatures. The thermal shields and the vacuum vessel of the cryostat act as containment for the inner 2 K pressure vessel.
The DESY safety rules are fulfilled as soon as the cryostat is conforming to the EU rules and the 2 K pressure vessel would have had an MAWP (the maximum working pressure) of 2.0 bar in order to be consistent with the other cryomodules in FLASH.
According to the DGRL, the manufacturer has to take the responsibility for the application of suited technical rules, which are not defined in detail in the DGRL. DESY would have applied the AD2000 technical rules or the European harmonized rules but according to DESY's risk analysis, also the US ASME regulations for pressure vessels could be applied. This was underlined by the fact that for the past decade, DESY has had cryogenic components in use at TTF and FLASH, which were designed and constructed in the US according to ASME regulations (FLASH feed box, test cryostats).
The choice of materials for use at low temperatures had to be in accordance with the European

harmonized rules. Materials allowed by the ASME rules for pressure vessels at low temperatures would have been able to be used with the exception of stainless steel 321, which had to be avoided. For the Ti-vessel, DESY used titanium DIN/EN 3.7035, which corresponds to Ti grade 2. According to the DGRL there was no way to certify niobium for the use at low temperatures. Apart from the cavity made from niobium, all parts of the 3.9 GHz cryostat were going to be designed and manufactured in accordance to the ASME pressure vessel code for the use at low temperatures. Finally parts of the helium vessel ends were also made in niobium or NbTi and were going to be "exceptions" to ASME. Fermilab would have documented that the safely level was very conservatively acceptable and, to the extent that Fermilab could verify so, as good as the ASME code.
The 2d draft of the 3.9 GHz Helium vessel is represented below:

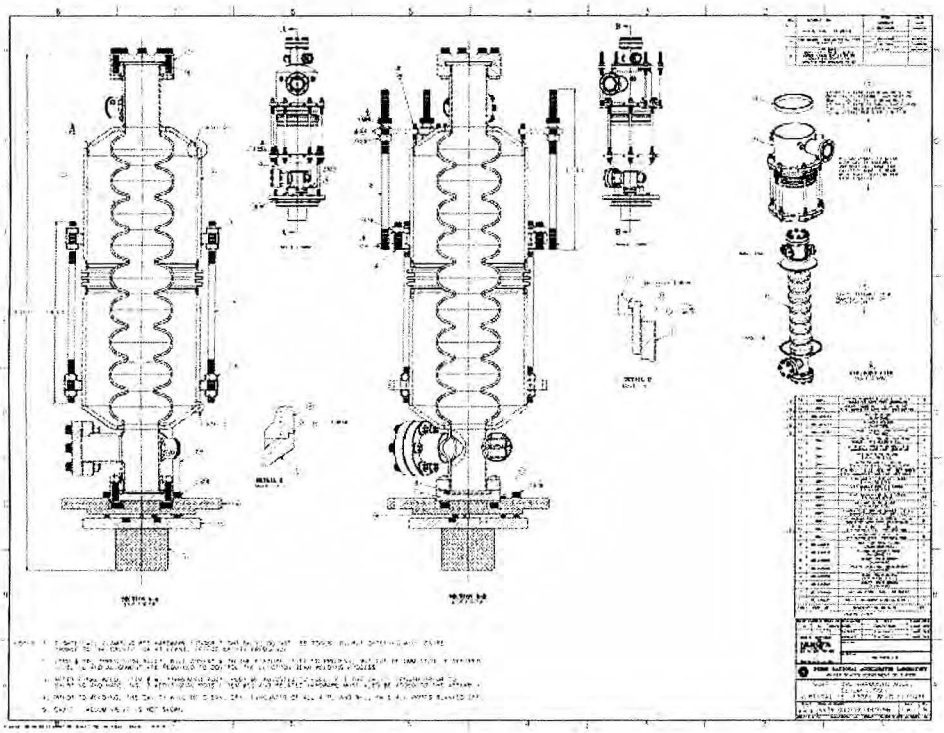

Fig. 8.1 – 2d draft of the 3.9 GHz Helium vessel assembly

8.2 – The analysis required by Fermilab

After analyzing the 3.9 GHz He vessel under similar load conditions with respect to the 1.3GHz already treated on Chapter 4 (the inner pressure is 2.0 bar while the nominal displacement and the intensity of the cool-down are the same), Fermilab required to know the lowest value of the welding depth that could guarantee the respect of the ASME code in order to determine as a safety factor the ratio between the nominal depth and this value.
These resistance analyses have been performed using a 3d FEA model (very similar to the one used for the 1.3 GHz Helium vessel, see Fig. 8.2) that was used for determining the linearized stresses

for all the stress classification lines.

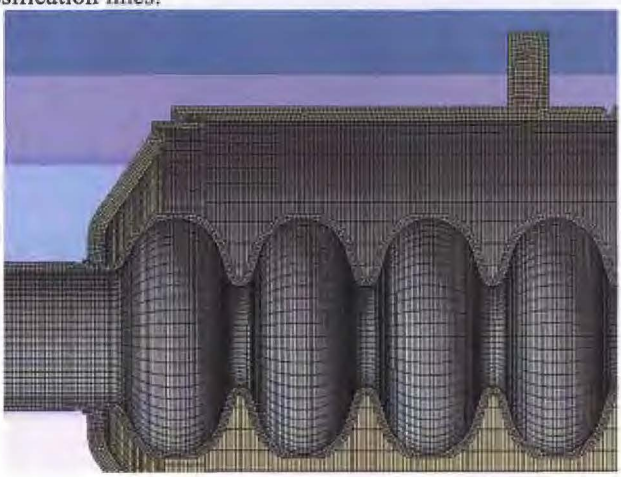

Fig. 8.2 – Mesh of the 3.9 GHz He vessel assembly 3d FE model

The stress classification lines are represented on Fig. 8.3:

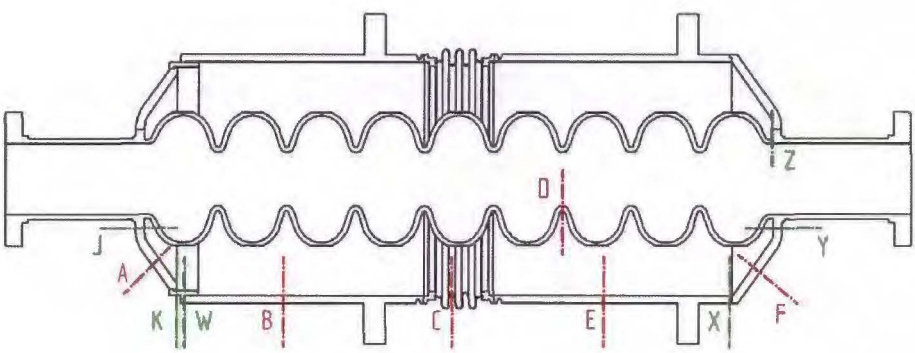

Fig. 8.3 – Stress Classification Lines SCLs used for the Stress Intensity linearization

Since the materials used for this vessel are the same as the 1.3 GHz Helium vessel, the allowable stresses and all the other material data are the same, too. These values can be seen on paragraph 4.3.1.

In order to assess the safety parameter introduced above, a 2d axis-symmetric FEA model has been created: in fact since the previous 3d FE analysis has clarified that helium weight and assembly own weight have not effect on the final stress values, a 2d axial symmetric model (Fig. 8.4) has been used in order to obtain an accurate solution, reducing the computational cost and the time necessary to complete the simulations.

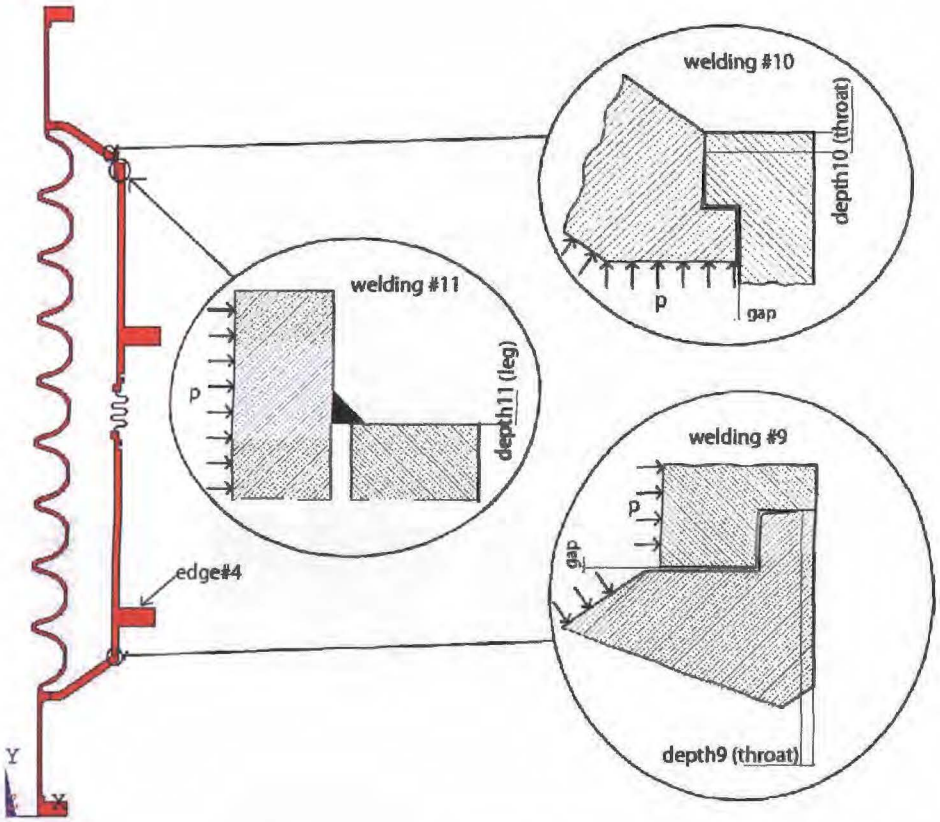

Fig. 8.4 – Weldings scheme for the FE study

The geometry of each Ti-Ti and Ti-TiNb welding has been parameterized choosing the welding depth as free parameter. As shown in Fig 8.4 these parameters are equivalent to:

- Throat of welding #10
- Throat of welding #9
- Leg of welding #11

Starting from the nominal penetration value, the welding depth has been gradually decreased until the origin of stress above the Ti allowable has been observed.
In this 2d FE model these nominal values are the welding depths used in the 3d FE model, it also must be noted that these values are already more conservative than the real ones.
The DESY Laboratories technical staff usually asked for a model with at least 4 elements inside the thickness for all the assembly's elements; besides a quadratic element was introduced in order to obtain more accurate results. The resulting mesh is represented below.

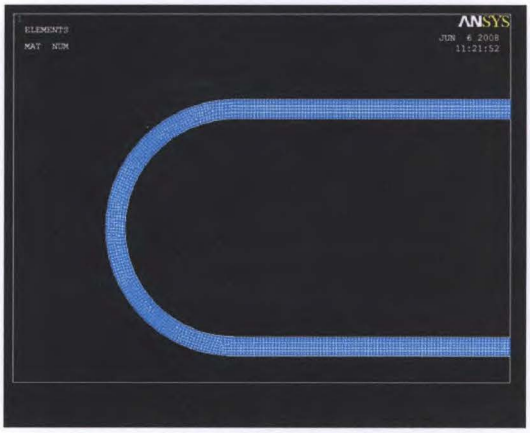

Fig. 8.5 – Resulting mesh for the bellow in the 2d axis-symmetric FE model

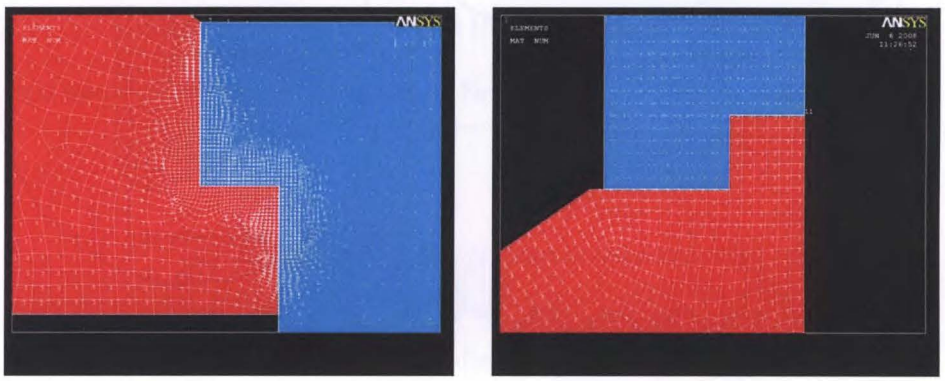

Fig. 8.6 – Resulting mesh for the welding #10 (on the left) and #11 (on the right) in the 2d axis-symmetric FE model

Since during the deformation process the welding zone (if the weld is not performed with a full depth) is exposed to the pressurized Helium, even in these surfaces the pressure must be applied. This fact is represented below.

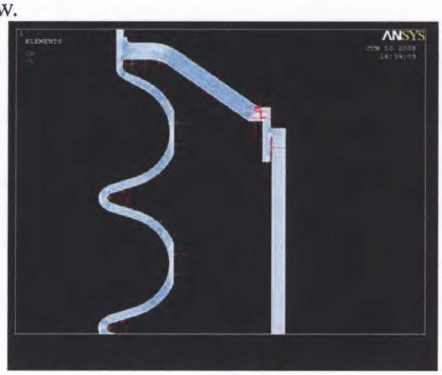

Fig. 8.7 – Application of the inner pressure in the 2d axis-symmetric FE model

Usually a welding area is characterized by the presences of geometric singularities which are cause of localized stress concentrations. The finer is the mesh size the larger will be the value of the total stress near a geometric singularity. In order to avoid problems related with this issue, each sharp edge present in the welding area has been replaced with a small radius.
Since the total stress diverges with the mesh refinement, the total stress map can not be considered a valid tool to use for this particular study.
On the other hand, it has been observed that the sum of intensity membrane stress + intensity bending stress linearized along proper classification lines, remains almost constant within a wide range of mesh sizes (Fig.8.8).
This way to proceed is perfectly consistent with the ASME code sec. VIII div. 2 specifications.
Since the higher stresses are localized on the Titanium components of the assembly, and by the fact that the Ti allowable is lower than the Nb-Ti allowable, the resultant stresses in the welded regions have been compared with the Ti allowable (66 MPa).
In this study both 1st and 2nd load cases contained in the Eng. Note [6] have been considered.

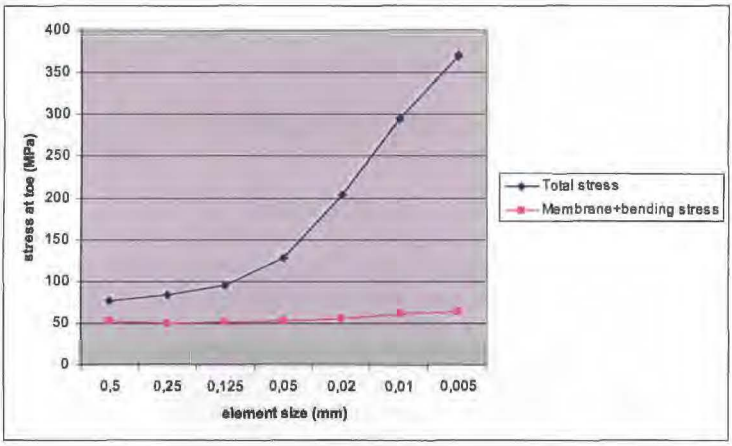

Fig. 8.8 – Stress rate vs. mesh element size (calculated for the welding #10 with 2mm depth)

Total stress values diverge with the mesh refinement. On the other hand, the sum of membrane stress + bending stress is not affected by the mesh size. For this reason, and in order to be consistent with the ASME code specifications, these last stresses have been compared with the Ti allowable.
Another important parameter that influences the joint's behavior is the gap size between two components in the welding region. Usually, the presence of a gap causes the origin of contact phenomena, which could additionally increase the stress values in the welding region: this phenomenon binds the solution to be performed in a nonlinear regimen. On Fig. 8.9 this rate is shown.
In real joints the gap size is about 0.1mm or lower, so the higher stress values have origin with the 0.1mm gap keeping fixed all the other free parameters (welding penetration and mesh size). The simulations have been performed using a 0.1mm gap.

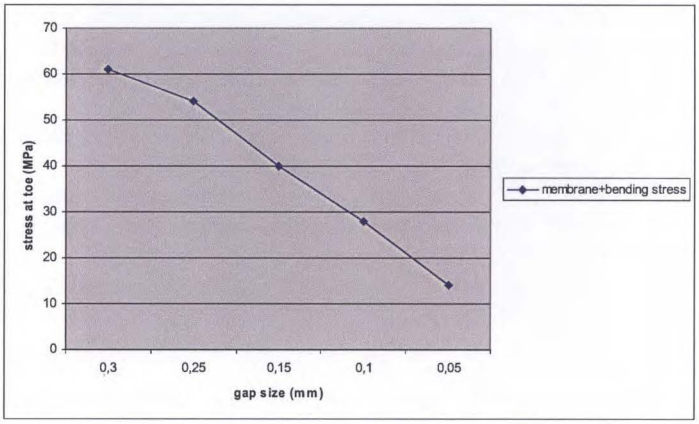

Fig. 8.9 – Stress rate vs. mesh element size (calculated for the welding #10 with 2mm depth)

In the evaluation of the minimal welding penetration required not to exceed the allowable stress limit, the following criteria has been used:

$$Pm + Pb < S_{Ti} = 66\text{MPa}$$

where Sti is the allowable stress for the titanium.

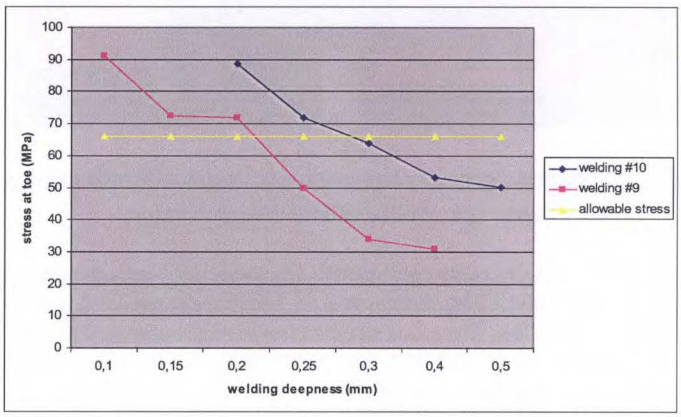

Fig. 8.10 – Welding stress rate for the #10 and #9 welding (gap set at 0,1mm)

As showed in the figure 8.10, the minimum welding depths causing the origin of a stress field exceeding the Ti allowable, are: 0.25mm for the #9 welding (6 times lower than the nominal depth) and 0.3mm for the #10 one (8 times lower than the nominal depth).
For the welding #11 the minimum depth is 0.9mm against a nominal depth of 3mm.

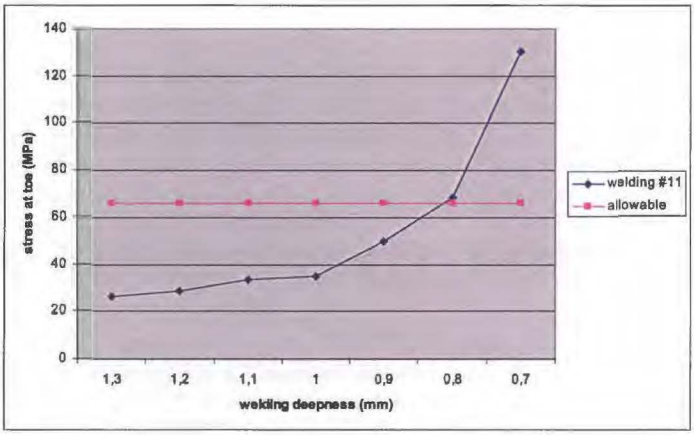

Fig. 8.11 – Welding stress for welding #11

8.3 – Conclusions

The candidate's contribution on the analyses concerning with the 3.9 GHz He vessel consists on the approach used for parametrizing the weldings. In this context the candidate helped the Fermilab staff to treat the weldings described above as variable parameters (coinciding with the value of the welding's depth), directly made through some boolean operations on the Finite Element environment. So that it wasn't anymore necessary to re-generate a new model every time some specific weldings dimensions were required through a CAD environment.
The resulting graphs show that this approach has been very useful to determine the value of the safety factors.

9. R&D ACTIVITIES ON THE HE VESSEL

In order to reduce the costs for the ILC cryomodules design two proposals have been forwarded to the community by the INFN Section of Pisa (in collaboration with JINR DUBNA Laboratory) and the Jefferson Laboratories (in collaboration with Fermilab):

- introduction of a Titanium-Stainless Steel (SS) transition: this change could allow to use the Stainless Steel for manufacturing the pipes containing the liquid Helium instead of the Titanium;
- introduction of a SS He vessel;

These new proposals will be briefly explained in the next paragraphs.

9.1 – The Ti-SS transitions

In the current design of the Titanium He vessel (see back on Fig. 3.2) it is joined with the Titanium pipe for the Helium vending through an intermediate Titanium pipe. In order to reduce the costs the INFN proposed to replace the Ti material with the SS one for the Helium vending pipe and to connect it with the He vessel through a Ti-SS transition (see Fig. 9.1).

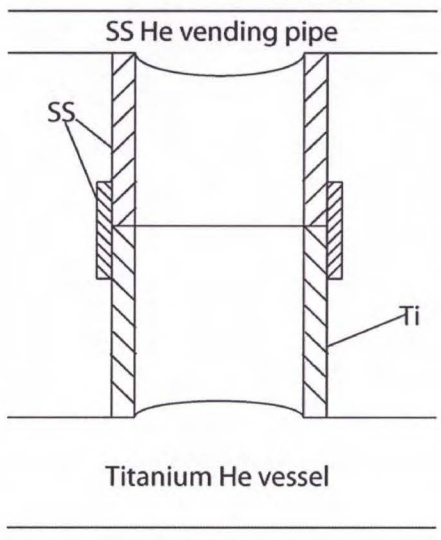

Fig. 9.1 – Conceptual scheme of the Ti-SS transition

This transition consist of two tubes with the same dimensions (thickness and outer diameter), one in Titanium and the other one in Stainless Steel linked together by a Stainless Steel collar. The two tubes are linked with the collar through an explosion bonding welding process.
Since the transition is supposed to be used for the Helium vending system, it must bear the nominal internal pressure (4 bar) and a -270°C cool down without any leak of liquid Helium: in order to evaluate the resistance of this kind of junction under these load conditions several tests have been performed. One of the most important tests (performed by the Pisa section of the INFN) is the Helium leak test, that will be briefly explained below.
The transition sample for this test is shown on Fig, 9.2: this sample was made by the Sarov company in Russia.

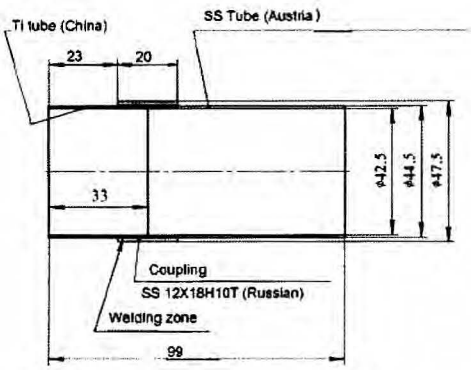

Fig. 9.2 – Ti-SS transition sample used for the Helium leak tests

A dedicated set-up was made for these tests. It consisted of a blind stainless steel flange (DN63) to close the aperture on the Titanium side and a stainless steel reduction (DN63–DN25) mounted to close the stainless steel aperture from the other side. Finally a DN25 connection was mounted to connect the sample with the Helium leak detector. Both the o-rings on these two flanges were handmade by using the Indium wire 2 mm in diameter. The choice of this gasket was motivated by the need to carry out tests at two different temperatures: room and liquid nitrogen (300 K and 77.3 K, respectively). The two standard stainless steel vacuum components (the blind flange DN63 and the DN63-DN25 reduction) and the joint sample were assembled together with 6 stainless steel threaded rods equipped with nuts and washers assuring the right vacuum seal (see Fig. 9.3). The same gasket (Indium wire) was applied for the connection between the flex pipe of the leak detector and the experimental set-up. The vacuum seal was completed by using a C-clamp.

Fig. 9.3 - Experimental set-up of the Ti-SS transition sample to be tested (on the left) and connected to the leak detector with a C-clamp (on the right)

In order to test the experimental setup at 77K a standard SS flex pipe was mounted between it and the leak detector and this setup was immersed into a dewar filled with liquid nitrogen.
The Ti-SS transition sample under consideration has shown excellent behavior both at the room and liquid nitrogen temperatures as well as under high pressure tests and after thermal cycling. The helium leak rate of the sample always was on the order of ($1x10^{-10}\pm10\%$) mbar* l/s. This result was very good for initial tests of this type of welding, i.e. – by using the explosion bonding technique, but it will be necessary to perform similar tests with a larger number of samples to obtain more reliable data and statistics.
The Pisa section of the INFN is also planning to carry out additional tests with the samples at liquid helium temperature. A metallographic analysis of the explosion bonding welded joint will also be performed to get more information about the structure of the welded surface and the surrounding area.

9.2 – The Stainless Steel Helium vessel (SS He vessel)

In the current design the ILC cryomodules contain a large amount of structures made of Titanium, which have 2 main defects:

- manufacturing: for instance one of the most important problems of producing the Titanium He vessel is that the TIG weldings between the vessel and the ring, and between the ring and the flat disk are very difficult to be performed because Titanium is very sensitive to a small variation of the weld parameters, so this operation must be performed by a machine instead of a skilled worker. In fact it has been marked that Titanium-Titanium TIG weldings performed by skilled workers can usually produce an oxygen penetration into the weld zone (so that a fragility condition can occur). Moreover welding around a circumference is a very difficult task to be achieved by a numeric control machine;
- cost: the intrinsic cost of the Titanium is much higher than the SS's one.

In order to eliminate these problems and increase the feasibility of the ILC project a proposal for a SS He vessel has been done: in this way the cost reduction is higher than the one obtained only by introducing the Ti-SS transition above described. The C100 cavity (designed and manufactured at the Jefferson Laboratories) is an example of a cavity equipped with a SS He vessel and showed that this new design can meet the same requirements than the Ti He vessel.

The distinguishing (with regards to the Titanium He vessel) mechanical features of this new He vessel are explained below:

- there are no stiffening rings: as shown on chapters 4 and 6 the stiffening rings improve a lot the resistance of the cavity to the helium outer pressure and increase the buckling point, but they even decrease the vessel's efficiency (so the blade-tuner needs to push more in order to stretch the cavity by the same quantity) because of their important contribution to the cavity's stiffness. The fact that the blade-tuner needs to push more is a clear sign of the bad tunability of the cavity equipped with the reinforcing rings;
- the tuner stretches the cavity through a different mechanism: a scissor-jack tuner has been introduced outside the SS He vessel instead of a blade-tuner.

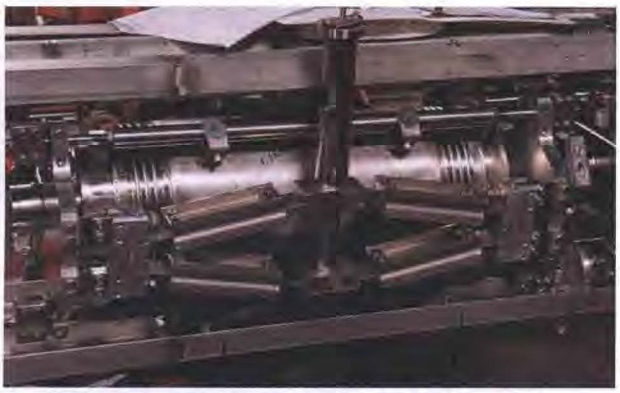

Fig. 9.4 – Tuning system for the SS He vessel

This mechanism differently works with regards to the Ti He vessel's blade-tuner: in fact, while in the current version of the He vessel the axial relative displacement of the flanges is given by a different bending grade of the blades, in the new design proposal it is given by a rod-crank kinematism, which allows lower stresses for the tuner's components. A scheme for the functioning of this new tuner is represented n Fig. 9.5.

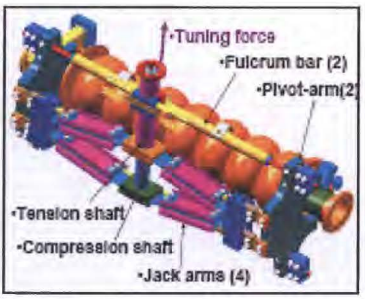

Fig. 9.5 – Conceptual scheme of the tuner's functioning

This new tuner is linked to the SS vessel through two flanges that aren't located in the middle of the vessel (as for the Ti He vessel) but on its ends, so the central bellow (that has been introduced for the Ti He vessel) has been replaced with two smaller bellows located near the flanges (Fig. 9.3).

- Niobium (cavity) and Stainless Steel (He vessel) are welded one to each other without any

need for an intermediate material: as shown on chapter 6 one of the problems of the Ti He vessel is the very low stiffness of the end-caps, also due to the high compliance of the material itself. In order to weld these two materials, for this new generation He vessel, Stainless Steel and Niobium are brazed and there is a lot of R&D that is being performed by the Jefferson Laboratories in the USA concerning with the reliability of this operation.

A 2d draft of the SS He vessel is shown in Fig. 9.6.

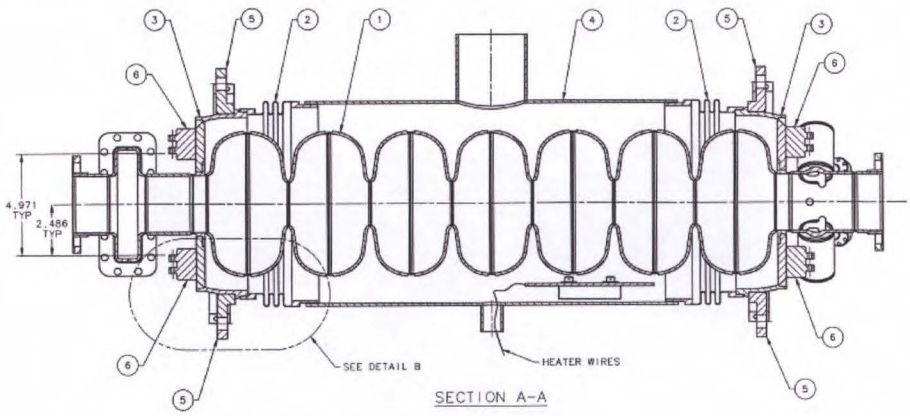

Fig. 9.6 – 2d draft of the C100 SS He vessel

A very important operation included into the fabrication process of the SS He vessel is the braze between the SS end-caps end the Nb tee. In fact some tests performed by the Jefferson Laboratories and other factories all around the world showed that it is a very critical topic for the whole manufacturing cycle because of its bad reliability in terms of static resistance and retaining of the Helium inside the vessel.
The parts involved in this operation are shown on Fig. 9.7.

Fig. 9.7 – Parts involved in the braze process

Before starting the welding operation the components shown above undergo a preparation process in order to eliminate the impurities. The whole preparation process is explained below:

- First of all these parts are cleaned in an ultrasonic environment and water rinsed;
- They are triple rinsed with pure water and dried with dry nitrogen;
- The parts are etched (for the SS this operation lasts 1 hour and involves a 30% nitric solution, while for the Nb it lasts only 1 minute and involves a BCP solution);
- Parts are dried with dry nitrogen and sealed in clean nylon bags.

After the preparation process, the parts are ready for being machined and finally brazed: the full procedure is listed below.

- All the 3 parts are machined in order to have a clearance between SS Transition plate and Nb Tee and between Nb Tee and SS Plug: the value of this clearance is about 0.001-0.004";
- Transition plate outer features are post-machined;
- The Transition plate is welded with the Tee: this welding is performed into an oven and the maximum reached temperature is about 1000°C (see Fig. 9.8).

Fig. 9.8 – Temperature rate through time for the brazing process

Before putting the 2 parts into the oven, the plug is inserted in the Tee: the SS's thermal expansion coefficient is higher than the Nb's one so during the permanence into the oven the Tee is pressed by the Plug against the Transition plate. As a consequence the inner stress state of the joint after the weld is not as critical as it could be if the braze was performed without the support of the Plug.

- The Nb tee is machined and all the alloy is cut up to obtaining a 0.15" thickness.

In the picture 9.9 the 3 parts are represented when they are taken out of the oven.

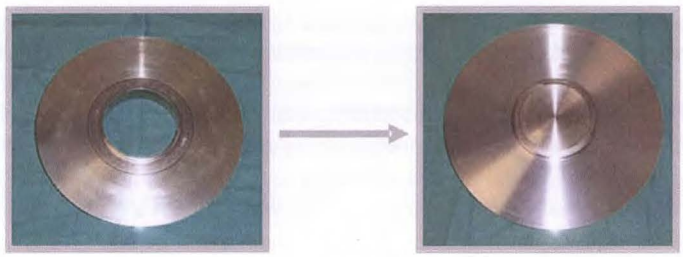

Fig. 9.9 – Brazing parts after the join process

All the welds regarding the SS only are performed through the TIG process: this kind of operation is easily performable because SS is adapted to this process and there are a lot of industries able to perform it with low costs.
A cost assessment has been performed for both the SS He vessel and the Ti He vessel, and it was shown that the new vessel is almost the 50% cheaper than the old one. Some other R&D is being developed concerning the material used for the braze: in this version a 50%Cu-50%Au alloy is used but it's very expensive, so the Jefferson Laboratories staff is trying to replace this material with Cu. In this context the INFN (Section of Pisa) in collaboration with DG Technologies (Parma, Italy) is trying to test the brazing procedure between the Nb and the SS by using a different kind of intermediate alloy. The INFN (in collaboration with the DUBNA Laboratories) is also testing the connection between the Nb and the SS by using the explosion bonding technique (already successfully used for the Ti-SS transitions) instead of the brazing one.

Conclusions

All the finite elements analyses contained and described in this thesis made possible the certification of the whole superconducting cavity-Helium vessel assembly at Fermilab. Furthermore they gave several useful indications to the Fermilab staff to improve the performance of the Helium vessel by modifying some design parameters or refining the manufacturing processes.
All the results found for these analyses were concordant with the experimental evidents coming from the Fermilab facilities.
The candidate wants to thank the Fermilab staff for having supported him in all the works described on this thesis, the INFN Staff (in particular Mr Andrea Basti and Mr Franco Bedeschi) for their support on its drawing up. Finally special thanks are directed to the teachers of the college of engineering in Pisa for having given the possibility of doing this wonderful experience.

Bibliography

1. INFN-LASA, presentation draw on the INFN school on electron accelerators
2. T. Arkan, 1.3GHz Cavity Dressing Plans for CM2
3. E. Daly, C100 He vessel
4. N. Panzeri, Design of Slim Tuner ver. 3.9.4
5. A. Basti, F. Bedeschi, J. Budagov, F. Frasconi, S. Linari, B. Sabirov, A. Sissakian, A. Sukhanova; Leak rate measurements on bimetallic transition samples for ILC cryomodules
6. M. Wong, G. Galasso, Harry Carter, Tom Peterson, Phil Pfund, Dan Olis, Tug Arkan; Pressure Vessel Engineering Note For the 3.9-GHz Helium Vessel, Cavity #5
7. A. Basti, F. Bedeschi, J. Budagov, F. Frasconi, S. Linari, B. Sabirov, A. Sissakian, A. Sukhanova; Characterization measurements of Ti-SS Bimetallic transition joint samples